UNIVERSIDADE FEDERAL DO RIO GRANDE DO SUL

INSTITUTO DE PESQUISAS HIDRÁULICAS

PROGRAMA DE PÓS-GRADUAÇÃO EM RECURSOS HÍDRICOS E SANEAMENTO AMBIENTAL

GABRIEL FERNANDO NARVÁEZ CAMPO

FLUID-SOLID THERMAL COUPLING IN PIPE AND CHANNEL TURBULENT FLOWS *VIA* A DUAL IMMERSED BOUNDARY METHOD

PORTO ALEGRE

2019

GABRIEL FERNANDO NARVÁEZ CAMPO

FLUID-SOLID THERMAL COUPLING IN PIPE AND CHANNEL TURBULENT FLOWS *VIA* A DUAL IMMERSED BOUNDARY METHOD

Thesis submitted to Postgraduate Program in *Recursos Hídricos e Saneamento Ambiental* of Universidade Federal do Rio Grande do Sul as a partial requirement to obtain the Ph.D. degree in *Recursos Hídricos e Saneamento Ambiental*.

Supervisor: Edith Beatriz Camaño Schettini

Co-supervisor: Jorge Hugo Silvestrini

PORTO ALEGRE

2019

CIP - Catalogação na Publicação

Narváez Campo, Gabriel Fernando
FLUID-SOLID THERMAL COUPLING IN PIPE AND CHANNEL TURBULENT FLOWS VIA A DUAL IMMERSED BOUNDARY METHOD / Gabriel Fernando Narváez Campo. -- 2019.
162 f.
Orientadora: Edith Beatriz Camaño Schettini.

Coorientador: Jorge Hugo Silvestrini.

Tese (Doutorado) -- Universidade Federal do Rio Grande do Sul, Instituto de Pesquisas Hidráulicas, Programa de Pós-Graduação em Recursos Hídricos e Saneamento Ambiental, Porto Alegre, BR-RS, 2019.

1. Escoamento turbulento. 2. Simulação numérica de alta ordem. 3. Interação térmica fluido-sólido. 4. Método de fronteiras imersas . I. Camaño Schettini, Edith Beatriz, orient. II. Silvestrini, Jorge Hugo, coorient. III. Título.

Elaborada pelo Sistema de Geração Automática de Ficha Catalográfica da UFRGS com os dados fornecidos pelo(a) autor(a).

GABRIEL FERNANDO NARVÁEZ CAMPO

FLUID-SOLID THERMAL COUPLING IN PIPE AND CHANNEL TURBULENT FLOWS *VIA* A DUAL IMMERSED BOUNDARY METHOD

Thesis submitted to Postgraduate Program in *Recursos Hídricos e Saneamento Ambiental* of Universidade Federal do Rio Grande do Sul as a partial requirement to obtain the Ph.D. degree in *Recursos Hídricos e Saneamento Ambiental*.

Approved at: Porto Alegre, on June 12, 2019.

Profa. Dra. Edith Beatriz Camaño Schettini - UFRGS
Supervisor

Pr. Dr. Jorge Hugo Silvestrini - PUCRS
Co-supervisor

Profa. Dra. Daniela Guzzon Sanagiotto - UFRGS
Committee member

Prof. Dr. Eric Lamballais - Universitè de Poitiers
Committee member

Prof. Dr. Rubem Mario Figueró Vargas - PUCRS
Committee member

Prof. Dr. Guillermo Osvaldo Artana - Universidad de Buenos Aires
Committee member

Dedico este trabajo al todo poderoso, a mi madre Cristina
y a mi padre Pablo, este es un resultados de su amor,
formación y acompañamiento en cada ambito de mi vida.

Agradecimentos

Agradeço à professora Edith Beatriz Camaño Schettini pelo apoio, conhecimento transmitido e pela sua amizade. Agradeço ao professor Jorge Silvestrini pelos seus comentarios agudos sobre meu trabalho, contribuiram muito na qualidade do mesmo. Agradeço ao professor Eric Lamballais, seus ensinamentos e acompanhamento na França me permitiram fortalecer meu caminho como pesquisador e pessoa. Agradeço a todos os meus amigos do Núcleo de Estudos em transição e Turbulência (NETT) e de todo o Instituto de Pesquisas Hidráulicas (IPH), foram 6 anos de construção que me acompanharão para sempre. Quero agradecer a Clarissa, sua paciente escuta baseada em amor sinceiro me fizeram sentir longe da solidão e me fortaleceram em momentos dificeis. Finalmente, agradeço ao IPH da UFRGS, que foi a minha casa durante tantos anos. Todo isto foi possível graças ao Conselho Nacional de Desenvolvimento Científico e Tecnológico pela bolsa de doutorado. Obrigado ao Brasil por ser meu lar.

Resumo

Este trabalho aborda numericamente o problema da Interação Térmica Fluido-Sólido. Uma representação precisa da transferência de calor é essencial no projeto de sistemas de aquecimento ou arrefecimento/resfriamento. Porém, para aplicações industriais, o entendimento da transferência de calor turbulenta se mantem limitado, especialmente na vizinhança da interface fluido-sólido. Esta pesquisa visa desenvolver uma ferramenta numérica original, simples de implementar e geometricamente flexível no intuito de aportar no entendimento da transferência de calor turbulenta e problemas envolvendo transporte escalar, *via* Simulação Numérica Direta ou Simulação Numérica Implícita de Grandes Escalas. As equações governantes são resolvidas numericamente aplicando o código *Incompact3d*, que se baseia no método de diferenças finitas compactas de sexta-ordem, para diferenciação espacial, e um esquema de Adams-Bashforth de terceira-ordem em conjunto com o método do passo fracionado. A geometria do sólido representada por meio de um Método de Fronteiras Imersas baseado na forçagem direta de quantidade de movimento, aplicada ao escoamento turbulento periódico em canal plano fechado e conduto circular. O escoamento em canal é avaliado para três condições de contorno térmicas: fluxo de calor imposto (tipo Neumann), temperatura imposta (tipo Dirichlet) e interação térmica fluido-sólido (tipo Dirichlet e Neumann) na parede/interface. O escoamento no conduto circular é avaliado para condição de temperatura imposta na parede. A análise de convergência, para escoamento laminar, mostra até sexta-ordem de precisão para canal plano submetido a temperatura constante e até segunda-ordem para as outras condições térmicas na parede e para escoamento em conduto circular. Nos casos turbulentos, as estatísticas básicas da velocidade e da temperatura tiveram um excelente ajuste a dados de referência, e o fenómeno de transferência de calor foi representado consistentemente, ainda para resoluções menores do que a espessura da camada limite viscosa.

Palavras chave: Escoamento Turbulento, Simulação Numérica de Alta Ordem, Interação Térmica Fluido-Sólido, Método de Fronteiras Imersas.

Abstract

This study deals numerically with Fluid-Solid Thermal Interaction. Accurate representation of fluid-solid heat transfer is the key for designing heating and cooling systems. However, for industrial applications, the understanding of the conjugate heat transfer remains in deficit, especially near the fluid-solid interface. This research aims to develop an original, straightforward, geometrically flexible and accurate numerical tool to improve the understanding of turbulent heat transfer and problems involving scalar transport, *via Direct Numerical Simulation* or *Implicit Large Eddy Simulation*. The fluid dynamic and heat transfer governing equations are solved numerically by the *Incompact3d* code based on 6^{th}-order compact schemes of finite differences, for spatial differentiation in a Cartesian mesh. The time advancement is carried on by a 3^{th}-order Adams-Bashforth together with a fractional time step. The solid geometry is represented by an Immersed Boundary Method based on momentum direct forcing. The thermal interaction is studied in pipe and plane channel turbulent flow. *Periodic channel flow* was evaluated for three thermal boundary conditions: imposed heat flux (Neumann-type), imposed temperature (Dirichlet-type) and *fluid-solid thermal interaction* (Dirichlet and Neumann type) at the wall/interface. *Periodic pipe flow* was evaluated for an imposed temperature at the wall. The convergence analysis shows a second order accuracy at the fluid-solid interface. The velocity and temperature statistics had an excellent agreement with the reference results, and the turbulent heat transfer phenomenon was consistently represented, even using lower spatial resolution than the thickness of the viscous sublayer.

Keywords: Turbulent Flow, High-order Numerical Simulation, Fluid-Solid Thermal Interaction, Immersed Boundary Method.

List of figures

Lista de Tabelas

List of symbols

A	Cross-sectional flow area	m^2
a^I, b^I	Coefficients to interpolate via 6^{th}-order schemes	–
a', b', c'	Compact schemes coefficients for first derivative	–
a'', b'', c''	Compact schemes coefficients for second derivative	–
c_p	Specific heat capacity of the fluid	$J/(kgK)$
c_{ps}	Specific heat capacity of the solid	$J/(kgK)$
D	Pipe diameter	m
D_h	$(= A/P)$ Ratio of the cross-sectional area to the wetted perimeter	m
D_x^I	Matrix for 6^{th}-order values interpolation	–
D_x'	Matrix for 6^{th}-order derivative interpolation	–
E_x^I	Matrix for 6^{th}-order values interpolation	–
E_x'	Matrix for 6^{th}-order derivative interpolation	–
Fr_τ	$(= u_\tau/\sqrt{gD_h})$ Friction Froude number	–
f	Auxiliary function	–
f_Θ	Source/sink term in the fluid energy dimensionless equation	–
$\vec{f}$	Vector with the discrete values of function f	–
$\vec{f_{IB}}$	Forcing term in dimensionless momentum equation	–
$\vec{f_\tau} = [f_\tau\ 0\ 0]^T$	Streamwise forcing term in momentum equation	–
G	$(= \alpha/\alpha_s)$ Ratio of fluid/solid thermal diffusivities	–
G_2	$(= \lambda_s/\lambda)$ Ratio of solid/fluid thermal conductivities	–
H	Channel height	m
h	Local convection heat transfer coefficient	$W/(m^2K)$
i	Index referred to x axis	–
j	Index referred to y axis	–
K	$(= \sqrt{(\rho c_p \lambda)/(\rho_s c_{p_s} \lambda_s)})$ Thermal activity ratio	–
k_x, k_y, k_z	Wavenumber in x-, y- and z- direction, respectively	–
k_{x_c}, k_{y_c}, k_{y_c}	Exact wavenumber at mesh cutoff	–
k'_x, k'_y, k'_z	Modified wavenumber in x-, y- and z- direction, respectively	–
k'_{x_c}, k'_{y_c}, k'_{y_c}	Modified wavenumber at mesh cutoff	–
k''_x, k''_y, k''_z	Modified square wavenumber	–
k''_{x_c}, k''_{y_c}, k''_{y_c}	Modified square wavenumber at mesh cutoff	–

L_e	Entrance length in a duct	m
L_c	Characteristic length (pipe diameter or channel length)	m
L_x	Dimensionless length of the computational domain in x	$-$
L_y	Dimensionless length of the computational domain in y	$-$
L_z	Dimensionless length of the computational domain in z	$-$
$\dot{m}$	Rate of mass flow	kg/s
Nu	$(= (hL_c)/\lambda)$ Nusselt number	$-$
$N_{x,y,z}$	Number of mesh nodes in x, y or z axis	$-$
n	Index referred to the time	$-$
n_x	Component of $\vec{n}$ in x	$-$
n_y	Component of $\vec{n}$ in y	$-$
n_z	Component of $\vec{n}$ in z	$-$
$\vec{n}$	Dimensionless unitary vector normal to the fluid-solid interface	$-$
P	Wall perimeter in internal flow	m
Pr	$(= \nu/\alpha)$ Prandtl number	$-$
p	Dimensional pressure field	Pa
Q	Volumetric flow rate	m^3/s
Re	$(= (U_b L_c)/\nu)$ Reynolds number	$-$
r	Radial coordinate	$-$
$\vec{s}$	Dimensionless unitary vector tangential to the fluid-solid interface	$-$
T	Temperature field	K
T_b	Bulk temperature	K
T_r	Reference temperature	K
T_{rms}	Temperature root mean square	K
$T\|_{int}$	Temperature at fluid-solid interface	K
tU_b/L_c	Dimensionless time	$-$
U_b	Bulk velocity	m/s
$\vec{u}$	Dimensionless velocity vector of the fluid	$-$
u_τ	Friction velocity	m/s
u_x	Dimensionless fluid velocity component in $x-$direction	$-$
u_y	Dimensionless fluid velocity component in $y-$direction	$-$
u_z	Dimensionless fluid velocity component in $z-$direction	$-$
V_x	Dimensional fluid velocity component in $x-$direction	$-$
V_y	Dimensional fluid velocity component in $y-$direction	$-$
V_z	Dimensional fluid velocity component in $z-$direction	$-$
$\vec{V}$	Dimensional velocity vector of the fluid	$-$
$\vec{x}_{i,j}$	Distance vector from the origin to the mesh point (i,j)	m
x	Dimensionless streamwise coordinate	$-$
x_i	$(= (i-1)\Delta x)$ coordinate at point i	$-$
y	Dimensionless vertical/wall-normal coordinate in pipe/channel configuration	$-$
z	Dimensionless horizontal/spanwise coordinate in pipe/channel configuration	$-$

Greek symbols

α	Thermal diffusivity of the fluid	m^2/s
α_s	Thermal diffusivity of the solid	m^2/s
α^I	Interpolation coefficient	–
$\alpha_{IBM}, \beta_{IBM}$	Coefficients of the *Virtual boundary method*	–
α'/α''	Coefficient to compute $1^{th}/2^{nd}$ derivative via compact schemes	–
α_{cut}	Proportionality coefficient relating exact and modified cutoff wavenumber	–
β	Auxiliary constant depending on internal flow configuration	–
λ	Thermal conductivity of the fluid	$W/(mK)$
λ_s	Thermal conductivity of the solid	$W/(mK)$
Δt	Dimensionless computational time step	–
Δx	Dimensionless mesh spacing in x	–
Δy	Dimensionless mesh spacing in y	–
Δz	Dimensionless mesh spacing in z	–
δ	Density function nearby the immersed boundary	–
δ_{BL}	Boundary layer thickness	m
Θ	Dimensionless temperature field in fluid domain	–
Θ_s	Dimensionless temperature field in solid domain	–
μ	Dynamic viscosity coefficient	Ns/m^2
ν	Cinematic viscosity coefficient	m^2/s
Π	Dimensionless pressure field	–
ϕ	Porosity of the medium	–
$\varphi\|_{int}$	Dimensional heat flux at wall	W/m^2
η	Refinement parameter	–
ρ	Density of the fluid	kg/m^3
ρ_s	Density of the solid	kg/m^3
σ_i	Limit of stability region in imaginary axis	–
σ_r	Limit of stability region in real axis	–
τ_w	Shear stress at wall	N/m^2

Acronyms

CHT Conjugate heat transfer
DBC Dirichlet-type boundary condition
FSI Fluid-solid interaction
IB Immersed boundary
IBM Immersed boundary method
IF Ideal locally imposed heat flux at the wall
IT Ideal locally imposed non-uniform temperature at the wall
IUT Ideal locally imposed uniform temperature along the wall
NBC Neumann-type boundary condition

Contents

Chapter 1

Introduction

1.1 Relevance

Real fluid systems have physical boundaries such as solid walls and/or another fluids. Inside the atmosphere, there is a wide variety of phenomena involving fluid-solid interaction (*FSI*). *FSI* occurs when the flow and the solid are coupled and thus their responses co-exist by mean a feedback relation. This feedback can be observed, for instance, in oscillations of a solid submitted to certain flow conditions (fluid-solid dynamic coupling) or in heat transfer processes between a flow and its solid boundaries (fluid-solid thermal coupling). This study focuses on the analysis of the **fluid/solid thermal interaction**.

A fluid in movement can be an efficient way to transport heat from one source to other. In industry, flows are commonly in the turbulent regime, then, the devices efficiency depends on a high understanding of the heat transfer process in turbulent flows. In wall-bounded flows, thermal interactions occur between fluid and solid. This interaction is so-called *Conjugate heat transfer* (*CHT*), which represents the fluid-solid thermal coupling. Accurate representation of fluid-solid *CHT* is the key for designing nuclear reactors, heat exchangers, and cooling and heating systems. The difficulty in experimentally measuring turbulent quantities, inside very thin boundary layers (Saha *et al.*, 2014[89]), makes numerical simulation a superior tool to study instantaneous turbulent flow structures (Kasagi, 1995[38]). However, the number of published studies which validated near-wall statistics of turbulent heated flows is relatively small and, the understanding on *CHT*, inside the thermal boundary layer, is limited, for industrial applications.

1.2 Objectives

This research aims to develop an accurate numerical tools, using *DNS* or *ILES* in the immersed boundary methods framework, to improve the understanding on fluid/solid thermal interaction in turbulent heated internal flows. To accomplish this objective, the following specific objectives have to be reached:

- To establish a methodology for coupling the streamwise **heat source/sink term**, in the energy equation;
- to impose and validate a **Dirichlet-type boundary condition** for the temperature imposition at the immersed fluid-solid interface;
- to develop, implement and validate a novel numerical approach to ensure a **Neumann-type boundary condition** at the fluid-solid immersed interface;
- to represent the **solid-fluid thermal coupling** in periodic flow;

1.3 Principal contributions and developments

In this numerical research, the code *Incompact3d* is used as fluid dynamic solver. Then, all developments are implemented in agreement with *Incompact3d*'s computational strategy. This open source code (License GNU GPL v3, `https://www.incompact3d.com/`) was developed at Université de Poitiers and Imperial College of London (Lardeau *et al.*, 2002[53]; Laizet *et al.*, 2009[48] e 2011[50]). As *Incompact3d* solves the incompressible fluid dynamic equations in a rectangular Cartesian mesh, the developments are framed in the recent customized immersed boundary method (*IBM*) based on an adapted direct forcing (Gautier *et al.*, 2014[22]).

In this framework, the main contributions of the present work are:

- The source term, which allows dealing with a periodic flow in horizontal ducts, was coupled to the fluid energy equation for pipe and channel flow and three thermal boundary conditions.

- For first time in *Incompact3d*, a customized *IBM* is used to prescribe a scalar derivative at the fluid-solid interface. This original methodology allows imposing a scalar value on the immersed boundary to virtually ensure a derivative.

- The capability of imposing derivative and value can be applied in solving problems on turbulent fluid-solid heat transfer or even in problems involving scalar passive transport. This was achieved by mean Direct Numerical Simulation (*DNS*) or Implicit Large Eddy Simulations (*ILES*).

1.4 Structure of the text

The core of this text can be compiled into three parts: Review - Methodology - Results and concluding remarks (Figure 1.1).

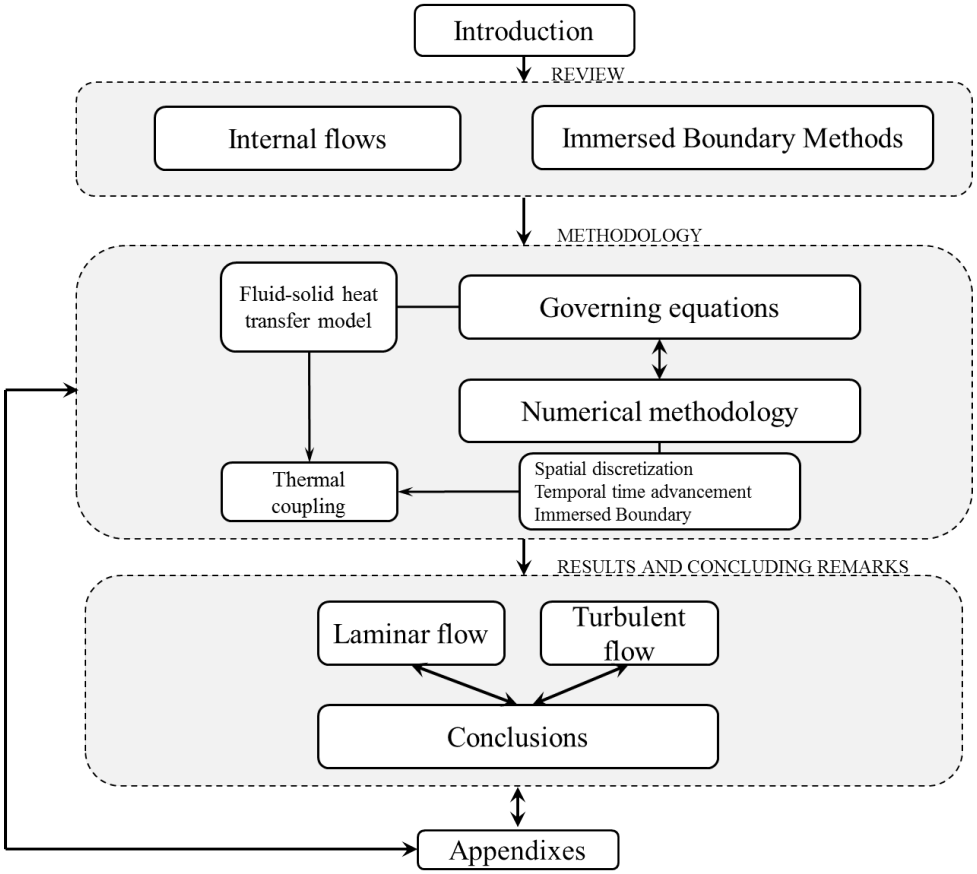

Figura 1.1: Flux-chart relating the text main topics.

As the present study deals with internal flows in the *IBM* framework, after an introduction

to the problem in this chapter (Chap. 1), the literature review is distributed into two chapters: 2. *Internal flows* and 3. *Immersed boundary methods*. Each one of these chapters describes the main highlights and, through a brief discussion, provides an introduction to the scientific problem developed throughout the text.

The second part of this work involves details on the adopted methodology. Since this is a numerical work in fluid mechanics, the second part includes two chapters: 4. *Governing equations* and 5. *Numerical methodology*. In Chapter 4, we present the mathematical models which describe the fluid dynamics and the fluid-solid heat transfer in turbulent flows. *Appendixes* contain details on the laminar solutions and deductions of the transient heat transfer equations in a periodic flow. Chap. 5 presents the numerical solution of the governing equations including spatial and temporal discretization, immersed boundary treatment, fluid-solid coupling, and the computational parallel strategy. Note that the emphasis of this chapter is on the thermal field treatment via immersed boundary method (*IBM*) and the fluid-solid thermal coupling, because the main developments are consigned in these topics.

The remaining three chapters include the verification, validation and results (Chap. 6 and 7) and conclusions (Chap. 8). In fluid-solid thermal coupling, we have made a complete study on the order of error for the laminar solution. Moreover, validations are presented in pipe/channel turbulent flows, for real fluid-solid thermal coupling and the most typical ideal thermal conditions. Despite of every chapter has a partial concluding remarks at the end, in Chapter 8, the developments and validation are discussed, concluding with the main highlights of this work.

Chapter 2

Internal flows

In internal flows, the fluid in motion is confined by solid walls. As the solid geometry is determinant in the flow characteristics, this chapter focuses on pipe and channel periodic internal flows. Channel geometry is an academic geometry which enables rigorous estimation of the formal error of the numerical scheme, while its 1D nature simplifies the methodology implementation at a first stage. On the other hand, pipe geometry is typically used in engineering designing, as heating/cooling systems and fluid distribution networks. Hence, in this chapter, some highlights on internal flow and heat transfer are reviewed briefly.

In this kind of flows, it is convenient to use the bulk velocity (U_b) which, in incompressible flows, is constant for ducts with a uniform cross-sectional area (A). In heating and cooling applications, the physical properties of the fluid could change due to the temperature field. However, for a great number of applications, these changes are not commonly considered while tolerating their impact on the solution accuracy. On the other hand, sensible thermal energy increment, related to the friction losses, is neglected, since it has usually not significant effects. The bulk velocity is defined as

$$U_b = \frac{\dot{m}}{\int_A \rho dA'} = \frac{\int_A \rho \left(\vec{V} \cdot \vec{i}\right) dA'}{\int_A \rho dA'}, \tag{2.1}$$

where $\vec{V} = [V_x \; V_y \; V_z]^T$ is the velocity field, $\dot{m}$ is the rate of mass flow, ρ is the fluid density and $\vec{i}$ is an unitary vector normal to the cross-sectional area. This expression for incompressible flow reads

$$U_b = \frac{\int_A \left(\vec{V} \cdot \vec{i}\right) dA'}{A} = \frac{Q}{A}, \tag{2.2}$$

where Q is the volumetric flow rate. Moreover, in ducts with uniform cross-sectional area, by continuity the bulk velocity is uniform along the duct and thereby it can be computed as the following volumetric-average

$$U_b = \frac{\int_\forall \left(\vec{V} \cdot \vec{i}\right) d\forall'}{\forall}, \tag{2.3}$$

where, $\forall = AL_x$ is the volume of fluid contained in a length L_x of duct.

2.1 Flow regimes

Osborne Reynolds (1842 - 1912), in former paper published in 1883[87], identified three flow regimes by injecting dye streaks inside a flow in a smooth circular pipe (Figure 2.1). By observing the dye trace patterns, for increasing velocities, he sequentially identified the following flow regimes: **laminar** (straight dye trace), **transitional** (intermittent dye trace fluctuation) and **turbulent** (high random dye trace fluctuations). Basically, the transition from laminar to turbulent flow depends on the wall roughness, duct geometry, flow velocity field, type of fluid, fluid temperature fluctuations, boundary conditions and duct vibrations. For smooth ducts, small temperature fluctuations and far from the duct boundaries, the flow regimes are dominated by the ratio of inertial ($\sim \rho U_b^2 L_c^2$) to viscous ($\sim \mu U_b L_c$) forces. From this relation, the Reynolds number is defined as

$$Re \equiv \frac{\rho U_b L_c}{\mu} = \frac{U_b L_c}{\nu}, \tag{2.4}$$

where L_c is a characteristic length and ν and μ are the cinematic and dynamic viscosity of the fluid, respectively.

In this work, the characteristic length of pipe flow is the internal diameter ($L_c = D$), while for channel flow is the internal channel height ($L_c = H$). The unstable transition regime is very sensitive to flow disturbance (e.g. wall roughness and duct vibrations) thus the critical Reynolds

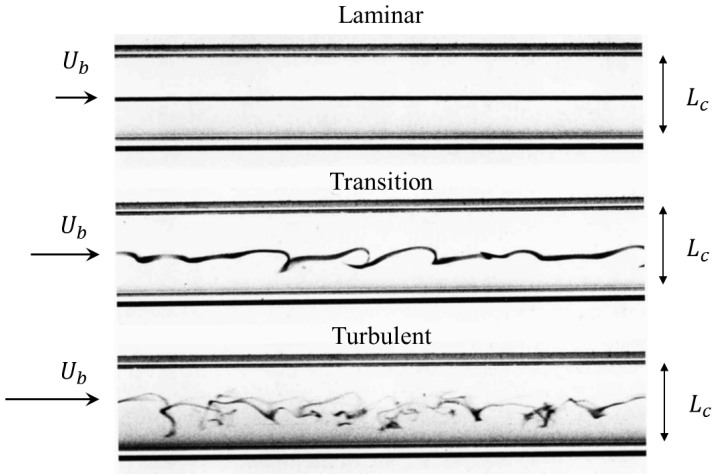

Figura 2.1: Repetition of Osborne Reynolds experiment in a pipe flow. From top to bottom, the dye trace shows the laminar, transition and turbulent flow regimes. Figure adapted from Van Dyke (1982)[102].

number (Re_c) which delimit the transition region is not easy to be experimentally well delimited, but the regimes intervals are commonly defined as

REGIME	*PIPE FLOW* [107]	*CHANNEL FLOW*
Laminar	$Re \lesssim 1760$	$Re \lesssim 1000$ [69]
Transition	$1760 \lesssim Re_c \lesssim 2300$	$1000 \lesssim Re_c \lesssim 5772$ [70]
Turbulent	$Re \gtrsim 2300$	$Re \gtrsim 5772$

(2.5)

For pipe flow, Reynolds[87] found $Re_c \approx 2000$ whereas for experiments with more disturbance control, he found $Re_c \approx 12000$. Posterior experimental studies basically confirmed this first value with estimation in the range $1760 \lesssim Re \lesssim 2300$ ([4], [54], [11]). The most recent experimental work of Mukund & Hof (2018)[65], on turbulent transition in pipe flow, shows a more narrowed transition range: $2020 < Re_c < 2060$. On the other hand, by suppressing even further the flow disturbances in smooth pipes, it has been experimentally shown that the laminar regime can be maintained up to $Re = 10^5$ ([79]).

It should be pointed out that, a linear stability analysis shows that pipe flow is stable ([113]), whereas channel flow is stable up to $Re_c \approx 5772$ ([70]). Experimental ([91]) and numerical ([100]) studies in channel flow have shown that the lower bound of the subcritical transitional regime is $Re \approx 840$.

2.2 Pressure loss in ducts

The net viscous friction force at the wall, far from the entrance influence, yields a linear pressure drop (fully developed flow region, Figure 2.2). From a momentum balance in an infinitesimal duct length (dx), the cross-sectional averaged pressure gradient loss in streamwise direction can be expressed as

$$\left(\frac{1}{\rho}\right)\frac{d\langle p\rangle}{dx} = -\frac{\langle\tau_w\rangle}{\rho}\frac{P}{A} + g\frac{dy}{dx}. \tag{2.6}$$

where τ_w is the shear wall stress, P is the wall perimeter, A is the cross-sectional flow area, dy/dx is the duct slope and $\langle\cdot\rangle$ denotes an average operator in azimuthal/spanwise and/or time.

Defining the (non-physical) friction velocity as

$$u_\tau \equiv \left(\frac{\tau_w}{\rho}\right)^{1/2}, \tag{2.7}$$

the duct slope, when the mean pressure gradient is null, is

$$\frac{dy}{dx} = \frac{\langle u_\tau\rangle^2}{gD_h} = Fr_\tau^2, \tag{2.8}$$

where $D_h = A/P$ is the ratio of the cross-sectional area to the wall perimeter and $Fr_\tau = \dfrac{\langle u_\tau\rangle^2}{gD_h}$ is a Froude number based on the friction velocity. This expression represents the slope that a duct must have to ensure null mean pressure gradient. On the other hand, the dimensionless pressure gradient loss for incompressible flow in horizontal ducts ($dy/dx = 0$) is given by

$$\frac{d\langle\Pi\rangle}{dx} = \frac{d}{dx}\left(\frac{\langle p\rangle}{\rho U_b^2}\right) = -\left(\frac{u_\tau}{U_b}\right)^2\frac{L_c}{D_h}. \tag{2.9}$$

Note: For notational convenience and simplicity, in this expression and in the rest of the text, the derivative operators are dimensionless, although the notation relative to the dimensional operator in Eq. 2.6 did not change. Besides, the notation u_τ is be considered as representing an averaged friction velocity $\langle u_\tau\rangle$.

In wall-bounded flows, it is convenient to work with the quantities non-dimensionalized by the friction velocity (in wall units). Then, the Reynolds number based on u_τ is

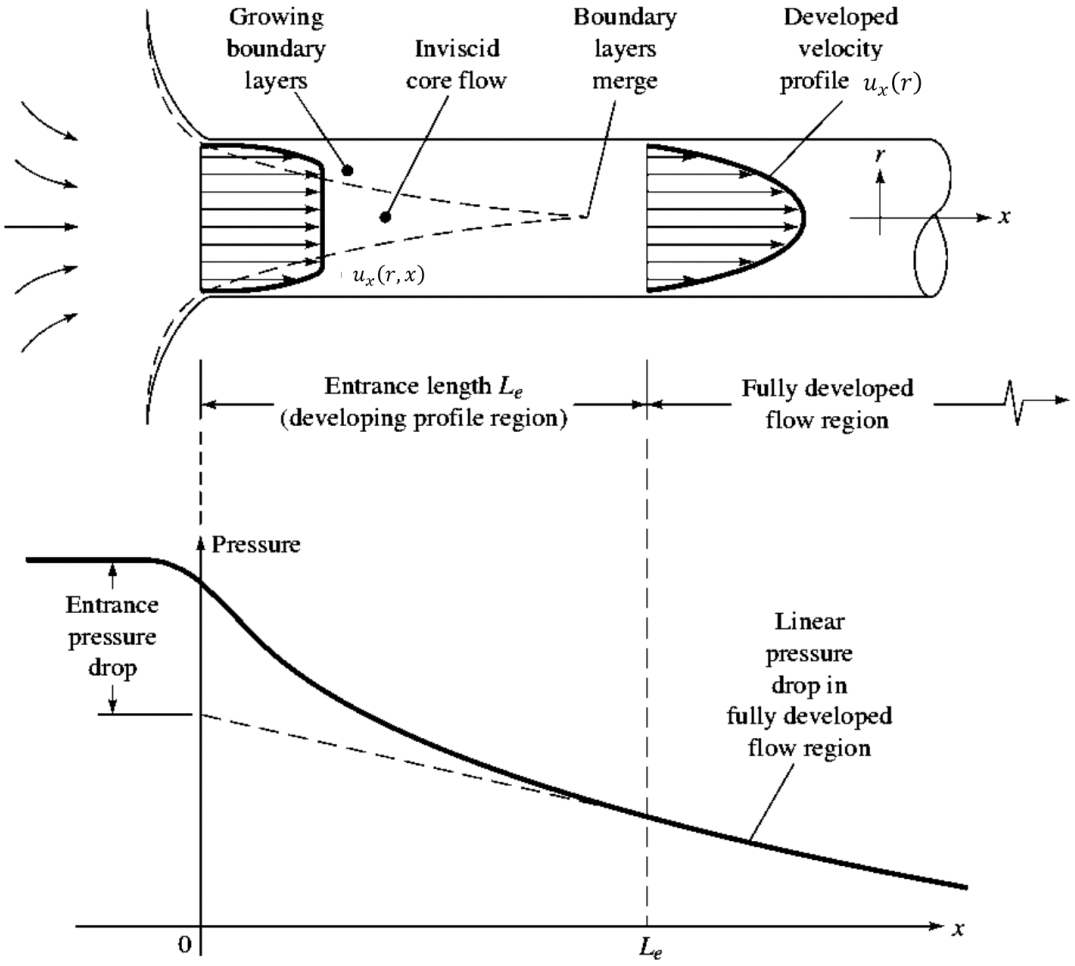

Figura 2.2: Developing streamwise velocity profile $u_x(r,x)$ and pressure drop in a duct. The schematic is exemplifying a uniform circular duct (pipe flow) with radial coordinate r and axial coordinate x. The same results can be extended to any uniform cross-sectional geometry. Figure adapted from White 2011[107].

$$Re_\tau \equiv \frac{u_\tau (L_c/2)}{\nu}, \tag{2.10}$$

which is also so-called friction Reynolds number. The streamwise velocity in wall units is defined as

$$u_x^+ = \frac{V_x}{u_\tau}, \tag{2.11}$$

and the distance to the wall (y) in wall units is

$$y^+ = \frac{y u_\tau}{\nu}. \tag{2.12}$$

From the definition of the friction Reynolds number and the global Reynolds number (Eq. 2.4), the expression 2.9 can be rewritten as

$$\frac{d\langle\Pi\rangle}{dx} = -\left(2\frac{Re_\tau}{Re}\right)^2 \frac{L_c}{D_h}. \tag{2.13}$$

2.3 Velocity profile in wall-bounded flows

As a function of the distance to the wall, three flow layer can be identified: (i) viscous wall layer or inner layer, (ii) outer layer and (iii) overlap layer (Figure 2.3). In the inner layer, the velocity profile follows the linear viscous relation

$$u_x^+ = y^+ \ \ (Inner \ \ layer). \tag{2.14}$$

This expression is valid for $y^+ < 5$, and then it is itself curved over to merge with the following logarithmic law

$$u_x^+ = \frac{1}{\kappa} ln\,(y^+) + B \ \ (Overlap \ \ layer), \tag{2.15}$$

for $y^+ > 30$. The accepted values for the constants are: $\kappa \approx 0.41$ and $B = 5$ *to* 6. The outer turbulent layer is sensitive to pressure variations, but the velocity profile is represented mostly by the logarithmic law of the wall (Figure 2.4).

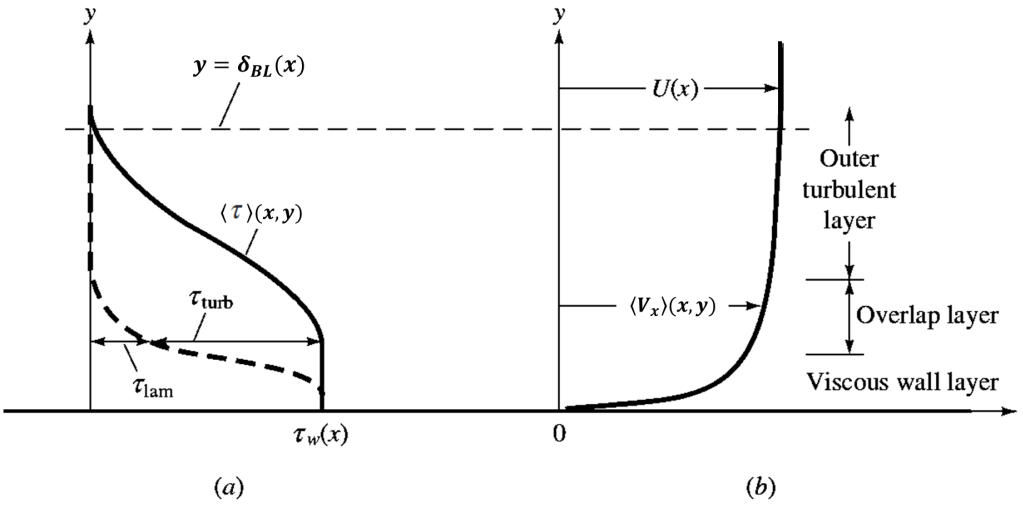

Figura 2.3: (a) Shear stress and (b) velocity profiles in wall-bounded flow. Figure adapted from White 2011[107].

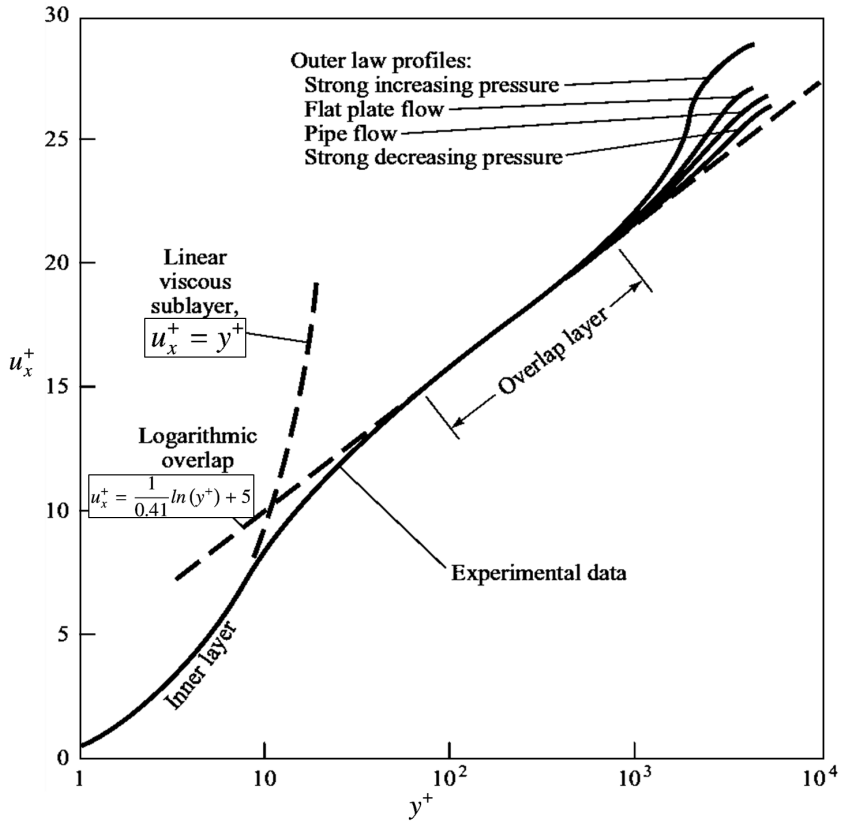

Figura 2.4: Experimental verification of the inner, outer, and overlap layer laws relating streamwise velocity profiles in turbulent wall-bounded flows. Figure adapted from White 2011[107].

2.4 Heat transfer in wall-bounded flow

In following, the governing equations and some previous studies are briefly discussed, in order to establish the current scientific knowledge on heat transfer problem in turbulent flows, particularly in internal flow, and to have a starting point to validate our numerical developments.

In internal flows, the convection energy rate can be obtained by integrating the product of mass flux $\rho\left(\vec{V}\cdot\vec{i}\right)$ and the thermal energy (or enthalpy) per unit mass c_pT, over the cross section A. From the convection rate, the bulk temperature is conveniently defined as

$$T_b \equiv \frac{1}{c_p\dot{m}}\int_A \rho\left(\vec{V}\cdot\vec{i}\right)c_pTdA', \tag{2.16}$$

where $\dot{m} = \int_A \rho u_x dA' = \rho U_b A$ is the mass flow rate and c_p is the fluid heat capacity ar constant pressure. Under the assumptions of passive scalar, incompressible flow and uniform duct cross

section, Equation 2.16 can be rewritten as

$$T_b = \frac{1}{U_b A} \int_A \left(\vec{V} \cdot \vec{i}\right) T dA', \tag{2.17}$$

It means that the cross-sectional bulk temperature is identical to the volumetric bulk temperature. It should note that, for incompressible flow, the heat capacity under constant pressure c_p is equal to the heat capacity in constant volume c_v. Furthermore, if the temperature T is uniform along the duct the bulk temperature can be expressed by the following volumetric-average

$$T_b = \frac{1}{U_b \forall} \int_\forall \left(\vec{V} \cdot \vec{i}\right) T d\forall'. \tag{2.18}$$

2.4.1 Dimensional heat transfer equations

Most commonly, the temperature fluctuations in a moving fluid are considered not to modify the fluid physical or thermal properties, then it is said that the temperature T is transported as a *passive scalar*. Thus, the thermal energy balance **inside the fluid** can be expressed by mean a convection-diffusion equation of the temperature driven by the incompressible velocity field $\vec{V}$ ($\nabla \cdot \vec{V} = 0$), as it follows

$$\frac{\partial T}{\partial t} = -\vec{V} \cdot \nabla \vec{T} + \alpha \nabla^2 T, \qquad \text{in the fluid,} \tag{2.19}$$

where, $\alpha = \lambda/(\rho c_p)$ and λ are the thermal diffusivity and conductivity of the fluid, respectively. The first term, on the right-hand side of the equation, accounts for heat transported by fluid convection, while the second term refers to the heat transported by conduction. Under the same assumptions, the energy equation **inside the solid** can be expressed in terms of the solid temperature field T_s, by the following heat conduction equation

$$\frac{\partial T_s}{\partial t} = \alpha_s \nabla^2 T_s, \qquad \text{in the solid,} \tag{2.20}$$

where α_s is the thermal diffusivity of the solid. The energy equations inside the fluid and solid domains (Eq. 2.19 and 2.20) are coupled by the **thermal boundary conditions** at the fluid/solid

interface. On the fluid/solid interface ($|_{int}$), it must be verified the physical **temperature continuity**

$$T|_{int} = T_s|_{int}\,, \tag{2.21}$$

and the **continuity of the temperature derivative** normal to the interface (derivate from energy conservation through the interface)

$$\lambda_s \left.\frac{\partial T_s}{\partial \vec{n}}\right|_{int} = \lambda \left.\frac{\partial T}{\partial \vec{n}}\right|_{int}, \tag{2.22}$$

where λ_s is the conductivity of the solid and $\vec{n}$ is an unitary vector normal to the interface pointing towards the fluid.

After the presentation of the governing differential equations of energy and their respective boundary conditions, maybe the immediate question is: which and where is the heat source or sink? In internal flows, the heat source/sink typically acts on a surrounding fluid which transfers heat through the *external fluid/solid interface* of the duct. In this case, three approaches are commonly followed:

1. the temperature inside the solid, the internal fluid and the surrounding fluid is solved for a given external heat source applied at the **domain boundary** or at some point of the **external still fluid**;

2. the temperature inside the internal fluid and the solid is solved, and the heat source is defined by the thermal boundary condition on the **external fluid-solid interface**, which can be selected according to the dominant process: *isothermal process* (e. g. fluid phase change) or *isoflux of heat process* (e. g. cooling or heating systems);

3. only the internal flow is solved and the heat source is represented by the boundary condition directly imposed on the **internal fluid/solid interface**.

The fluid/solid coupling modeled by the two first approaches has been so-called *Conjugate heat transfer* (*CHT*). In *CHT* conditions, the equations of energy are solved and coupled either

in the solid or in the fluid domain (Eq. 2.19, 2.20, 2.21 and 2.22). The third approach, referred here as *ideal locally imposed* condition, is the most commonly applied. However, it only considers the energy transport in the fluid while prescribing a thermal boundary condition at the internal interface. Those ideal boundary conditions are an adequate representation of the thermal process dominated by uniform conditions, as *isothermal* or *isoflux* processes.

Ideal locally imposed conditions

On the fluid-solid interface can be prescribed the temperature (*ideal locally imposed temperature*)

$$T = T|_{int} \quad on \quad the \quad interface, \tag{2.23}$$

or the heat flux (*ideal locally imposed heat flux*)

$$\lambda \frac{\partial T}{\partial \vec{n}} = \varphi|_{int} \quad on \quad the \quad interface. \tag{2.24}$$

It should be noted that the prescribed temperature ($T|_{int}$) or heat flux ($\varphi|_{int}$) are not necessary non-fluctuating (in time) and uniform (in space). For instance, in a duct heated by thick solid in contact with a surrounding fluid in phase change, the hypothesis of non-fluctuating and uniform temperature at the interface could be adequate (*isothermal* process). On the other hand, in a cooling system, under certain conditions, the wall temperature along the duct is linearly increasing, while the wall heat flux is approximately non-fluctuating and uniform (*isoflux* process). The *isoflux* process at the wall can be modeled by imposing a non-fluctuating and linearly increasing wall temperature (Dirichlet-type boundary condition, *DBC*) or by prescribing a non-fluctuating and uniform heat flux (Neumann boundary condition, *NBC*). According to Tiselj *et al.* (2001)[97], the *DBC* corresponds to the physical configuration in which a fluid with negligible density, heat capacity and thermal conductivity, is heated by a thick wall with high density, heat capacity and thermal conductivity (thermal activity ratio $K = \sqrt{(\rho c_p \lambda)/(\rho_s c_{p_s} \lambda_s)} \longrightarrow 0$). Conversely, the *NBC* represents a hypothetical or ideal case in which thermal activity ratio is infinity ($K = \infty$). As in practice, there are several cases of interest, many other configurations

of thermal boundary conditions, based on the *ideal locally imposed* conditions, has been also employed (Table 2.1).

Tabela 2.1: Overview of turbulent heat transfer in wall-bounded flows. Table adapted from Saha *et al.* (2011)[88].

Previous DNS	Re_τ	Pr	Boundary conditions
Channel flows			
Kim and Moin (1989)	180	[0.1, 0.71, 2.0]	UHG[1], UTD[2], PF[9]
Lyons et al. (1991)	150	1.0	UTD[2], CF[10]
Kasagi et al. (1992)	150	0.71	MBC[3], PF[9]
Kasagi and Ohtsubo (1993)	150	0.025	MBC[3], PF[9]
Kawamura et al. (1997)	180	[0.025, 0.05, 0.1, 0.2, 0.4, 0.6, 0.71, 1.0, 1.5, 5.0]	MBC[3], PF[9]
Abe et al. (1998)	[180, 395]	[(0.025, 0.1, 0.2, 0.4, 0.71, 5.0), (0.025, 0.2, 0.71)]	MBC[3], PF[9]
Matsubara et al. (1998)	150	[0.1, 0.3, 0.71, 1.5]	SMTG[4], PF[9]
Kawamura et al. (1998a)	180	[0.025, 0.05, 0.1, 0.2, 0.4, 0.6, 5.0]	MBC[3], PF[9]
Kawamura et al. (1998b)	180	[0.025, 0.05, 0.1, 0.2, 0.4, 0.6, 0.71, 1.0, 1.5, 5.0]	MBC[3], PF[9]
Kawamoto and Kawamura (1998)	180	[0.025, 0.05, 0.4, 0.71]	SMTG[4], PF[9]
Kawamoto and Kawamura (1999a)	180	[0.025, 0.71]	UTD[2], MBC[3], PF[9]
Kawamoto and Kawamura (1999b)	[180, 395]	[(0.025, 0.05, 0.1, 0.2, 0.4, 0.6, 5.0), (0.025, 0.2, 0.71)]	MBC[3], PF[9]
Kawamura et al. (1999)	[180, 395]	[0.025, 0.2, 0.71]	MBC[3], PF[9]
Matsubara et al. (1999)	150	0.71	SMTG[4], PF[9]
Johansson and Wikström (1999)	265	0.71	UTD[2], PF[9]
Na et al. (1999)	150	[0.3, 1.0, 3.0, 10.0]	UTD[2], PF[9]
Na and Hanratty (2000)	150	[1.0, 3.0, 10.0]	UTD[2], PF[9]
Kawamura et al. (2000)	[180, 395]	[(0.025, 0.2, 0.71, 1.0), (0.025, 0.2, 0.71, 1.0)]	UTD[2], MBC[3], PF[9], CF[10]
Kawamura and Ogawa (2001)	180	0.71	UTD[2], SMTG[4], CWTDSMTG[5], PF[9]
Matsubara et al. (2001)	150	0.71	MBC[3], SMTG[4], PF[9]
Piller et al. (2002)	150	[0.025, 0.05, 0.1, 0.3, 1.0]	UTD[2], PF[9]
Kawamura and Abe (2002)	[180, 395, 640]	[0.025, 0.71]	MBC[3], PF[9]
Abe and Kawamura (2002)	[180, 395, 640]	[0.025, 0.71]	MBC[3], PF[9]
Seki et al. (2003a)	[180, 395]	0.71	UTD[2], MBC[3], PF[9]
Seki et al. (2003b)	180	0.71	UTD[2], MBC[3], CWTDSMTG[5], PF[9]
Abe et al. (2004)	[180, 395, 640, 1020]	[0.025, 0.71]	MBC[3], PF[9]
Tsukahara et al. (2004)	[64, 70, 80, 110, 150, 180]	0.71	MBC[3], PF[9]
Kawamura et al. (2004)	[180, 395, 640, 1020]	[0.025, 0.71]	MBC[3], PF[9]
Seki and Kawamura (2004a)	180	0.71	SVTBC[6], PF[9]
Seki and Kawamura (2004b)	180	0.71	UTD[2], MBC[3], CWTDSMTG[5], PF[9]
Seki and Kawamura (2005)	180	0.71	SVTBC[6], PF[9]
Seki and Kawamura (2006)	180	0.71	SVTBC[6], PF[9]
Seki et al. (2006)	180	[0.71, 1.0, 2.0, 10.0]	MBC[3], PF[9]
Abe et al. (2008)	[180, 395, 640]	0.71	MBC[3], PF[9]
Antonia et al. (2008)	[180, 395, 640, 1020]	0.71	MBC[3], PF[9]
Yamamoto et al. (2009)	[150, 1000, 2000]	5.0	UTD[2], PF[9]
Pipe flows			
Satake et al. (2000)	[150, 180, 360, 500, 1050]	0.71	MBC[3], PF[9]
Piller (2005)	180	0.71	IWT[7], IWHF[8], MBC[3], PF[9]
Redjem-Saad et al. (2007)	186	[0.026, 0.1, 0.2, 0.4, 0.71, 1.0]	MBC[3], PF[9]
Saha et al. (2010)	170	[0.026, 0.1, 0.2, 0.4, 0.71, 1.0]	MBC[3], PF[9]

[1] USG: uniform heat generation with cold isothermal walls.
[2] UTD: uniform temperature difference (constant wall temperature difference).
[3] MBC: mixed boundary condition (wall temperature is time independent and varies linearly along streamwise direction).
[4] SMTG: spanwise mean temperature gradient (time-averaged wall temperature is uniform in streamwise and wall-normal direction).
[5] CWTDSMTG: constant wall temperature difference imposed with spanwise mean temperature gradient.
[6] SVTBC: streamwise varying thermal boundary condition.
[7] IWT: ideal isothermal boundary condition (time-averaged wall temperature is uniform and constant).
[8] IWHF: ideal isoflux boundary condition (time-averaged wall temperature varies linearly along streamwise direction).
[9] PF: Poiseuille flow.
[10] CF: Couette flow.

2.4.2 Dimensionless heat transfer equations

Several of the previous studies (Tables 2.1, 2.2, 2.3) have focused on stationary periodic internal flows, far from the entrance region, e. i., along the duct region where the thermal boundary layer is completely developed (*thermally fully developed flow*, see Figure 2.5). It means

Tabela 2.2: Computational parameters for previous wall-bounded DNS studies with imposed linear temperature along the duct wall. Table adapted from Saha *et al.* (2011)[88].

Previous DNS	Re_τ	Pr	L/δ	l^+	Δx^+	$\Delta z^+/\Delta r^+$	$\Delta y^+/\Delta(r\theta)^+$
Channel flows							
Kasagi et al. (1992)	150	0.71	5π	2356.2	18.4	[0.08, 4.9]	7.4
Kasagi and Ohtsubo (1993)	150	0.025	5π	2356.2	18.4	[0.08, 4.9]	7.4
Abe et al. (1998)	180	[0.025, 0.1, 0.2, 0.4, 0.71, 5.0]	6.4	1152	9.0	[0.40, 11.5]	4.5
	395	[0.025, 0.2, 0.71]	6.4	2528	9.88	[0.44, 13.0]	4.94
Kawamura et al. (1998b)	180	[0.025, 0.05, 0.1, 0.2, 0.4, 0.6, 0.71, 1.0, 1.5]	6.4	1152	9.0	[0.40, 11.5]	4.5
	180	5.0	6.4	1152	4.5	[0.20, 5.90]	2.25
Kawamoto and Kawamura (1999a)	180	[0.025, 0.71]	6.4	1152	9.0	[0.40, 11.5]	4.5
Kawamura et al. (1999)	180	[0.025, 0.2, 0.71]	6.4	1152	9.0	[0.40, 11.5]	4.5
	395	[0.025, 0.2, 0.71]	6.4	2528	9.88	[0.44, 13.0]	4.94
Kawamura et al. (2000)	180	[0.025, 0.2, 0.71]	6.4	1152	9.0	[0.40, 11.5]	4.5
	180	1.0	6.4	1152	4.5	[0.20, 5.90]	2.25
	395	[0.025, 0.71]	6.4	2528	9.88	[0.44, 13.0]	4.94
	395	[0.2, 1.0]	6.4	2528	9.88	[0.20, 9.46]	4.94
Matsubara et al. (2001)	150	0.71	7.85	1177.5	18.4	[1.03, 9.51]	7.36
Kawamura and Abe (2002)	180	[0.025, 0.71]	12.8	2304	9.0	[0.20, 5.90]	4.5
	395	[0.025, 0.71]	12.8	5056	9.88	[0.15, 6.52]	4.94
	640	[0.025, 0.71]	12.8	8192	8.00	[0.15, 8.02]	4.00
Seki et al. (2003a)	180	0.71	12.8	2304	9.0	[0.20, 5.90]	4.5
	395	0.71	12.8	5056	9.88	[0.15, 6.52]	4.94
Kawamura et al. (2004)	180	[0.025, 0.71]	12.8	2304	9.0	[0.20, 5.90]	4.5
	395	[0.025, 0.71]	12.8	5056	9.88	[0.15, 6.52]	4.94
	640	[0.025, 0.71]	12.8	8192	8.00	[0.15, 8.02]	4.00
	1020	[0.025, 0.71]	12.8	13056	6.38	[0.15, 7.32]	4.25
Tsukahara et al. (2004)	64	0.71	25.6	1638.4	6.40	[0.071, 2.11]	3.20
	70	0.71	25.6	1792	7.00	[0.078, 2.31]	3.50
	80	0.71	51.2	4096	4.00	[0.111, 3.59]	3.52
	80	0.71	12.8	1024	4.00	[0.089, 2.64]	2.00
	110	0.71	12.8	1408	5.50	[0.123, 3.62]	2.75
	150	0.71	12.8	1920	7.50	[0.167, 4.94]	3.75
	180	0.71	12.8	2304	9.00	[0.201, 5.93]	4.50
Seki et al. (2006)	180	[0.71, 1.0, 2.0, 10.0]	6.4	1152	1.1	[0.05, 1.0]	1.1
Antonia et al. (2008)	180	0.71	12.8	2304	3.00	[0.20, 5.90]	3.00
	395	0.71	12.8	5056	3.29	[0.15, 6.52]	3.29
	640	0.71	12.8	8192	4.00	[0.15, 8.02]	4.00
	1020	0.71	12.8	13056	6.38	[0.15, 7.32]	4.25
Kozuka et al. (2009)	180	[0.71, 1.0, 2.0, 10.0]	6.4	1152	1.13	[0.0504, 0.972]	1.13
	180	[7.0, 10.0]	6.4	1152	0.563	[0.0504, 0.972]	1.13
	395	[0.71, 1.0, 2.0, 5.0, 7.0, 10.0]	6.4	2528	1.23	[0.111, 2.13]	2.47
Pipe flows							
Satake et al. (2000)	150	0.71	15	2250	8.78	[0.24, 0.86]	7.36
	180	0.71	15	2700	10.5	[0.29, 1.04]	8.84
	360	0.71	15	5400	14.0	[0.11, 1.1]	8.83
	500	0.71	15	7500	14.6	[0.1, 2.6]	8.18
	1050	0.71	15	15750	15.4	[0.163, 4.16]	8.59
Piller (2005)	180	0.71	12.656	2278	7.03		6.28
Redjem-Saad et al. (2007)	186	0.026	15	2790	20	[0.01, 7]	10
	186	[0.1, 0.2, 0.4, 0.71, 1.0]	15	2790	10	[0.01, 5]	10
Saha et al. (2010)	170	[0.026, 0.1, 0.2, 0.4, 0.71, 1.0]	4π	2148.8	14.3	[0.5, 3.6]	8.4

Tabela 2.3: Recent works of turbulent heat transfer in internal flow.

Previous DNS	Pr	Re_τ	Re	L_x	n_x	$n_{r,y}$	$n_{\theta,z}$	Δx^+	Δy^+	$\Delta(R\theta)^+$
Pipe flow										
Saha *et al.* (2011)[88]	0.025, 0.71, 2.0	≈ 170	5000	$2\pi D$	256	128	128	10.5	0.29 ~ 1.04	8.84
Saha *et al.* (2014)[89]	1.0	≈ 186	5500	$7.5D$	301	121	128	9.3	0.0649 ~ 4.8	3.13
Channel flow										
Tiselj *et al.* (2001)[97]	0.71	≈ 150	5560	$5\pi H/2$	128	97	65	18.4	0.08 ~ 4.9	7.4
Flageul (2015)[16]	0.71	≈ 149	5560	$25.6H/2$	256	193	256	14.8	0.049 ~ 4.8	5.1

that, the temperature profiles are similar along the duct, although the streamwise gradients of the local temperature ($\partial T/\partial x$) and the bulk temperature (dT_b/dx) are not necessarily nulls. For instance, if an infinite channel flow constantly heated is considered, the bulk temperature in-

creases linearly with x. A change of variable is used, to compensate this linear increase and to allow periodicity in the streamwise direction. This gives rise to the source term in the fluid energy equation.

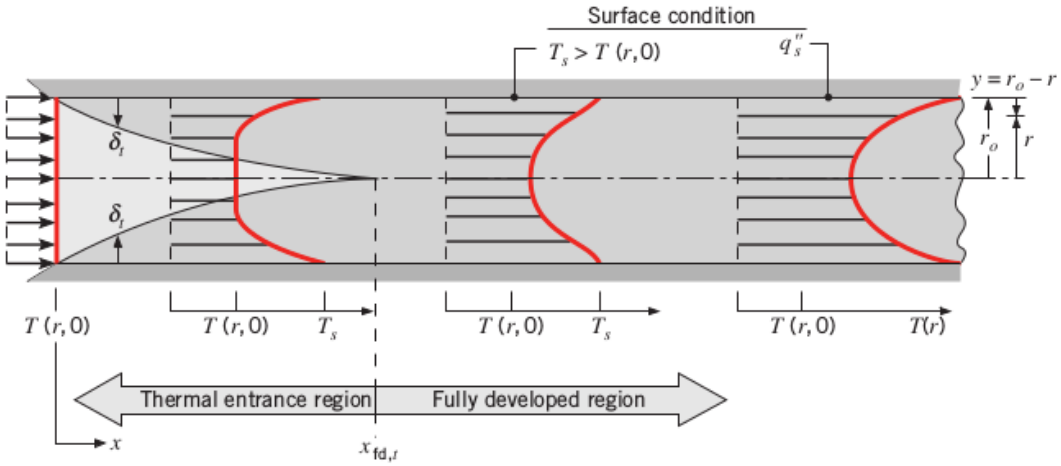

Figura 2.5: Thermal boundary layer development in a heated circular tube (Incropera & Dewit, 2000[32]).

Taking advantage from the linearity of the temperature equations (Eq. 2.19 and 2.20), the following linear transformation (non-dimensionalization) can be applied to the dimensional fluid temperature T, in order to deal with a single normalized temperature field,

$$\Theta(x,y,z,t) = \frac{\langle T|_{int}\rangle(x) - T(x,y,z,t)}{\langle T|_{int}\rangle(x) - T_b(x)}. \tag{2.25}$$

Considering that the geometrical quantities are non-dimensionalized with the reference length L_c (diameter for pipe and height for channel), the velocity field with the bulk velocity ($\vec{u} = \vec{V}/U_b$), the time with the ratio L_c/U_b and applying the transformation defined in Eq.2.25 to **fluid temperature equation** (Eq. 2.19), the following dimensionless temperature transport equation is yielded

$$\frac{\partial\Theta}{\partial t} = -\vec{u}\cdot\vec{\nabla}\Theta + \frac{1}{RePr}\nabla^2\Theta + f_\Theta, \quad in\ \ the\ \ fluid, \tag{2.26}$$

where $Pr = \nu/\alpha$ is the Prandtl number which relates the viscosity (ν) with the thermal diffusivity (α) of the fluid. The quantity f_Θ acts as a source/sink term which maintains stationary thermal behavior or, equivalently, constant bulk dimensionless temperature (Θ_b) along the duct. On the

other hand, the energy transport dimensionless equation **inside the solid** reads

$$\frac{\partial \Theta_s}{\partial t} = \frac{1}{GRePr}\nabla^2\Theta_s \;\; in \;\; the \;\; solid. \tag{2.27}$$

where $G = \lambda\rho_s c_{ps}/(\lambda_s \rho c_p)$ is the fluid-to-solid ratio of thermal diffusivities.

The energy transport equations inside the fluid and solid domains are coupled by the **thermal boundary conditions** at the fluid/solid *interface*

$$\Theta|_{int} = \Theta_s|_{int}\,, \tag{2.28}$$

$$\left.\frac{\partial \Theta_s}{\partial \vec{n}}\right|_{int} = \frac{1}{G_2}\left.\frac{\partial \Theta}{\partial \vec{n}}\right|_{int}, \tag{2.29}$$

where Θ_s is the solid temperature and $G_2 = \lambda_s/\lambda$ is the ratio of thermal conductivities. It should be pointed out that, for simplicity, the notation of the differential operators is the same for the dimensional and dimensionless forms. More details on the dimensionless procedure of the temperature can be found in Appendix A.

2.4.3 Dominant parameters

The difficult to measure experimentally turbulent quantities, in very thin boundary layers (Saha *et al.*, 2014[89]), makes numerical simulation a powerful and useful tool to study instantaneous turbulent flow structures (Kasagi, 1995[38]). During the validation procedure, the computational fluid dynamic results are evaluated in relation to the real world physical observations. However, Saha *et al.* 2014[89] establish the following useful criteria for validating Direct Numerical Simulation (*DNS*), with numerical data available in the literature.

The space-time thermal distribution strongly depends on the thermal boundary condition, the friction Reynolds number number (Re_τ) and the Prandtl number (Pr), while the streamwise length of the computational domain (L_x) and the simulation time are decisive for the statistics convergence.

The usual ideal thermal conditions at the wall, which consider *imposed* temperature (*DBC*) or heat flux (*NBC*), correspond to the physical configuration in which thermal activity ratio

$K \longrightarrow 0$ and $K \longrightarrow \infty$, respectively. The influence of these assumptions is reflected in the temperature fluctuations which increase nearby the wall with increasing thermal activity ratio (Figure 2.6).

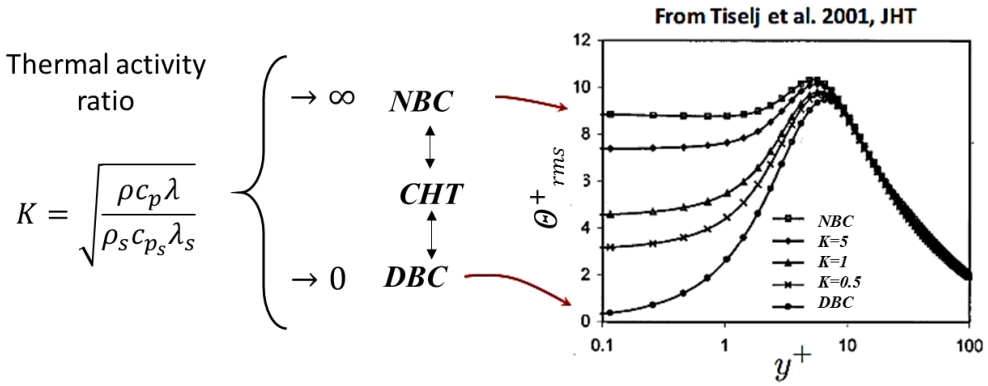

Figura 2.6: Influence of the thermal activity ratio influence in temperature fluctuations in a channel flow. Uniform heat flux imposition and linear temperature imposition corresponds to the physical configurations with very high and very low activity ratio, respectively.

The mean and fluctuating temperature strongly depend on Re_τ for approximately $y^+ > 10$(Figure 2.7). The root mean square (*rms*) of the temperature fluctuation is shifted away from the pipe center with increasing Re_τ (Saha *et al.*, 2014[89]). On the other hand, according to Redjem-Saad *et al.* (2007)[84], the mean temperature and temperature fluctuations increase with increasing values of Pr (Figure 2.8). For $Pr > 1$, temperature fluctuations at the wall do not affect heat transfer and the average velocity and temperature profiles are similar (Kasagi *et al.*, 1989[37]; Li *et al.*, 2009[56]).

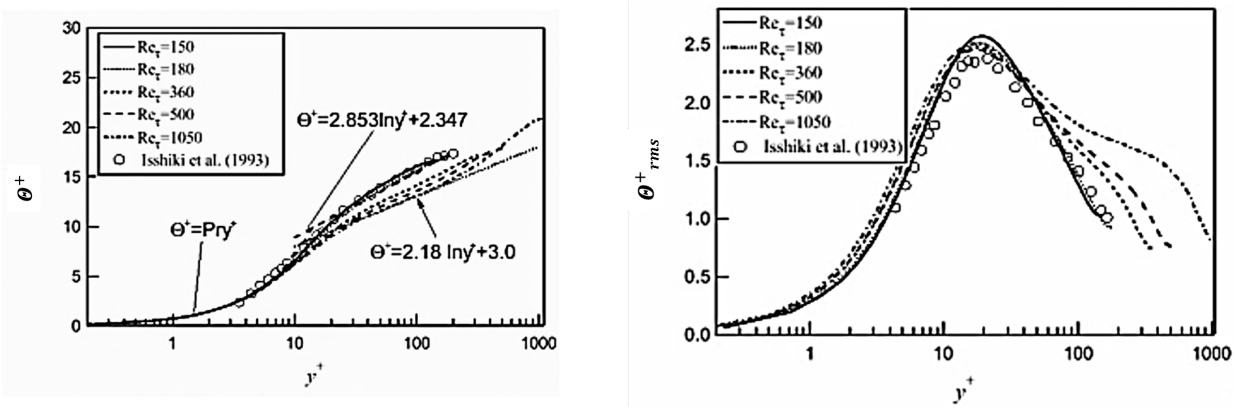

Figura 2.7: Mean and fluctuating temperature profile (in wall-units) for different values of Re_τ at $Pr \approx 1$ (Satake *et al.*, 2000[92]).

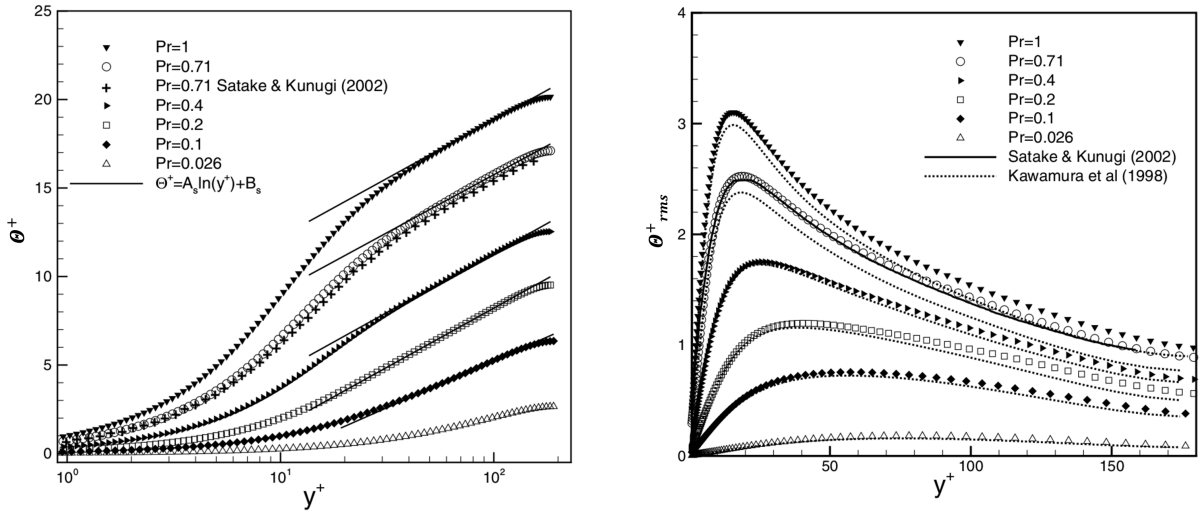

Figura 2.8: Temperature statistics in wall-units for different values of Pr at $Re_\tau \approx 186$ ($Re = 5500$). Mean (left) and fluctuating (right) temperature profile. Figure adapted from RedjemSaad *et al.* (2007)[84].

Tables 2.1, 2.2 and 2.3 summarize some parameters used in precedents studies on heat transfer in pipe and channel flow. For the range of parameters defined in Saha *et al.* (2011)[88], it was found that the convergence of the first and second order thermal statistics is achieved for a minimum pipe length of $L_x = 2\pi$.

The mesh resolution effect, on the first and second order thermal statistics, is practically negligible if it is compared with the Re_τ, Pr and L_x/D effects (Saha et al., 2011-2014[88][89]). Furthermore, in pipe and channel flows, the thermal boundary conditions modify the temperature statistics profiles (Piller, 2005[80]; Flageul *et al.*, 2015[17]).

According to Saha *et al.* (2014)[89], some deviations could appear at the pipe center when a cylindrical mesh is used. This depends on the strategy to overcome the singularity at the pipe center. Certainly, in codes based on a Cartesian mesh, as *Incompact3d* [48], this singularity is naturally bypassed.

2.5 Concluding remarks

This study is focused on **internal flows** with **heat transfer**, specifically on channel and pipe **periodic flows**. To describe this kind of flows, the bulk velocity U_b and the bulk temperature T_b are important quantities. U_b is the velocity averaged in space (cross section or duct volume) while T_b can be defined as average temperature pondered by the streamwise velocity. The Reynolds number approximately defines if the flow is in laminar, turbulent or a transition regime between these states. It is commonly accepted that the transition in pipes occurs in the interval $1760 \lesssim Re = U_b D/\nu \lesssim 2300$ and in channels $500 \lesssim Re = U_b H/\nu \lesssim 2886$. In wall-bounded flows, it is convenient to work with the quantities scaled by the (non-physical) friction velocity defined as $u_\tau = \left(\frac{\tau_w}{\rho}\right)^{1/2}$. Then, the Reynolds number based on u_τ is $Re_\tau \equiv \frac{u_\tau (L_c/2)}{\nu}$. The net viscous friction at the wall, without entrance influence, yields a linear pressure drop which can be compensated by a **streamwise momentum forcing term**, in order to maintain the periodic flow **statistically stationary**.

As a function of the distance to the wall y^+, three flow layer can be identified: viscous wall layer or inner layer, outer layer and overlap layer. In the inner layer ($y^+ < 5$), the velocity profile follows the linear viscous relation $u_x^+ = y^+$ and the logarithmic law $u_x^+ = \frac{1}{\kappa} ln\,(y^+) + B$, in the overlap layer ($y^+ \geq 30$). The values accepted for the constants are: $\kappa \approx 0.41$ and $B = 5 - 6$. Despite of The outer turbulent layer is sensitive to pressure variations, the **velocity profile** is represented mostly by such a **logarithmic law of the wall**.

Under certain conditions, the temperature fluctuations in the moving fluid can be considered not to modify the fluid physical or thermal properties, then it is said that the temperature T (energy) is transported as a *passive scalar*. Thus, the temperature transport is modeled by a convection-diffusion equation **inside the fluid**, a conduction equation **inside the solid** and temperature and heat flux **continuity at the interface**. Hence, the dimensionless governing equations for energy transport are

$$
\begin{aligned}
&\text{in the fluid:} && \frac{\partial \Theta}{\partial t} = -\vec{u} \cdot \vec{\nabla}\Theta + \frac{1}{RePr}\nabla^2\Theta + f_\Theta, \\
&\text{in the solid:} && \frac{\partial \Theta_s}{\partial t} = \frac{1}{GRePr}\nabla^2\Theta_s + f_{\Theta_s}, \\
&\text{at the interface:} && \Theta|_{int} = \Theta_s|_{int}, \\
&\text{at the interface:} && \frac{\partial \Theta_s}{\partial \vec{n}}\Big|_{int} = \frac{1}{G_2}\,\frac{\partial \Theta}{\partial \vec{n}}\Big|_{int}.
\end{aligned}
$$

Just as the momentum streamwise forcing term in the fluid motion equations, the quantity f_Θ acts as a **heat source/sink term** which maintains stationary thermal behavior or, equivalently, constant bulk dimensionless temperature (Θ_b) along the duct. More details on the non-dimensionalization procedure of the temperature can be found in Appendix A.

Assuming a flow configuration in a duct surrounded by a heated/cooled still fluid, the internal/external fluids and the solid are solved. The fluid/solid coupling represented by this approach has been so-called **Conjugate heat transfer** (*CHT*). If the heat source directly is applied to the internal fluid interface, only the internal fluid is solved. This simplified approach is here referred to as an **Ideal locally imposed** condition.

The space-time thermal distribution strongly depends on the thermal boundary condition, the friction Reynolds number (Re_τ) and the Prandtl number (Pr), while the streamwise length of the computational domain (L_x/D or L_x/H) and the simulation time are decisive for the statistics convergence.

A process dominated by *isoflux of heat* at the wall can be modeled by imposing a **non-fluctuating and linearly increasing wall temperature** (Dirichlet-type boundary condition, *DBC*) or by prescribing a **non-fluctuating and uniform heat flux** (Neumann boundary condition, *NBC*). The *DBC* and the *NBC* correspond to the physical configuration in which thermal activity ratio $K \longrightarrow 0$ and $K \longrightarrow \infty$, respectively. For instance, the **temperature fluctuations** increase nearby the wall with increasing thermal activity ratio, they are shifted away from the pipe center with increasing Re_τ. **The mean temperature and temperature fluctuations** increase with increasing values of Pr. For $Pr > 1$, temperature fluctuations at the wall do not affect heat transfer and the **average velocity and temperature profiles are similar**. It was found that the convergence of the first and second order thermal statistics is achieved for a minimum pipe length of $L_x = 2\pi D$. The mesh resolution effect, on the first and second order thermal statistics, is practically negligible if it is compared with the Re_τ, Pr and L_x effects.

Finally, some deviations could appear at the pipe center when a cylindrical mesh is used. This depends on the strategy to overcome the **singularity at the pipe center**. Such a issue, in codes based on a Cartesian mesh, as *Incompact3d*, this singularity is naturally bypassed.

Chapter 3

Immersed boundary methods

Considering a numerical approach to the fluid-solid interaction problem, the geometrical solid representation can be classified into two categories: body-conformal and non-body conformal methods (Figures 3.1a and 3.1b). In the first category, the mesh follows the solid geometry and thereby the computational boundaries of the mesh coincide with the solid boundaries. Thus, Dirichlet or even Neumann boundary conditions on the solid surface can be prescribed directly. However, the generation of an appropriated body-conformal mesh could be more complex than solve the fluid dynamic equations (Fortuna, 2012[19]). In order to represent adequately the solid, this technique has to balance the total number of mesh points and the refinement near the solid wall (Mittal & Iaccarino, 2005[61]). This balance can yield accuracy and convergence problems due to an inappropriate mesh (Ferziger & Perić, 2002[15]). Apart from the complexity and limited flexibility of functions used to generate the mesh, the body-conformal methods commonly reduce the stencil of the numerical scheme at the fluid-solid interface leading to a low order of precision in the computation of the discrete operators (Gautier, 2013[20]).

Immersed boundary methods (*IBM*) surge as a non-body conformal alternative to represent solids submerged. The problem can be formulated and solved in a simple Cartesian stationary mesh, even for complex solid geometries in movement. These methods were introduced for the first time by Peskin (1972)[77] to simulate blood flow inside heart valves. Since then, the *IBM* has been extensively applied to a wide range of problems: compressible flows ([24, 60, 59]), particulate flows ([101, 110]), micro-scale flows ([2]), interaction with solid bodies ([26, 114], among others), multi-phase flows ([23]), conjugate heat transfer ([30, 110]), environmental

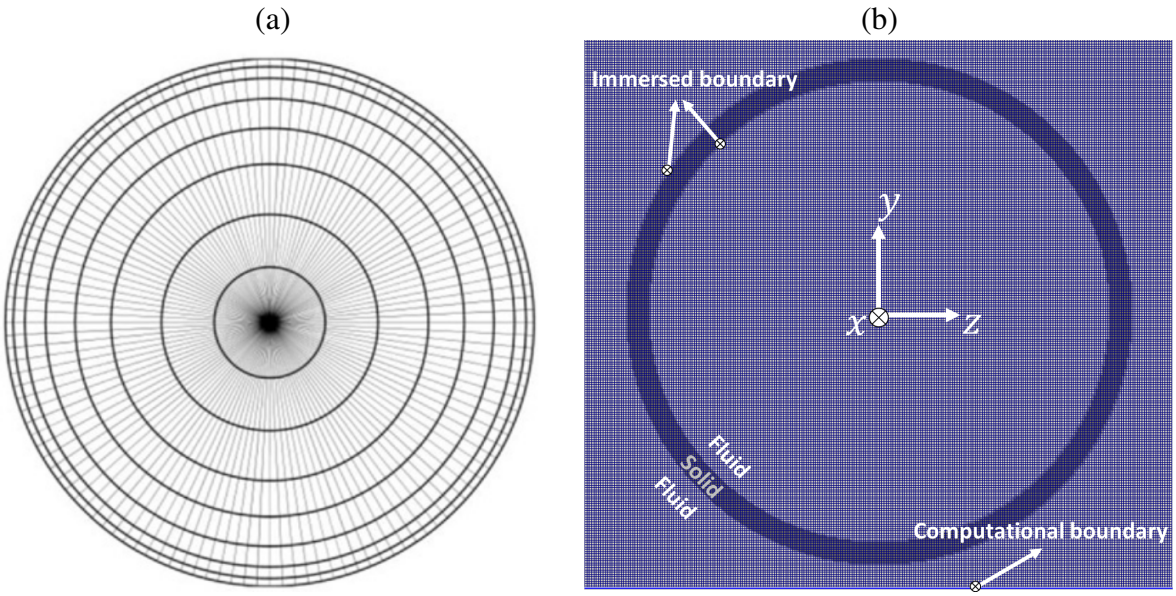

Figura 3.1: Structured pipe meshes: (a) body-conformal radial mesh ([88]), (b) non-body conformal Cartesian mesh.

flows ([94]), bio-fluids ([14]), etc.

Numerical simulation with *IBM* allows using a mesh of simple topology as a Cartesian structured mesh (with or without local refinement), which is desirable in terms of efficiency and parallelization implementation ([59]). Basically, the non-body conformal methods consider the solid as embedded in the mesh, and therefore the mesh does not depend on the body shape. *IBM* allows making computations for moving boundaries simple and accurate, since the mesh does not need to reformulate for every body displacement. Moreover, high order numerical schemes can be straightforward implemented ([57, 68]). On the other hand, Dirichlet- and, especially, Neumann-type boundary conditions could represent an implementation challenge essentially related to the geometric complexity. More details about the basis of *IBM* can be found in the reviews of Iaccarino & Verzicco (2003)[31], Mittal & Iaccarino(2005)[61] and Kim & Choi (2019)[45]. In the following, the main *IBM* approaches and highlights are presented. This includes the approaches for solving the mass, momentum and energy conservation equations in a flow with a fluid-solid interface.

3.1 Mass and momentum conservation equations

The motion of an incompressible and Newtonian fluid is governed by the mass and momentum conservation equations, respectively, expressed as

$$\vec{\nabla} \cdot \vec{V} = 0, \tag{3.1}$$

$$\frac{\partial \vec{V}}{\partial t} + \vec{V} \cdot \vec{\nabla}\vec{V} = -\frac{1}{\rho}\vec{\nabla}p + \nu\nabla^2\vec{V}, \tag{3.2}$$

where $\vec{V}$ is the fluid velocity field, p the pressure field, ρ and $\nu = \mu/\rho$ are the density and cinematic viscosity of the fluid, respectively. On the interface between fluid and the solid domain ($|_{int}$), equations 3.1 and 3.2 must respect the no-slip condition (kinematics condition)

$$\vec{V}\Big|_{int} = \vec{V}_s\Big|_{int}, \tag{3.3}$$

where $\vec{V}_s\Big|_{int}$ is the solid velocity at the interface.

If finite differences approach were adopted to solve the fluid motion equations, by using a body-conformal method, the governing equations have to be solved in a transformed structured grid, which follows the body shape. Whereas finite volume and finite element methods can be employed in an unstructured grid fitted to the body, incorporating the body geometrical information directly and locally in the discrete governing equations. This means that the discrete differential operators have to be modified on the solid boundary.

The main advantage of *IBM* is that the mesh is independent of the body shape. Thus a Cartesian mesh can be employed without coordinate transformation or complex modifications on the discrete operators on the fluid-solid interface. Conversely, the boundary condition at the interface is incorporated by modifying the governing equations near the solid surface. This leads to the classification into two *IBM* approaches: **continuous forcing approach** and **discrete forcing approach**. In the first approach, the body representation is carried out by adding a momentum forcing term in the continuous equations to ensure the no-slip condition on the interface. The second approach ensures this condition in the discrete equations form at the

computational mesh nodes near the immersed boundary (*IB*). In the following sections, these approaches are briefly discussed.

3.1.1 Continuous forcing approach

Several continuous forcing methods were developed since Peskin introduced the *IBM*. This section concerns with methodologies associated with elastic and rigid stationary/moving boundaries. This approach consists in adding a forcing term $\vec{f_{IB}}$ to the momentum equation (3.2), in order to balance the fluid-solid forces and ensure the no-slip condition (Equation 3.3) on the interface. Then, the modified equations of motion are

$$\frac{\partial \vec{V}}{\partial t} + \aleph\left[\vec{V}\right] + \frac{1}{\rho}\vec{\nabla}p = \vec{f_{IB}}, \tag{3.4}$$

$$\vec{\nabla} \cdot \vec{V} = 0, \tag{3.5}$$

where $\aleph\left[\vec{V}\right] = \vec{V} \cdot \vec{\nabla}\vec{V} - \nu\nabla^2\vec{V}$ is the convective-diffusive term and $\vec{f_{IB}}$ is the forcing term which ensures the no-slip condition

$$\vec{V}\Big|_{int} = \vec{V_s}\Big|_{int}. \tag{3.6}$$

Elastic boundaries

The methodology introduced by Peskin is an *Eulerian-Lagrangian* methodology, which solves the governing equations in a Cartesian stationary mesh by finite differences. The methodology was developed to represent the coupled blood-membrane motion inside heart valves. The immersed boundary is defined by elastic fibers whose motion is represented by tracking massless Lagrangian points. The curve, that describes the body contour $\vec{X_k}(t)$, preserves the no-slip condition of the k^{th} Lagrangian point by

$$\frac{\partial \vec{X_k}}{\partial t}(t) = \vec{V}(\vec{X_k}, t). \tag{3.7}$$

Note that this discrete form in a Lagrangian fashion is identical to the kinematic condition defined in Equation 3.3. The forcing term $\vec{f_{IB}}(\vec{x},\ t)$, sometimes referred as force density, at the

Eulerian mesh point $\vec{x}_{i,j}$ located at a distance $|\vec{x}_{i,j} - \vec{X}_k|$ from the k^{th} Lagrangian point, is given by

$$\vec{f}_{IB}(\vec{x}_{i,j},\ t) = \sum_k \vec{F}_k(t)\ \delta(|\vec{x}_{i,j} - \vec{X}_k(t)|), \tag{3.8}$$

where $\vec{F}_k(t)$ is the stress at the point k, and δ can be the sharp Dirac delta function or an improved smooth function of the force distribution (Figure 3.2). $\vec{F}_k$ is related to the fiber deformation by the constitutive laws as the Hooke's law, an elastic energy function or the principle of virtual work. The dynamic evolution of the fibers (Equation 3.7) is now performed through the δ-function as

$$\frac{\partial \vec{X}_k}{\partial t}(t) = \sum_i \sum_j \vec{V}(\vec{x}_{i,j}, t)\ \delta(|\vec{x}_{i,j} - \vec{X}_k(t)|). \tag{3.9}$$

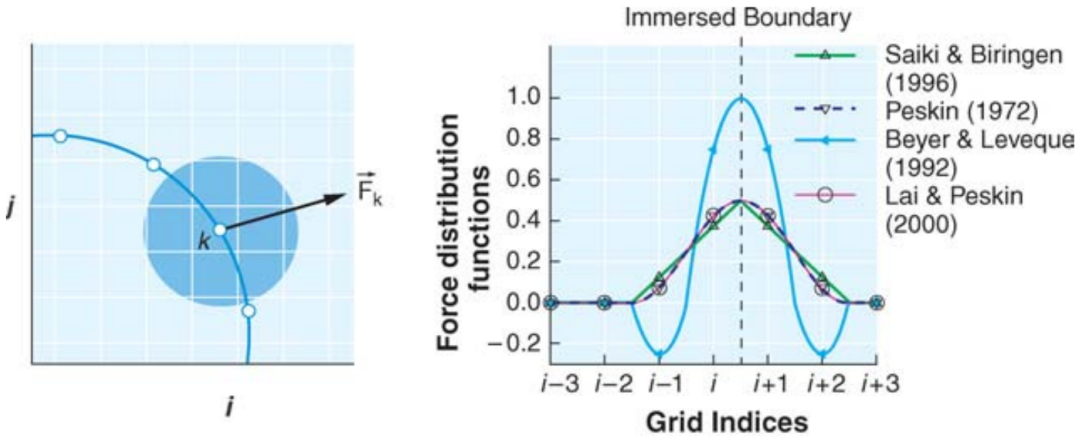

Figura 3.2: Left: Transfer of forcing $\vec{F}_k$ from Lagrangian boundary point ($\vec{X}_k$) to surrounding fluid nodes; shaded region signifies the extent of the force distribution. Right: Distribution functions employed in various studies. Figure adapted from Mittal & Iaccarino, 2005[61].

This formulation finds its applications in biofluid problems concerning with elastic structures in which the external flow is not very important and it is commonly treated as periodic. Rigid boundaries can be represented by extremely increasing the stiffness of the elastic fibers.

Stationary and moving rigid boundaries

Goldstein *et al.* (1993)[28] developed the *virtual boundary method* to simulate flow around rigid bodies. The body can be seen as a damped oscillator (Iccarino & Verzicco, 2003[31])

attached to an equilibrium location $\vec{X}_k^e$. This model considers that the momentum forcing term induced by the k^{th} Lagrangian point at any grid point $\vec{x}_{i,j}$ has the following feedback relation with the surrounding velocities

$$\vec{f}_{IB}(\vec{x}_{i,j},\ t) = \sum_k \vec{F}_k(t)\ \delta(|\vec{x}_{i,j} - \vec{X}_k^e|), \tag{3.10}$$

with

$$\vec{F}_k(t) = \alpha_{IBM} \int_0^t \vec{V}_k(\tau)d\tau + \ \beta_{IBM}\ \vec{V}_k(t), \tag{3.11}$$

where α_{IBM} and β_{IBM} are coefficients conveniently selected to best ensure the no-slip condition

$$\vec{0} = \vec{V}(\vec{X}_k^e,\ t) \equiv \sum_i \sum_j \vec{V}(\vec{x}_{i,j},\ t)\ \delta(|\vec{x}_{i,j} - \vec{X}_k^e|). \tag{3.12}$$

Angot *et al.* (1999)[1] and Khandra *et al.* (2000)[41] developed a *penalty method*, which considers the domain as a porous medium where fluid (solid) has an hypothetical very high (small) porosity ϕ, and thereby the governing equations are the Navier-Stokes/Brinkman equations (Brinkman, 1947[7]). This approach added is a particular case of the *virtual boundary method*, in which $\alpha_{IBM} \equiv 0$ and $\beta_{IBM} \equiv \mu/\phi$.

The feedback forcing near the boundary causes spurious oscillations, while the stability of the method is restricted by the set of parameters ($\alpha_{IBM},\ \beta_{IBM}$), especially for highly unsteady flows (high Reynolds numbers). Hence, Saiki *te al.* (1996)[90] extended the virtual boundary method for controlling such spurious oscillations by specifying a velocity suppressor at the boundary and using fourth order centered schemes. On the other hand, Lai & Peskin (2000)[46] proposed to control the boundary motion by a very stiff spring (whose stiffness constant is $K \gg 1$) which transfer a restoring force to remain the *IB* location $\vec{X}_k(t)$ close to the equilibrium location $\vec{X}_k^e(t)$. Thus, the restoring force is expressed by

$$\vec{F}_k(t) = K\left(\vec{X}_k^e(t) - \vec{X}_k\right). \tag{3.13}$$

Therefore, the forcing term in the momentum equation is

$$\vec{f}_{IB}(\vec{x}_{i,j},\ t) = \sum_{k} \vec{F}_k(t)\ \delta(|\vec{x}_{i,j} - \vec{X}_k|). \tag{3.14}$$

This is another special version of the virtual boundary method when $\beta \equiv 0$. Note that moving boundaries ($\partial\vec{X}/\partial t \neq \vec{0}$) can be simulated by this methodology, and the boundary position is updated by integrating

$$\frac{\partial \vec{X}_k}{\partial t} = \vec{V}(\vec{X}_k,\ t) \equiv \sum_{i} \sum_{j} \vec{V}(\vec{x}_{i,j},\ t)\ \delta(|\vec{x}_{i,j} - \vec{X}_k|). \tag{3.15}$$

General considerations

The continuous forcing approach was developed for elastic boundaries founding applications in biological flows and multiphase flows. However, for rigid boundaries, it requires employing some simplified models to mimic the solid behavior, and the parameters used for these models restrict the accuracy and stability of the method (Mittal & Iaccarino, 2005[61]). The smooth δ-function, to represent a real sharp boundary transition, is particularly undesirable for thin boundary layers associated with high Reynolds numbers (Mittal & Iaccarino, 2005[61]). Furthermore, an adequate representation of thin boundary layers requires increasing the number of mesh nodes, even inside the solid domain, where solving the governing equations is generally unnecessary and increases the computational processing requirement.

3.1.2 Discrete forcing approach

As the Navier-Stokes equations do not allow extracting an analytical forcing term to enforce the no-slip condition at the fluid-solid interface, the precedent approaches use a simplified model to estimate $\vec{f}_{IB}$ in the momentum equation continuous formulations. Conversely, Mohd-Yosuf (1997)[62] and Verzicco *et al.* (2000)[103] propose to extract the forcing term directly from the discrete form of the governing equations. Basically, in this approach, $\vec{f}_{IB}$ acts as a velocity corrector that ensures $\vec{V} = \vec{V}_s$ at the interface.

As this method is based on the discrete formulation, the time advancement from t^n to t^{n+1}, by the pressure projection method (typical fractional steps), reads

$$\frac{\vec{V}^* - \vec{V}^n}{\Delta t} + \aleph' \left[\vec{V}\right] + \frac{1}{\rho}\vec{\nabla} p^n = \vec{f}_{IB}^{n+1}, \tag{3.16}$$

$$\frac{\vec{V}^{**} - \vec{V}^*}{\Delta t} - \frac{1}{\rho}\vec{\nabla} p^n = 0, \tag{3.17}$$

$$\frac{\vec{\nabla} \cdot \vec{V}^{**}}{\Delta t} = -\frac{1}{\rho}\vec{\nabla}^2 p^{n+1}, \tag{3.18}$$

$$\frac{\vec{V}^{n+1} - \vec{V}^*}{\Delta t} = \frac{1}{\rho}\vec{\nabla} p^{n+1}, \tag{3.19}$$

where $\aleph' \left[\vec{V}\right]$ is the discrete operator, of the convective-diffusive term, associated to the derivative schemes. The time level at which this operator is applied depends on the time advancement scheme. As it must be verified the no-slip condition (3.6) $\vec{V}^{n+1} = \vec{V}_s^{n+1}$, then

$$\vec{f}_{IB}^{n+1} = \begin{cases} \dfrac{\vec{V}_s^{n+1} - \vec{V}^n}{\Delta t} + \aleph' \left[\vec{V}\right] + \frac{1}{\rho}\vec{\nabla} p^n & \text{near the interface;} \\ 0 & \text{elsewhere.} \end{cases} \tag{3.20}$$

In practice, this approach is straightforward when the interface coincides with the mesh nodes. Otherwise, an interpolation procedure is commonly required. Assuming that all flow variables at t^n are known and satisfy the boundary conditions on the computational domain and on the immersed boundary, as it is described by Balaras (2004)[3], the basics steps of the discrete forcing algorithm are summarized as:

1. First, predict an intermediate velocity field $\vec{V}^*$ by the discrete Equation 3.16, omitting the forcing term $\vec{f}_{IB}^{n+1}$. The resulting $\vec{V}^*$ is not necessary divergence free, besides it will not satisfy the boundary condition on the interface yet.

2. Then, compute $\vec{f}_{IB}^{n+1}$ from Equation 3.20. The value of the velocity $\vec{V}_s$ at the forcing points is estimated using an interpolation procedure. These forcing points can be placed outside or/and inside the body, as it is used in a ghost cell method (Tseng & Ferziger (2003)[99]).

3. Recompute $\vec{V}^*$ from the Equation 3.16 with the forcing term $\vec{f}_{IB}^{n+1}$. The resulting velo-

city will satisfy the desired boundary condition on the immersed boundary but not the incompressibility condition (3.5).

4. Compute $\vec{V}^{**}$ from the Equation 3.17. This step eliminates the influence of the precedent pressure field.

5. Update the pressure by solving the Poisson equation (p^{n+1} in Equation 3.18).

6. Update the velocity ($\vec{V}^{n+1}$ in Equation 3.19).

7. Go to step 1, to calculate the next time step, until ending.

Discrete forcing approach can be classified in *indirect forcing* ([103], [3]) and *direct forcing* ([62], [13]). The indirect forcing represents the immersed boundary condition by spreading the forcing term into the surrounding flow region through the δ-function. For high Re, this is particularly undesirable, and thus, to overcome this issue, the direct forcing modifies the computational stencil near the immersed boundary to directly impose the boundary condition. Therefore, the main difference between these discrete forcing approaches is the procedure used to ensure the no-slip condition at the forcing points (step 2 of the algorithm).

Direct forcing approach

In order to ensure the boundary condition, the spectral method of Mohd-Yosuf (1997)[62] mirrors the fluid velocity field across the fluid/solid interface (towards the solid region). It means that the velocity is imposed inside the solid domain (*internal forcing*). On the other hand, Fadlun *et al.* (2000)[13] proposed to impose the velocity at the first fluid node (*external forcing*). This could be done by linear interpolation using information of the velocity at the interface and at the second external mesh node (which is obtained by directly solving the Navier-Stokes equations). This conceptually corresponds to applying the momentum **forcing inside the fluid**.

In the Mohd-Yosuf's method, only the tangential (to the interface) component of the velocity is used to prescribe the boundary condition. To deal with this issue, Zhang & Zheng (2007)[112] implemented a bilinear interpolation/extrapolation which considers either the tangential or the normal velocity components to reconstruct the velocity at the internal nodes. The

forcing inside the solid can be done basically into two ways: by forcing all the inside nodes and leaving free the pressure computation, or forcing the first internal node and leaving free the velocity and pressure at the other internal nodes. Inspired in the first procedure, for circular cylindrical geometries, Parnaudeau *et al.* (2004)[73] uses the forcing concept in all the inside nodes by mirroring the external flow (bilinear interpolation) and modulating the flow by a sinusoidal function. This methodology deals with the singularity in the cylinder center and gives continuity to the velocity profile, which is mandatory when, for instance, compact schemes in finite differences are applied (see Section 5.3.1 for more details).

In order to achieve higher order representation at the interface, Tseng & Ferziger (2003)[99] extended the idea of Faldun *et al.* (2000)[13] resulting in the so-called Ghost-cell finite-difference approach. A ghost cell is defined as the cell in the solid that is adjacent to at least one fluid cell. For each ghost cell, an interpolation scheme has to be applied to implicitly incorporates the boundary condition. As this interpolation do not consider the mass conservation law, the reconstruction is not divergence free. This issue can be bypassed by the cut-cell finite-volume approach proposed by Ye *et al.* (1999)[108], in which the discretization fulfills the conservation laws due to the nature of the finite-volume approach.

3.1.3 Concluding remarks

The direct forcing approach improves the boundary layer representation for high Reynolds numbers, since it makes a sharp representation of the immersed boundary, whereas the continuous forcing or the indirect forcing approaches spread the forcing through the surrounding flow nodes. Furthermore, the stability constraints, associated with the user-specified set of parameters used in the feedback continuous forcing (Goldstein *et al.* (1993)[28]), are overcome. Some drawbacks of the direct forcing method could be: (i) their accuracy, stability and discrete conservation properties are strongly dependent on the discretization method, (ii) thus, these methods are not always straightforward for implementing, and (iii) the inclusion of moving boundaries can be more complex than in continuous forcing. The drawback (iii) is due to the fluid nodes which were inside the solid at the previous time step do not have flow information ("freshly-cleared" cells in Figure 3.3). Figure 3.4 shows an interaction scheme of the Euler

grids and the Lagrange nodes at the immersed boundary.

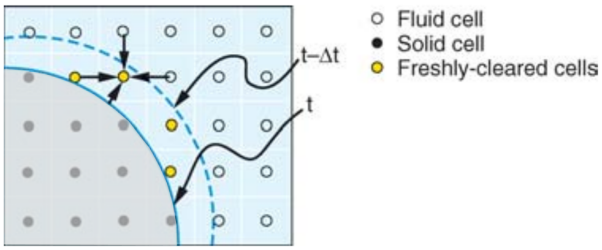

Figura 3.3: Schematic of "freshly-cleared" cells on a fixed Cartesian grid due to boundary motion from time step $(t - \Delta t)$ to t. Schematic indicates how the flow variables at one such cell could be obtained by interpolating from neighboring nodes and from the immersed boundary. Figure adapted from Mittal & Iaccarino, 2005[61].

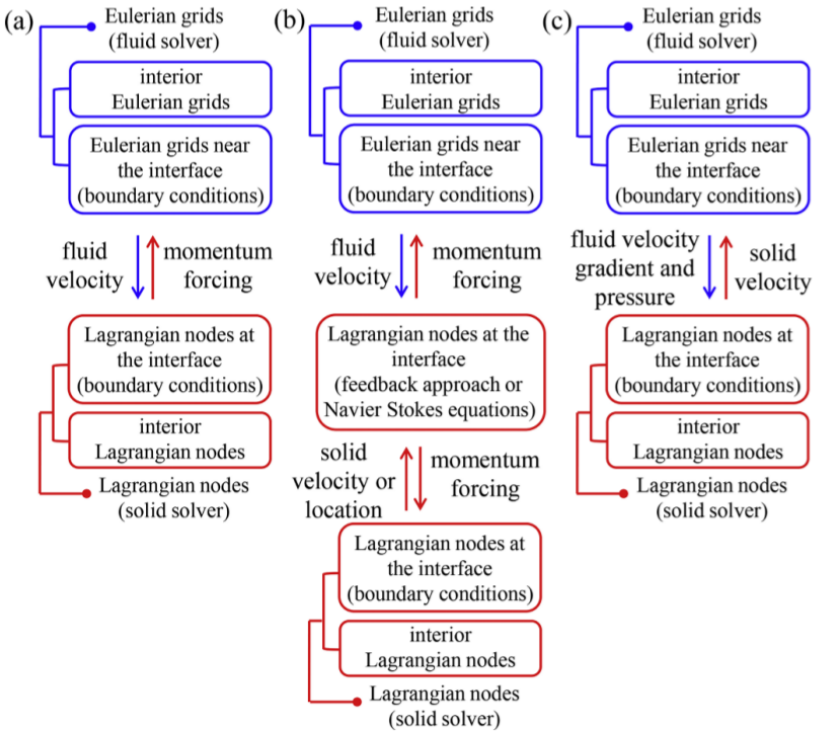

Figura 3.4: Transfer of variables to satisfy the boundary conditions (no-slip condition and Cauchy stress theorem) for *IBM* methods: (a) direct momentum forcing for original *IBM* (Peskin, 1972[77]); (b) direct momentum forcing with a feedback approach (Goldstein, 1993[28]; Kim & Peskin, 2006[42]) and with Navier-Stokes equations (Ulhmann, 2005[101]); (c) velocity reconstruction (Mohd-Yusof, 1997[62]; Borazjani et al., 2008[5]; Luo et al., 2010[58]). Figure adopted from Kim & Choi (2019)[45].

The methods described above use commonly bilinear (trilinear in 3D) interpolation to represent the boundary condition. This is a disadvantage for a parallelization strategy by 2D domain decomposition since flow information can only be acquired in one direction. Therefore, Gautier (2013)[20] developed an alternative direct forcing method (so-called *Reconstruction Method by*

Alternated Direction), which can deal with complex geometries and this parallelization strategy (see Section 5.3).

The *IBM* has extensively applied to the momentum equation and can be completely extended to solve scalar fields, as well. Some problems require to implement the conservation of energy equation, and thereby the next section discusses some *IBM* strategies to deal with a scalar field.

3.2 Energy conservation equation (Fluid-solid heat transfer)

A fluid in movement can be an efficient way to transport heat from one source to another. This advantage has motivated several Direct Numerical Simulations (*DNS*) in turbulent heated flow, which consider the thermal energy (temperature) as a passive scalar transported inside the fluid by conduction and manly by convection (*e. g.* [43, 36, 39, 97, 98, 82, 17, 18]).

In diabatic wall-bounded flows with thermal gradients, thermal interaction occurs between fluid and solid. This interaction, frequently so-called *Conjugate heat transfer* (*CHT*), represents the fluid-solid thermal coupled problem of turbulent heat transfer and unsteady heat conduction in the solid wall. Recalling Section 2.4.1, the governing equations for the *CHT* are

$$\begin{aligned}
&\text{in the fluid:} && \tfrac{\partial T}{\partial t} = -\vec{V}\cdot\vec{\nabla}T + \alpha\nabla^2 T,\\
&\text{in the solid:} && \tfrac{\partial T_s}{\partial t} = \alpha_s\nabla^2 T_s,\\
&\text{at the interface:} && T|_{int} = T_s|_{int},\\
&\text{at the interface:} && \lambda_s \left.\tfrac{\partial T_s}{\partial \vec{n}}\right|_{int} = \lambda \left.\tfrac{\partial T}{\partial \vec{n}}\right|_{int}.
\end{aligned}$$

Former papers have studied the *CHT* problem analytically and experimentally (*e. g.* [83, 40, 93, 37, 95]). However, the relevant simplifications of the analytical approaches and the difficulty to measure experimentally turbulent quantities, in very thin boundary layers, makes numerical simulation a powerful and useful tool to study instantaneous turbulent structures in heated flows ([38, 89]).

One of the main challenges in numerically solving *CHT* problems is to couple, at the fluid-solid interface, the convective-diffusive equation (in the fluid) with the conduction equation (in the solid). To overcome this challenge, two techniques arise:

- *solving separately the fluid and solid* energy equations and matching the boundary conditions by iterative processes ([105]) or by tolerating a small temperature discontinuity at the interface ([109, 97, 17, 18]);

- solving the energy equations in a *unique computational domain* by changing the diffusion coefficients (viscosity or thermal conductivity) inside each domain or by imposing a volumetric source/sink term at the fluid-solid immersed interface ([44]), in order to ensure the thermal boundary conditions. Evidently, the *unique domain* approach is appropriate for applying an *IBM*.

Some of these methods deal with the sudden change of the diffusion coefficients in heat transfer problems, by imposing an artificial very high viscosity inside the solid domain, to represent the no-slip condition (as the penalty method, [1]), and the harmonic mean formulation or the concept of effective conductivity to impose the heat flux condition. Other *IBM* approaches impose a momentum forcing term and a source/sink term at the fluid-solid interface, by reconstruction (interpolation) techniques, to respectively enforce the no-slip condition and the thermal boundary conditions in the discrete equations (*e. g.* [44, 71, 30, 111, 106, 34, 85, 86, 59]).

In order to approximate the real *CHT* thermal condition, it is common to only apply simplified thermal conditions, at the fluid-solid interface, as the ideal locally imposed non-uniform (*IT*) or uniform temperature (*IUT*), or locally imposed heat flux (*IF*). Most of the heat transfer studies with *IBM* only consider Dirichlet-type boundary conditions (as *IT* or *IUT*), because the Neumann-type boundary condition (*IF*), on immersed boundaries, represents a bigger challenge ([86]). Moreover, it should be remembered that, these ideal conditions are not satisfactory when the thermal diffusivities of the solid and fluid are of the same order [17].

3.2.1 Source/sink energy term

Just as the momentum and mass equations respectively require forcing and mass-source terms for imposing the boundary conditions at the interface, the energy equation can incorporate source/sink term at the interface to represent a fluid-solid heat transfer scenario. Kim *et al.* (2004)[44] introduced for the first time the source/sink term in the energy conservation equation

in the fluid to account the effect of the hot/cool solid wall. Using information from the nearby fluid points and applying linear or bilinear interpolation, this term is applied by forcing the interpolated value at the nearest solid point to the interface. This methodology uses a finite volumes formulation on a mesh staggered together with a fractional step method, to deal with Dirichlet-type boundary conditions (*DBC*) and Neumann-type boundary conditions (*NBC*). The discrete energy equation at the interface, incorporating the source term, reads

$$\frac{T|_{source}^{n+1} - T^n}{\Delta t} = \aleph' [T] + f_{source}^{n+1}, \qquad \text{at the source/sink points,} \tag{3.21}$$

where $T|_{source}$ is the uncorrected temperature at the cells nearby the interface where the source term is applied, $\aleph' [T]$ is the discrete version of the convective-diffusive operator $\aleph [T] = -\vec{V} \cdot \nabla T + \alpha \nabla^2 T$ applied over the temperature. To induce the reconstructed target temperature $T|_{int}$ which ensures the boundary condition, instead of the uncorrected one $T|_{source}^{n+1}$, the source/sink term should be

$$f_{source}^{n+1} = -\aleph' [T] + \frac{T|_{int}^{n+1} - T^n}{\Delta t}, \qquad \text{at the source/sink points.} \tag{3.22}$$

The variations of this method essentially differ in the selections of the source/sink points and the reconstruction technique.

3.2.2 Effective thermal conductivity

An *IBM* applied to finite volume or finite elements schemes, the temperature imposition (*DBC*) could not be complicated, however, the heat flux condition (*NBC*) is more demanding. Hence, the penalty method *IBM* is based on suddenly change the properties of the medium across the fluid/solid interface. In the penalty method framework, to impose *NBC*, it can be introduced the concept of *effective thermal conductivity* at the interface ([64]). This method states that effective conduction in the cell at the interface can be expressed as a linear combination of the conductions inside each medium. For instance,

$$\frac{1}{2}\left(\lambda_s \left.\frac{\partial T_s}{\partial \vec{n}}\right|_{int} + \lambda \left.\frac{\partial T}{\partial \vec{n}}\right|_{int}\right) = \lambda_e \left.\frac{\partial T_s}{\partial \vec{n}}\right|_{int} \qquad \text{at the interface cells,} \tag{3.23}$$

where λ is the effective thermal conductivity. Approximating the precedent derivatives numerically and considering the temperature continuity, for cells faces coinciding with the interface, it can be obtained that the effective thermal conductivity is

$$\lambda_e = \frac{G_2 \Delta x}{G_2 \Delta x_f + \Delta x_s}, \tag{3.24}$$

where $G_2 = \lambda_s/\lambda$ is the thermal conductivities ratio, Δx is the mesh spacing, $\Delta x_s(\Delta x_f)$ is the distance from the solid(fluid) temperature point to the interface location. On the other hand, if the interface cuts the cells, λ can be computed as an average value along the interface surface cut by the cells (S_{int})

$$\lambda_e = \frac{1}{S_{int}} \int_{S_{int}} \lambda(S) dS'. \tag{3.25}$$

3.2.3 Concluding remarks

In diabatic wall-bounded flows, thermal interaction occurs between the fluid and solid (frequently so-called *Conjugate heat transfer*, *CHT*). Mathematically, this interaction represents the problem of the fluid-solid thermal interaction of turbulent heat transfer and unsteady heat conduction in the solid. Typically some simplified thermal conditions, at the fluid-solid interface, are considered: ideal locally imposed non-uniform (*IT*) or uniform temperature (*IUT*), or locally imposed heat flux (*IF*). One of the main challenges in solving numerically *CHT* problems is coupling the convective-diffusive equation (in the fluid) with the conduction equation (in the solid), at the fluid-solid interface.

Some techniques arise to solve this interaction problem, specifically to set the thermal boundary conditions. The *IBM* appears as an accurate tool, which allows using a simple structured mesh and eventually complex geometries. Among the *IBM* possibilities, two approaches can be highlighted: (*i*) applying a source/sink term in the energy equation (equivalent to the forcing

term in the momentum equation), or (*ii*) use a sudden or transitional change of the diffusive coefficients across the fluid-solid interface. The fundamental proposal of the approach (*i*) is to impose a momentum forcing term and a source/sink term at the fluid-solid interface, by reconstruction (interpolation) techniques, to respectively enforce the no-slip condition and to set the thermal boundary condition (*e. g.* [44, 71, 30, 111, 106, 34, 85, 86, 59]).

Recently, Song *et al.* (2017)[96] proposed an *IBM* which applies the effective thermal conductivity concept and a modification of the convection terms. However, the code is only poorly evaluated for laminar cases. Luo *et al.* (2017)[59] proposed a 2D *ghost-cell IBM* in explicit finite differences to simulate compressible flows under temperature boundary conditions of Dirichlet, Neumann, and Robin type, but without *CHT*. This methodology is applied to external flow around a cylinder at low Reynolds numbers (2D flow). Iaccarino & Moreau, 2006[30] studied the *CHT* in complex geometries on Cartesian mesh by applying a solver based on Reynolds Averaged Navier-Stokes equations model (*RANS*) with immersed boundary so-called *IBRANS*. Despite these efforts, to the best of our knowledge there are no *LES/DNS* studies considering *CHT* fluid-solid interaction by mean *IBM* techniques.

Chapter 4

Governing equations

In this chapter, the governing equations associated to fluid-solid thermal interaction are presented. The details concerning mathematical modeling of fluid dynamics of incompressible flows, temperature passive transport in turbulent flows, and temperature conduction in the solid are discussed. In order to solve the equations, the boundary and initial conditions are defined, for pipe and channel periodic flow. To deal with the *fluid-solid thermal coupling*, the conjugate heat transfer equations are presented.

4.1 Fluid dynamics model

All the flow governing equations are presented in the dimensionless form. The reference velocity is the bulk velocity (U_b) and the reference length is the pipe diameter (D) or the channel height (H). The incompressible flow dynamic of a Newtonian fluid can be mathematically represented by equations of mass and momentum balance. In rectangular Cartesian coordinates, these equations, respectively, read

$$\vec{\nabla} \cdot \vec{u} = 0, \tag{4.1}$$

$$\frac{\partial \vec{u}}{\partial t} = \aleph\left[\vec{u}\right] - \vec{\nabla}\Pi + \vec{f_\tau}, \tag{4.2}$$

and on fluid-solid interface, these equations must respect the no-slip condition (kinematics con-

dition)

$$\vec{u}\Big|_{int} = \vec{u}_s\Big|_{int}, \tag{4.3}$$

where $\vec{u}_s$ is the solid velocity, $\vec{u}$ is the fluid velocity field, Π the fluid pressure field, Re the global Reynolds number and $\aleph\left[\vec{u}\right] = -\left(\vec{u}\cdot\vec{\nabla}\right)\vec{u} + \frac{1}{Re}\nabla^2\vec{u}$. The momentum forcing therm $\vec{f_\tau} = [f_\tau\ 0\ 0]^T$, constant in the space, acts in internal periodic flow to compensate the net viscous friction at the wall and thereby it sustain stationary regime ($U_b = 1$, constant volumetric flux). Physically, this term could represent the gravitational force caused by the duct slope such that it is balanced with the net viscous force. In fully developed turbulent flow, the magnitude of f_τ corresponds to the mean pressure gradient loss $-d\langle\Pi\rangle_{y,z}/dx$, in streamwise direction. This quantity (as defined in Section 2.2) can be expressed by

$$f_\tau(t) = -\frac{d\langle\Pi\rangle_{y,z}}{dx} = \beta\left(\frac{2Re_\tau}{Re}\right)^2, \tag{4.4}$$

where $\beta = D/D_h = 4$ for pipe flow and $\beta = H/D_h = 2$ for channel flow (with $D_h = A/P$).

In this work, *internal flow* corresponds to channel or pipe flow, in which the streamwise direction coincides with the x axis, and the cross-section of the pipe or channel is parallel to the yz plane (Figure 4.1). The channel or pipe is embedded inside of a rectangular parallelepipedic domain (*computational domain*) aligned with a rectangular Cartesian system of reference. Thus, the no-slip condition at the solid wall (Eq. 4.3) is ensured by an immersed boundary method applied in the discrete formulation (Section 5.3.1), while periodic boundary conditions are defined on the computational domain. However, in the case of conjugate heat transfer in the channel, a Dirichlet boundary condition is adopted in y (wall-normal direction). The velocity and pressure field are assumed statistically homogeneous and periodic in the streamwise direction. On the other hand, at Chapters 6 and 7, the validation process is performed in a Poiseuille and turbulent flows, for both pipe and channel flow configurations, including the initial flow conditions, corresponding to each simulation.

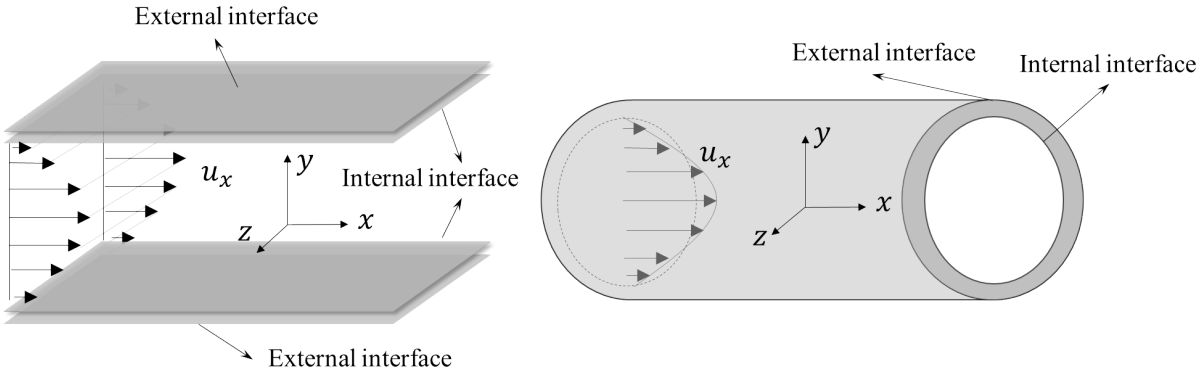

Figura 4.1: Internal flow configurations.

4.2 Fluid/solid heat transfer model

The fluid-solid thermal interaction is commonly so-called *Conjugate heat transfer (CHT)*. This interaction can be mathematically modeled by solving the energy equations either in the solid (heat conduction) or the fluid (heat convection-conduction), and coupling them at the fluid/solid interface.

In internal flows, there are thermal boundary conditions at the *internal* ($|_{int}$) and the *outer* ($|_{out}$) fluid/solid interfaces. Just as the momentum and mass equations, the energy equations are also *normalized* with the same geometrical, kinematic and mechanical quantities, but including characteristic thermal quantities, as the interface temperature $T|_{int}$ and the bulk temperature T_b, for the normalization (Appendix A). The dimensionless energy governing equations of a heated/cooled flow, with constant properties, are

$$\frac{\partial \Theta}{\partial t} = -\vec{u} \cdot \vec{\nabla}\Theta + \frac{1}{RePr}\nabla^2\Theta + f_\Theta, \qquad \text{in the fluid,} \tag{4.5}$$

$$\frac{\partial \Theta_s}{\partial t} = \frac{1}{GRePr}\nabla^2\Theta_s, \qquad \text{in the solid,} \tag{4.6}$$

$$\Theta|_{int} = \Theta_s|_{int}\,, \qquad \text{at the interface} \tag{4.7}$$

$$\left.\frac{\partial \Theta_s}{\partial \vec{n}}\right|_{int} = \frac{1}{G_2}\left.\frac{\partial \Theta}{\partial \vec{n}}\right|_{int}, \qquad \text{at the interface} \tag{4.8}$$

$$\left.\frac{\partial \Theta_s}{\partial \vec{n}}\right|_{out} = \frac{1}{G_2}\left.\left\langle\frac{\partial \Theta}{\partial \vec{n}}\right\rangle\right|_{int}, \qquad \text{at the interface} \tag{4.9}$$

where Θ_s is the temperature of the solid, Θ is the temperature of the fluid, $\vec{n}$ is a local unitary vector normal to the interface pointing towards the fluid, $Pr = \nu/\alpha$ is the Prandtl number, $\alpha = \lambda/(\rho c_p)$ is the thermal diffusivity of the fluid, c_p is the fluid heat capacity at constant pressure, $G = \lambda\rho_s c_{ps}/(\lambda_s \rho c_p)$ is the ratio of thermal diffusivities and $G_2 = \lambda_s/\lambda$ is the ratio of thermal conductivities. The quantity f_Θ acts as a source/sink term which maintains the bulk temperature stationary (in time) and uniform (along the duct). The first two equations rise from the energy conservation inside the fluid and the solid (Eq. 4.5 and 4.6), while the last three equations represent the temperature and heat flux (Eq. 4.7, 4.8 and 4.9) continuity on the fluid-solid interfaces.

As the fluid-solid interface is immersed inside the domain, the *interface boundary conditions* are ensured by an *IBM* based on a modified direct forcing approach (Section 5.3.2). Just as for velocity, the temperature is assumed statistically homogeneous and periodic in the streamwise direction. The *domain boundary conditions* are periodic in all direction, excepting for *CHT* (fluid-solid thermal coupling) for which is used a Neumann-type boundary condition to ensure the heat flux external source.

When the entire fluid-solid thermal coupling is not solved, it is commonly only solved the energy equation in the fluid while imposing a temperature or a heat flux on the internal fluid-solid boundary. These options are ideal conditions and respectively correspond to Dirichlet-type and Neumann-type boundary conditions.

4.3 Ideal thermal boundary conditions

The appropriate ideal thermal boundary condition depends on the dominant phenomenon and the relation of the fluid/solid thermal properties. These are some thermal boundary conditions commonly used at the interface, to simulate heated/cooled channel/pipe flow:

(i) **ideal locally imposed heat flux** *(IF)*,

(ii) **ideal locally imposed non-uniform temperature** *(IT)*,

(iii) **ideal locally imposed uniform temperature** *(IUT)*.

In this section the mathematical formulation briefly is presented for these ideal cases. However, at Appendix A, there is a complete description and discussion of the three cases. *IF*: constant and uniform heat flux at the wall; *IT*: linear streamwise variation of the temperature with no temporal fluctuations at the wall; *IUT*: constant and uniform temperature at the wall (Figure 4.2). In ducts under *IF* thermal condition, the mean temperature varies linearly along the conduct, and thus the *IT* condition mimics the *IF* with non-fluctuating temperature. Hence, in absence of time fluctuations (laminar flow), both conditions (*IT* and *IF*) are equivalents. Only the *IF* and *IT* conditions are considered in the simulations of this study. The initial conditions are described for each case at Chapters 6-7.

For imposing certain ideal boundary conditions, some temperature *transformations* are more adequate than others. In the following section, for each ideal boundary condition, the dimensionless temperature forms are presented, including the source term and the Nusselt number estimation. In Section A.4 is presented a relation between the more common and useful dimensionless temperature forms.

4.3.1 Ideal locally imposed heat flux

The ideal locally imposed heat flux assumes that the heat flux along the duct is constant and uniform while the temperature is free ($\Theta|_{int} \equiv free$, $\partial_{\vec{n}}\,\Theta|_{int} \equiv constant$). When heat flux is imposed (*IF* and *CHT*) the dimensionless form adopted is

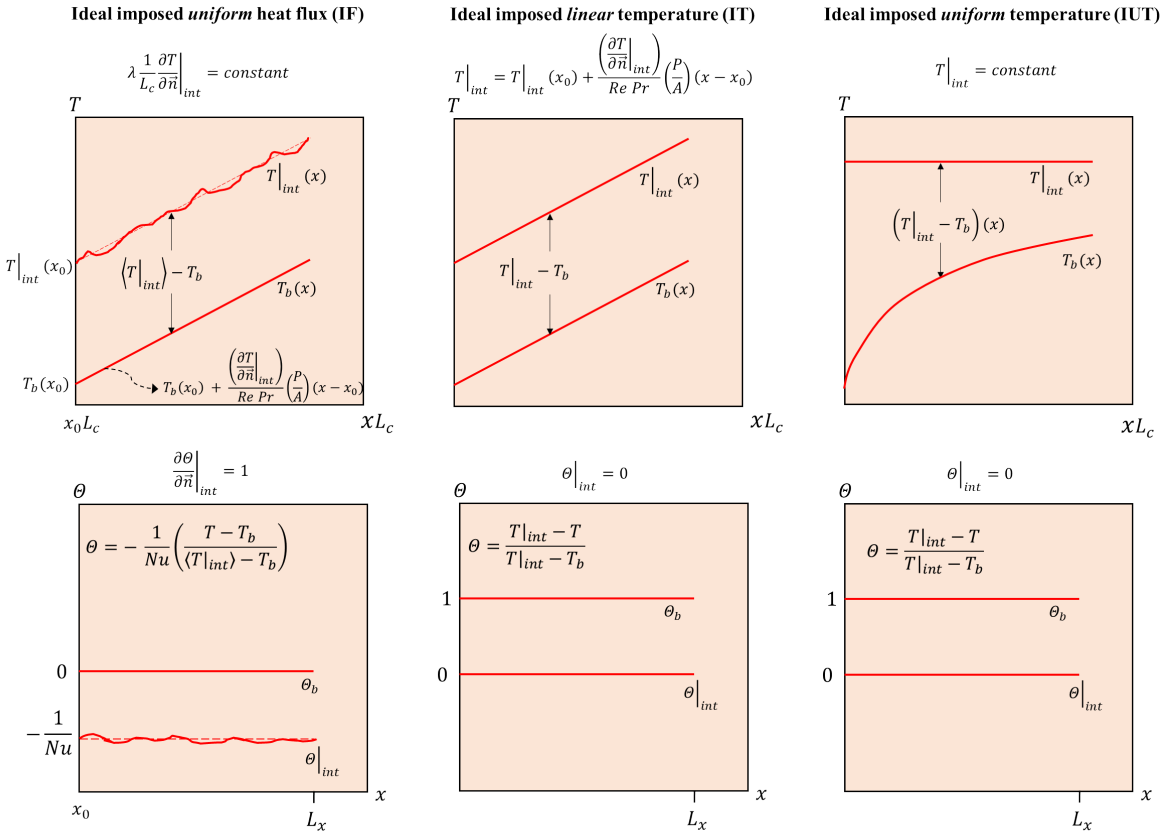

Figura 4.2: Streamwise variation of temperature in thermal fully developed flow, for some ideal thermal boundary conditions. Top: dimensional temperature; bottom: dimensionless temperature. The derivative operator normal to the wall is dimensionless and the normal vector is pointing towards the fluid. The temperature streamwise gradient is inversely proportional to the Reynolds and Prandtl numbers.

$$\Theta = -\frac{1}{Nu}\left(\frac{T - T_b}{\langle T|_{int}\rangle - T_b}\right) \quad \Longrightarrow \quad \left.\frac{\partial \Theta}{\partial \vec{n}}\right|_{int} = 1, \ \ \langle \Theta|_{int}\rangle = -1/Nu, \ \ \Theta_b = 0, \tag{4.10}$$

where $Nu = hL_c/\lambda$ is the average Nusselt number, h is the average convective heat transfer coefficient (from Newton law of cooling, Eq. A.14), L_c is the characteristic length, where $\vec{n} = [n_x\ n_y\ n_z]^T$ is a unitary vector normal to the wall (pointing towards the fluid) and $\langle\cdot\rangle$ is an average operator in spanwise/azimuthal and time. As $\Theta|_{int}$ is free, through its average, the Nusselt number can be estimated as

$$Nu \approx -\frac{1}{\langle \Theta|_{int}\rangle}. \tag{4.11}$$

The temperature transport equation and the interface boundary conditions, for thermal condition of ideal locally imposed heat flux, respectively are

$$\frac{\partial \Theta}{\partial t} = -\vec{u} \cdot \vec{\nabla}\Theta + \frac{1}{RePr}\nabla^2\Theta + u_x \frac{\beta}{RePr}\left(\left.\frac{\partial \Theta}{\partial \vec{n}}\right|_{int}\right), \tag{4.12}$$

$$\left.\frac{\partial \Theta}{\partial \vec{n}}\right|_{int} = 1, \tag{4.13}$$

By the concept of directional derivative, the relation between the normal heat flux $\left(\left.\frac{\partial \Theta}{\partial \vec{n}}\right|_{int}\right)$ and the flux Cartesian components can be expressed as

$$\left.\left(n_x \frac{\partial \Theta}{\partial x} + n_y \frac{\partial \Theta}{\partial y} + n_z \frac{\partial \Theta}{\partial z}\right)\right|_{int} = \left.\frac{\partial \Theta}{\partial \vec{n}}\right|_{int}, \tag{4.14}$$

For channel flow $\vec{n} = [0\ 1\ 0]^T$, Equation 4.14 can be simplified as

$$\left.\frac{\partial \Theta}{\partial \vec{n}}\right|_{int} = \left.\frac{\partial \Theta}{\partial y}\right|_{int}. \tag{4.15}$$

For a pipe with dimensionless diameter $D = 1$ and longitudinal axis collocated with x-axis, the normal vector at the wall location $[x\ y\ z]^T$ is $\vec{n} = \frac{2}{D}[x\ y\ 0]^T$. Then, the heat flux have two cartesian components

$$2\left.\left(x \frac{\partial \Theta}{\partial x} + y \frac{\partial \Theta}{\partial y}\right)\right|_{int} = \left.\frac{\partial \Theta}{\partial \vec{n}}\right|_{int}, \tag{4.16}$$

4.3.2 Ideal locally imposed non-uniform temperature

This ideal boundary condition assumes a fixed dimensional temperature at the wall variating linearly along the duct. After the variable transformation, the dimensionless imposed temperature at the wall is constant and uniform while the heat flux is free ($\Theta|_{int} \equiv constant$, $\partial_{\vec{n}}\,\Theta|_{int} \equiv free$). The temperature is normalized as

$$\Theta = \frac{T|_{int} - T}{T|_{int} - T_b}, \quad \Longrightarrow \quad \left\langle \left.\frac{\partial \Theta}{\partial \vec{n}}\right|_{int} \right\rangle = Nu, \quad \Theta|_{int} = 0, \quad \Theta_b = 1. \tag{4.17}$$

Equalities on the right-side of the arrow can be easily obtained analogously to the *IF* case. The temperature transport equation and the corresponding boundary condition for locally imposed temperature respectively are

$$\frac{\partial \Theta}{\partial t} = -\vec{u} \cdot \vec{\nabla}\Theta + \frac{1}{RePr}\nabla^2\Theta + \left(-u_x \frac{\beta}{RePr}\left\langle \frac{\partial \Theta}{\partial \vec{n}}\bigg|_{int}\right\rangle\right), \tag{4.18}$$

$$\Theta|_{int} = 0, \tag{4.19}$$

where the amplitude of the source term f_Θ/u_x is

$$\frac{f_\Theta}{u_x} = \frac{\beta}{RePr}\left\langle \frac{\partial \Theta}{\partial \vec{n}}\bigg|_{int}\right\rangle = -\frac{\beta Nu}{RePr}, \quad where\ \beta = \begin{cases} 2, & for\ channel\ flow, \\ 4, & for\ pipe\ flow. \end{cases} \tag{4.20}$$

From average values of the source term amplitude or of the dimensionless heat flux at the interface (Section 5.2.2), the Nusselt number can be estimated as

$$Nu \approx \frac{RePr}{\beta}\left\langle \frac{f_\Theta}{u_x}\right\rangle \qquad or \qquad Nu \approx \langle \partial_{\vec{n}}\, \Theta|_{int}\rangle. \tag{4.21}$$

4.3.3 Ideal locally imposed uniform temperature

This boundary condition corresponds to the hypothetical case in which the temperature is constant and uniform. The temperature transport equation and interface boundary condition, respectively, are

$$\frac{\partial \Theta}{\partial t} = -\vec{u} \cdot \vec{\nabla}\Theta + \frac{1}{RePr}\nabla\Theta + \Theta\frac{\beta Nu}{RePr}\left[-u_x + \frac{\beta Nu}{(RePr)^2}\right], \tag{4.22}$$

$$\Theta|_{int} = 0. \tag{4.23}$$

It is interesting to note that this source term also depends on the temperature field. As it is shown in Appendix A, this dependence occurs because of the variation of the streamwise

bulk temperature gradient along the duct causing that the scaling factor of the temperature normalization ($T|_{int} - T_b$) is function of x (Figure 4.2).

In heated/cooled internal flow, the temperature increases/decreases along the duct, thus the temperature is scaled to compensate these increments/decrements. This give rise to the streamwise energy source term. In order to summarize the previous considerations on ideal thermal boundary conditions, the Table 4.1 shows the dimensionless temperature, the forcing term expression and some relevant quantities including the bulk temperature, temperature value and gradient at the wall.

Tabela 4.1: Main considerations of the ideal boundary conditions.

$$\frac{\partial \Theta}{\partial t} = -\vec{u} \cdot \vec{\nabla}\Theta + \frac{1}{RePr}\nabla^2\Theta + f_\Theta$$

Thermal boundary condition	Dimensionless temperature Θ	Forcing term f_Θ	Relevant dimensionless quantities
IF	$-\frac{1}{Nu}\left(\frac{T - T_b}{T\|_{int} - T_b}\right)$	$u_x \frac{\beta}{RePr}\left(\left.\frac{\partial \Theta}{\partial \vec{n}}\right\|_{int}\right)$	$\left.\frac{\partial \Theta}{\partial \vec{n}}\right\|_{int} = 1, \quad \langle \Theta\|_{int} \rangle = -1/Nu, \quad \Theta_b = 0$
IT	$\frac{\langle T\|_{int} \rangle - T}{\langle T\|_{int} \rangle - T_b}$	$u_x \frac{\beta}{RePr}\left\langle \left.\frac{\partial \Theta}{\partial \vec{n}}\right\|_{int} \right\rangle$	$\left\langle \left.\frac{\partial \Theta}{\partial \vec{n}}\right\|_{int} \right\rangle = Nu, \quad \Theta\|_{int} = 0, \quad \Theta_b = 1$
IUT	$\frac{\langle T\|_{int} \rangle - T}{\langle T\|_{int} \rangle - T_b}$	$\Theta \frac{\beta Nu}{RePr}\left[-u_x + \frac{\beta Nu}{(RePr)^2}\right]$	$\left\langle \left.\frac{\partial \Theta}{\partial \vec{n}}\right\|_{int} \right\rangle = Nu, \quad \Theta\|_{int} = 0, \quad \Theta_b = 1$

4.3.4 Domain configuration

For *IF* and *IT* cases, the computational domain contains the inner fluid, the two solid slabs for channel (or the solid cylindrical shell for pipe) and the outer domain with still fluid. On the other hand, under *CHT*, the computational domain does not contain outer fluid domain, thus the outer slab faces coincide with the computational boundary (Figure 4.3). The computational domains is periodic in all directions, excepting for *CHT* case, for which a Neumann boundary condition is imposed on the outer boundary.

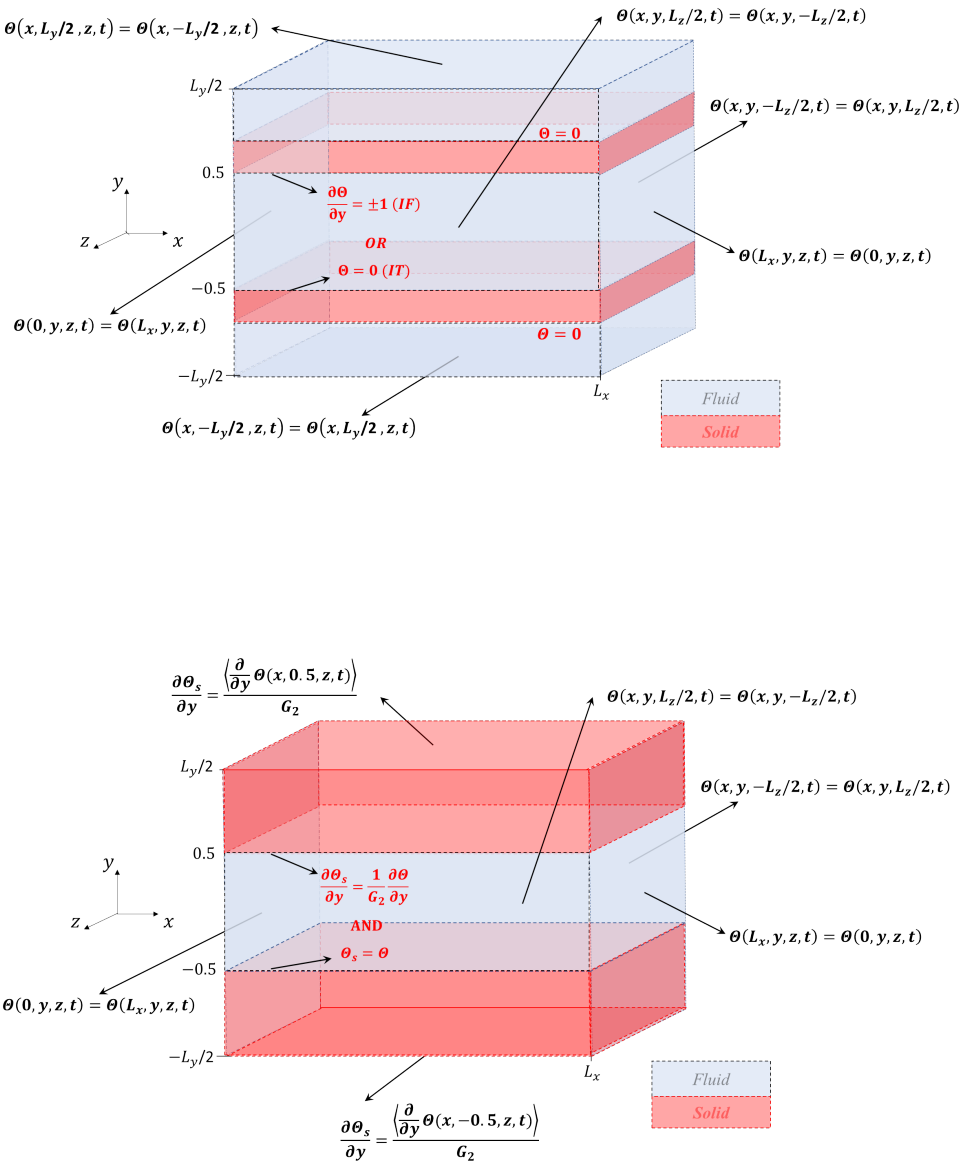

Figura 4.3: Scheme of the domain configuration and thermal boundary conditions, for channel setup. Top: imposed temperature (*IT*) or heat flux (*IF*); bottom: Conjugate heat transfer. In black, the boundary conditions at the domain faces; in red, the boundary conditions at the immersed boundary.

Chapter 5

Numerical methodology

A current challenger problem of great interest is to develop numerical methods for the conservation laws with the following properties: that it be conservative, high-order accurate, geometrically flexible, computationally efficient, and simply formulated and implemented. Aiming to deal with these challenges, in solving heat transfer in internal flows, the numerical methodology is described at this chapter. This includes descriptions of the numerical schemes (for the spatial and temporal discretization), the immersed boundary strategy (to represent the solid geometry), considerations on numerical stability, fluid-solid coupling strategy (to deal with the fluid-solid thermal interaction) and the parallel computing strategy.

In order to solve numerically the fluid dynamic (Eq. 4.1, 4.2 and 4.3) and heat transfer (Eq. 4.5, 4.6, 4.7, 4.8 and 4.9) governing equations, the code *Incompact3d* is employed (Laizet & Lamballais, 2009[48]). The *Incompact3d* code is an open source code written in Fortran90/95, for solving incompressible turbulent flows via Direct numerical simulation (*DNS*) and Large eddy simulation (*LES* and implicit-*LES* - *ILES*). The code is based on **6$^{\text{th}}$-order compact schemes of finite differences**, for spatial differentiation in a **Cartesian mesh**. By default, the code has implemented 4 explicit temporal schemes: Adams-Bashforth (2^{nd}- and 3^{th}- order) and Runge-Kutta (3^{th}- and 4^{th}- order) schemes. Runge-Kutta schemes use sub-time steps, which requires matrix inversion every time step and, according to Laizet *et al.* (2010)[49], it could lead to deterioration of the no-slip condition at the immersed solid boundary. Thus, a **3$^{\text{th}}$-order Adams-Bashforth scheme** is adopted, for time advancement. To treat the incompressibility condition, a **fractional step method** requires solving a Poisson equation of pressure, which is

fully solved in spectral space by a **3D Fast Fourier Transform**. More information and versions of the code can be found in `http://www.incompact3d.com/`.

In this work, especial atention is given to the body geometrical representation which is carried out by mean of an immersed boundary method (*IBM*) based on an adapted direct forcing method (Gautier *et al.*, 2014[22]). This method consists in reconstructing the field inside the immersed mesh region, in order to ensure smoothness (*e. i.* first derivative continuity) at the fluid-solid interface and improve the performance of high-order compact schemes.

5.1 Spatial discretization

The spatial derivatives, in a Cartesian computational mesh, are computed *via* compact schemes of finite differences described by Vichnevetsky & Bowles (1982)[104], Lele (1992)[55], Guerreiro (2000)[29] and Moin (2001)[63]. The mesh spacing is adopted as uniform in all directions (no stretching).

5.1.1 Compact schemes

Here, it will be assumed a computational domain of size $[0, L_x]$, with uniform mesh spacing Δx, and discrete coordinates $x_i = (i-1)\Delta x$ (with $1 \leq i \leq N_x$). If the function $f(x)$ evaluated at x_i is $f(x_i) = f_i$, the first and second discrete derivatives (f_i' and f_i'') can be estimated by the numerical schemes presented in Table 5.1 and Table 5.2, respectively. For periodic and free-slip boundary conditions, the 6^{th}- order scheme can be applied over all the mesh nodes ($1 \leq i \leq N_x$), while, for Dirichlet boundary conditions, the boundary nodes ($i = 1$ and $i = N_x$) are treated with a 3^{th}- order scheme and the nodes adjacent to the boundary ($i = 2$ and $i = N_x - 1$) with a 4^{th}- order scheme.

The compact schemes, presented in Tables 5.1 and 5.2, can be expressed in matricial form as

$$A_x' \vec{f'} = B_x' \vec{f}, \tag{5.1}$$

$$A_x'' \vec{f''} = B_x'' \vec{f}, \tag{5.2}$$

where, A_x', B_x', A_x'' and B_x'' are matrices of size $N_x \times N_x$. $\vec{f}$, $\vec{f'}$ and $\vec{f''}$ are vectors containing,

Tabela 5.1: Compact numerical schemes of finite differences to compute the *first derivative* (f_i') of the function $f_i = f(x_i)$ at the nodes $x_i = (i-1)\Delta x$, $1 \leq i \leq N_x$, uniform mesh spacing Δx. Table adapted from Pinto (2012)[81].

Scheme	**Mesh nodes:** $3 \leq i \leq N_x - 2$	**Coefficients**
6^{th}-order centered	$\alpha' f'_{i-1} + f'_i + \alpha' f'_{i+1} = a' \frac{f_{i+1} - f_{i-1}}{2\Delta x} + b' \frac{f_{i+2} - f_{i-2}}{4\Delta x} + c' \frac{f_{i+3} - f_{i-3}}{6\Delta x}$	$\alpha' = \frac{1}{3}; a' = \frac{14}{9}; b' = \frac{1}{9}; c' = 0$
	Mesh nodes: $i = 1$ and $i = N_x$	**Coefficients**
3^{th}-order non-centered	$f'_1 + \alpha' f'_2 = \frac{a' f_1 + b' f_2 + c' f_3}{\Delta x}$ $f'_N + \alpha' f'_{N-1} = \frac{-a' f_{N_x} - b' f_{N_x-1} - c' f_{N_x-2}}{\Delta x}$	$\alpha' = 2; a' = -\frac{5}{2}; b' = 2; c' = \frac{1}{2}$
	Mesh nodes: $i = 2$ and $i = N_x - 1$	**Coefficients**
4^{th}-order centered	$\alpha' f'_1 + f'_2 + \alpha' f'_3 = a' \frac{f_3 - f_1}{2\Delta x}$ $\alpha' f'_{N_x-2} + f'_{N_x-1} + \alpha' f'_{N_x} = a' \frac{f_{N_x} - f_{N_x-2}}{2\Delta x}$	$\alpha' = \frac{1}{4}; a' = \frac{3}{2}$

Tabela 5.2: Compact numerical schemes in finite differences to compute the *second derivative* (f_i'') of the function $f_i = f(x_i)$ at the nodes $x_i = (i-1)\Delta x$, $1 \leq i \leq N_x$, and uniform mesh spacing Δx. Table adapted from Pinto (2012)[81].

Scheme	**Nodes:** $3 \leq i \leq N_x - 2$	**Coefficients**
6^{th}-order centered	$\alpha'' f''_{i-1} + f''_i + \alpha'' f''_{i+1} = a'' \frac{f_{i+1} - 2f_i + f_{i-1}}{\Delta x^2} + b'' \frac{f_{i+2} - 2f_i + f_{i-2}}{4\Delta x^2} + c'' \frac{f_{i+3} - 2f_i + f_{i-3}}{9\Delta x^2}$	$\alpha'' = \frac{2}{11}; a'' = \frac{12}{11}; b'' = \frac{3}{11}; c'' = 0$
	Mesh nodes: $i = 1$ and $i = N_x$	**Coefficients**
3^{th}-order non-centered	$f''_1 + \alpha'' f''_2 = \frac{a'' f_1 + b'' f_2 + c'' f_3 + d'' f_4}{\Delta x^2}$ $f''_{N_x} + \alpha'' f''_{N_x-1} = \frac{a'' f_{N_x} + b'' f_{N_x-1} + c'' f_{N_x-2} + d'' f_{N_x-3}}{\Delta x^2}$	$\alpha'' = 11; a'' = 13; b'' = -27; c'' = 15; d'' = -1$
	Mesh nodes: $i = 2$ and $i = N_x - 1$	**Coefficients**
4^{th}-order centered	$\alpha'' f''_1 + f''_2 + \alpha'' f''_3 = a'' \frac{f_3 - 2f_2 + f_1}{\Delta x^2}$ $\alpha'' f''_{N_x-2} + f''_{N_x-1} + \alpha'' f''_{N_x} = a'' \frac{f_{N_x} - 2f_{N_x-1} + f_{N_x-2}}{\Delta x^2}$	$\alpha'' = \frac{1}{10}; a'' = \frac{6}{5}$

respectively, the function, the first derivative and second derivative evaluated at the N_x mesh nodes. The matrices A'_x and A''_x are tridiagonal, while B'_x and B''_x are pentadiagonal, but their characteristics depend on the boundary condition. For instance, a periodic domain is represented by cyclic matrices. More considerations on boundary conditions are discussed in Gautier (2013)[20].

When $c' \neq 0$ and $c'' \neq 0$ (Table 5.1 and 5.2) the scheme is up to 8^{th}-order accurate (B'_x and B''_x would be heptadiagonal) under the coefficients constraints

$$a' + b' + c' = 1 + 2\alpha', \qquad a'' + b'' + c'' = 1 + 2\alpha'', \qquad \mathcal{O}(\Delta x^2), \tag{5.3}$$

$$a' + 2^2 b' + 3^2 c' = 2\tfrac{3!}{2!}\alpha', \qquad a'' + 2^2 b'' + 3^2 c'' = \tfrac{4!}{2!}\alpha'', \qquad \mathcal{O}(\Delta x^4), \tag{5.4}$$

$$a' + 2^4 b' + 3^4 c' = 2\tfrac{5!}{4!}\alpha', \qquad a'' + 2^4 b'' + 3^4 c'' = \tfrac{6!}{4!}\alpha'', \qquad \mathcal{O}(\Delta x^6), \tag{5.5}$$

$$a' + 2^6 b' + 3^6 c' = 2\tfrac{9!}{8!}\alpha', \qquad a'' + 2^6 b'' + 3^6 c'' = \tfrac{8!}{6!}\alpha'', \qquad \mathcal{O}(\Delta x^8), \tag{5.6}$$

5.1.2 Modified wave number

It can be shown that, in the spectral Fourier space, the derivatives of the function f ($\hat{f}'$ and $\hat{f}''$) can be written as being proportional to the Fourier transform of the function ($\hat{f}$)

$$\hat{f}' = \imath k_x \hat{f}, \tag{5.7}$$

$$\hat{f}'' = -k_x^2 \hat{f}, \tag{5.8}$$

where $\hat{(\cdot)}$ is the Fourier transform operator, $\imath = \sqrt{-1}$ and k_x is the wavenumber. If the function is time-spatial dependent, the wavenumber analysis can be strictly applied, only if the function can be decoupled in the product of a time dependent by a space dependent functions. Numerical schemes can be applied over the spatial function f (for instance, schemes in Table 5.1 and 5.2) to estimate its derivatives ($f' \approx f'_{fd}$ and $f'' \approx f''_{fd}$), and through the concept of modified wavenumber k'_x and modified square wavenumber k''_x to obtain the following relation

$$\hat{f}'_{fd} = \imath k''_x \hat{f}, \tag{5.9}$$

$$\hat{f}''_{fd} = -k''_x \hat{f}. \tag{5.10}$$

Now, the relation between the numerical approximation and the exact solution of the derivatives can be established by comparing the exact and modified wavenumbers of Equations 5.7 and 5.8 to Equations 5.9 and 5.10. Applying 6^{th}-order compact schemes (with $c' \neq 0$ and $c'' \neq 0$) to the test function $f(x) = e^{\iota k_x x}$, in the framework of the Fourier analysis, it can be verified that

$$k'_x \Delta x = \frac{2a' sin(k_x \Delta x) + \frac{b'}{2} sin(2k_x \Delta x) + \frac{c'}{3} sin(3k_x \Delta x)}{1 + 2\alpha' cos(k_x \Delta x)}, \tag{5.11}$$

$$k''_x \Delta x^2 = \frac{2a'' (1 - cos(k_x \Delta x)) + \frac{b''}{2} (1 - cos(2k_x \Delta x)) + \frac{2c''}{9} (1 - cos(3k_x \Delta x))}{1 + 2\alpha'' cos(k_x \Delta x)}. \tag{5.12}$$

Figure 5.1 shows the performance of explicit schemes in relation to compact schemes, by comparing the modified wave number from the numerical scheme (k'_x and k''_x) to the exact one (k_x). In this figure, it is also considered the 6^{th}-order scheme with coefficients $(c',\ c'') \neq (0,\ 0)$, which is obtained by an optimization algorithm (Annex B of Flageul (2015)[16]). From this algorithm, the optimal set of coefficients, to compute the first derivative, is

$$(\alpha',\ a',\ b',\ c') \approx (0.469,\ 1.58,\ 0.401,\ -0.0407)\,. \tag{5.13}$$

Compact schemes have better performance than the explicit counterparts, which is more evident for the wavenumber associated to the first derivative (Figure 5.1).

5.1.3 Numerical dissipation (Implicit Large Eddy Simulation)

Lamballais *et al.* (2011)[51] propose a simple methodology to adjust the numerical dissipation in the second derivative computed by compact schemes. This approach permits to control the shape of the dissipation spectrum (Figure 5.1b) in the smallest scales (around the cutoff wavenumber: $k_x \Delta x|_{cutoff} = k_{x_c} \Delta x = \pi$). In *DNS*, this property could be used in wiggles control, while within Large Eddy Simulation (*LES*) framework, connections with hyperviscosity ([6], [52]) and spectral vanish viscosity ([35], [75]) can be established. The recent work of Dairay *et al.*(2017)[10] presents this numerical dissipation as an alternative strategy to perform Impli-

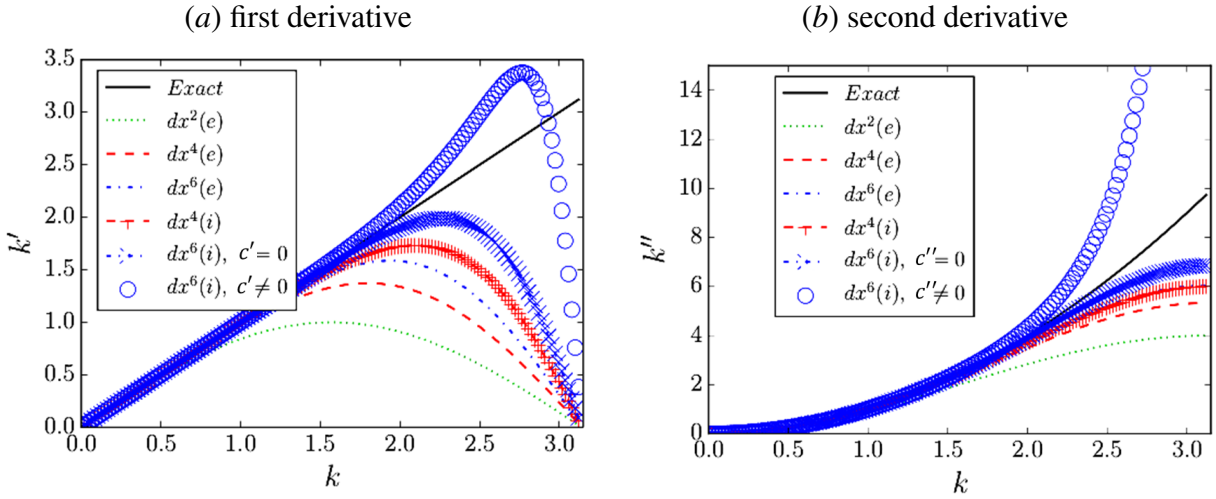

Figura 5.1: Modified wavenumber associated to the first and second derivative (k'_x and k''_x), for explicit schemes ($dx(e)$) of 2^{nd}-, 4^{th}- and 6^{th}- order (adapted from Tables 5.1 and 5.2 with $\alpha' = \alpha'' = 0$), and compact schemes ($dx(i)$) of 4^{th}- and 6^{th}- order. Figure adapted from Ph.D. work of Flageul (2015)[16].

cit Large Eddy Simulation (*ILES*), by equivalence with explicit sub-grid-scale modeling with physic basis, as spectral vanish viscosity.

It is possible to modulate the numerical dissipation by selecting the appropriate set of coefficients associated to the second-derivative discrete operator. From Equation 5.12, the modified square wavenumber admits a singularity at $k_{x_c}\Delta x$ when $\alpha'' \longrightarrow 1/2$ ($k''_{x_c}\Delta x \longrightarrow \infty$). This suggests that the dissipation can be modulated at the cutoff scale. By evaluating k''_x at k_{x_c} (Equation 5.12) and preserving the 6^{th}-order accuracy (constraints 5.3, 5.4 and 5.5), it can be establish

$$\alpha'' = \frac{272 - 45k''_{x_c}\Delta x^2}{416 - 90k''_{x_c}\Delta x^2}, \quad a'' = \frac{48 - 135k''_{x_c}\Delta x^2}{1664 - 360k''_{x_c}\Delta x^2}, \quad b'' = \frac{528 - 81k''_{x_c}\Delta x^2}{208 - 45k''_{x_c}\Delta x^2},$$
$$c'' = \frac{-432 + 63k''_{x_c}\Delta x^2}{1664 - 360k''_{x_c}\Delta x^2}. \tag{5.14}$$

In theses expressions, the modified square wavenumber at the mesh cutoff k''_{x_c} can be freely selected by the user as proportional, for instance, to the exact value of the cutoff square wave number $k^2_{x_c}$ ($k''_{x_c} = \alpha_{cut}k^2_{x_c} = \alpha_{cut}\pi^2/\Delta x^2$, where α_{cut} is the proportionality factor). Figure 5.2 displays the $k''_x\Delta x^2$ against $k^2_x\Delta x^2$, for the conventional 6^{th}-order scheme ($c'' = 0$, Table 5.2) and various modified square cutoff wavenumber ($k''_{x_c}\Delta x^2 = \alpha_{cut}\pi^2$ with $\alpha_{cut} = 1, 2, ..., 10$).

The numerical dissipation is concentrated in the smallest scales, even for high values of $k''_{x_c}\Delta x^2$. This bandwidth can be extended by fixing another $k''_x\Delta x^2$ in an intermediate value ($k_{x_m}\Delta x$). If $c'' = 0$, this requires reducing the scheme order to 4^{th}-order, since the new constrains are 5.3, 5.4 and Equation 5.12 evaluated in k_{x_c} and k_{x_m}. However, by selecting $c'' \neq 0$ and adding the constrain 5.5 the $6^{th}-$order accuracy can be preserved. Lamballais *et al.*(2011)[51] discusses this strategy with more details. Note that in the present work, only $k''_{x_c}\Delta x^2 = \alpha_{cut}\pi^2$ is adjusted in each simulation, depending on the flow configuration.

When $k''_{x_c}\Delta x^2$ is incremented, it should be pointed out that numerical stability is limited by the Fourier number

$$\frac{\nu\Delta t}{\Delta x^2} \leq \frac{\sigma_r}{k''_{x_c}\Delta x^2} = \frac{\sigma_r}{\alpha_{cut}\pi^2}, \tag{5.15}$$

where, σ_r depends on the stability region of the time advancement scheme in the real axis ($\sigma_r \approx -0.545$ for an Adams-Bashforth 3^{th}-order scheme).

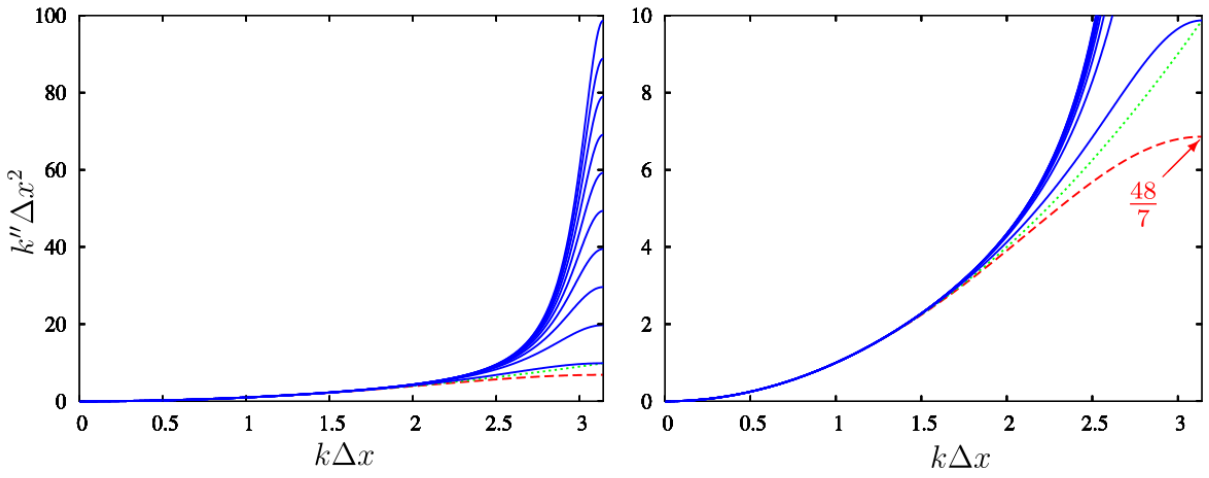

Figura 5.2: Modified square wavenumber in compact centered schemes of 6^{th}-order accuracy. Comparison between the cutoff wavenumber $k''_{x_c}\Delta x^2 = \alpha_{cut}\pi$ with $\alpha_{cut} = 1, 2, ..., 10$ (blue lines), the exact modified square wavenumber $k^2\Delta x^2$ (green dotted line) and the scheme presented in Table 5.2 with $c'' = 0$ (red dashed line). Figure adopted from Lamballais *et al.* (2011)[51].

5.1.4 Staggered mesh for pressure

A Cartesian collocated mesh (velocity and pressure solved at the same mesh nodes) can yield spurious pressure oscillations, as it was identified by Laizet & Lamballais (2009)[48].

According to Perot (2000)[76], a staggered mesh does not exhibit spurious pressure mode and shows conservative properties of mass, momentum and kinetic energy. These characteristics led to employ a staggered mesh for pressure computation (Figure 5.3). Thus, the Poisson equation (Subsection 5.2.1), to solve the pressure field, requires to interpolate the pressure and intermediate velocity (associated to the fractional time step, Section 5.2) to the center of the mesh.

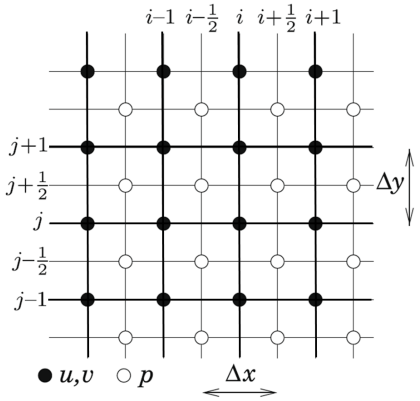

Figura 5.3: Schema 2D of a Cartesian staggered mesh for pressure (∘) and collocated for velocity (•). Figure adopted from Laizet & Lamballais 2009[48].

Considering that the values of f at the coordinate $x_i = (i-1)\Delta x$ are known, the function value ($f_{i+1/2}$) and the first derivative ($f'_{i+1/2}$) at the center of the mesh can be, respectively, computed as

$$\alpha^I f_{i-1/2} + f_{i+1/2} + \alpha^I f_{i+3/2} = a^I \frac{f_{i+1} - f_i}{2} + b^I \frac{f_{i+2} - f_{i-1}}{2}, \tag{5.16}$$

$$\alpha' f'_{i-1/2} + f'_{i+1/2} + \alpha' f'_{i+3/2} = a' \frac{f_{i+1} - f_i}{\Delta x} + b' \frac{f_{i+2} - f_{i-1}}{3\Delta x}. \tag{5.17}$$

This schemes have 6^{th}-order accuracy when $(\alpha^I,\ a^I,\ b^I) = (3/10, 3/4, 1/20)$ and $(\alpha',\ a',\ b') = (9/62, 63/62,\ 17/62)$. The matricial form reads

$$D^I_x \vec{f} = E^I_x \vec{f}, \tag{5.18}$$

$$D'_x \vec{f'} = E'_x \vec{f}, \tag{5.19}$$

where, $vec f$ and $\vec{f'}$ respectively are the vectors of the function and its first derivative at the staggered mesh. The matrices are defined in the Ph.D. Thesis of Laizet (2005)[47], for periodic, Dirichlet and free-slip boundary conditions.

5.2 Temporal advancement

By default the *Incompact3d* code has 4 explicit temporal schemes implemented: 3^{th}- and 4^{th}- order Runge-Kutta schemes and 2^{th}- and 3^{th}- order Adams-Bashforth schemes. For the terms associated with the first derivative (convective terms), the time step Δt must verify the following stability criteria:

$$\frac{max(u_x)\ \Delta t}{\Delta x} \leq \frac{\sigma_\iota}{max\,(k'_x)}, \tag{5.20}$$

where σ_ι is the limit of the stability region in the imaginary axis ($\sigma_\iota \approx 0.723$ for 3^{th}-order Adams-Bashforth scheme). The stability criteria is exemplified for x-direction, but the same could be adopted in y- and z- directions with the corresponding velocity component (u_y or u_z), mesh spacing (Δy or Δz) and modified wavenumber (k'_y or k'_z).

5.2.1 Fluid dynamics equations

Runge-Kutta schemes require matrix inversion every sub-time step and could lead to accuracy loss on the no-slip condition at the immersed boundary (Laizet *et al.*, 2009[48]). Thus, fluid dynamic equations (4.1 and 4.2) are integrated in time by a **3^{th}- order Adams-Bashforth scheme** together with a **fractional time step method**, to deal with the pressure, couple the incompressibility condition and ensure a constant bulk velocity. As first step, an intermediary velocity ($\vec{u}^*$) is **predicted** by

$$\frac{\vec{u}^* - \vec{u}^n}{\Delta t} = \frac{3}{2}\aleph'\left[\vec{u}^n\right] - \frac{1}{2}\aleph'[\vec{u}^{n-1}], \tag{5.21}$$

where $\aleph'\left[\vec{u}\right]$ is the convective-diffusive discrete operator computed by compacts schemes (Section 5.1.1) and the superscript represents the time level at which the variable is evaluated (for instance, $\vec{u}^n = \vec{u}(t^n,x,y,z)$). It should be stressed that the convective term is computed in the skew-symmetric formulation

$$\aleph'\left[\vec{u}\right] = -\frac{1}{2}\left[\vec{\nabla}'\left(\vec{u}\otimes\vec{u}\right) + \left(\vec{u}\cdot\vec{\nabla}'\right)\vec{u}\right] + \frac{1}{Re}\nabla^{2'}\vec{u}, \tag{5.22}$$

where the apostrophe indicates discrete operators. **Remark**: the forcing term $\vec{f}_{IB}$, which arises

from the *IBM* direct forcing formulation, does not appears. This is, basically, due to the 1D nature of the Reconstruction Method by Alternated Direction ([21]) used in this study, since the forcinf term $\vec{f}_{IB}^{n+1}$ cannot be explicitly expressed in the volumetric form, but it is considered during the discrete derivatives computation ($\aleph\,[\vec{u}]$).

As the pressure has not been considered, the intermediate velocity $\vec{u}^*$ is not divergence free. Moreover, the pressure drop has not been compensated and thereby the bulk intermediate velocity U_b^* is not unitary. Then, in a second stage the velocity is **corrected** into two steps

$$\frac{\vec{u}^{**} - \vec{u}^*}{\Delta t} = \vec{f}_\tau^{n+1}, \tag{5.23}$$

$$\frac{\vec{u}^{n+1} - \vec{u}^{**}}{\Delta t} = -\vec{\nabla}\Pi^{n+1}. \tag{5.24}$$

where the constant streamwise forcing term $\vec{f_\tau} = [f_\tau\ 0\ 0]^T$ appears in periodic flow to compensate the net viscous friction at the wall, driving the flow in streamwise direction. This means that f_τ compensates the streamwise mean pressure gradient lost due to friction stresses. For the simulations in this work, the instantaneous mean pressure gradient $d\langle\Pi\rangle_{y,z}/dx$ is adjusted every time step. This is done in such a way that the bulk velocity becomes constant and unitary throughout the simulation ($U_b = 1$, in such a way that volumetric flow rate remains constant):

$$f_\tau^{n+1} = \frac{d\langle\Pi^{n+1}\rangle_{y,z}}{dx} \approx f_\tau^* = \frac{\left(U_b - U_b^*\right)}{\Delta t}, \tag{5.25}$$

where the unadjusted bulk velocity U_b^* is time dependent, thus the magnitude of this adjustment is time-averaged to estimate Re_τ and u_τ by Equation 4.4. It means, that Re is set while Re_τ is estimated by

$$Re_\tau \approx \frac{Re}{2}\sqrt{\frac{1}{\beta}\left(\frac{U_b - \left\langle U_b^*\right\rangle}{\Delta t}\right)}. \tag{5.26}$$

Note that $u_\tau = (\nu/L_c)\,Re_\tau$ is a space/time-average estimation since the adjustment was applied to the mean pressure gradient.

Pressure treatment

Applying divergence operator on both sides of Equation 5.24, the following Poisson equation can be written

$$\nabla^2 \Pi^{n+1} = \frac{\vec{\nabla} \cdot \vec{u}^* - \vec{\nabla} \cdot \vec{u}^{n+1}}{\Delta t}. \tag{5.27}$$

In order to locate the immersed body (in *IBM* context) a variable ε is introduced, which is $\varepsilon = 1$ inside the solid and $\varepsilon = 0$ outside. Under this consideration, the incompressibility condition in Equation 5.27 is estimated by

$$\vec{\nabla} \cdot \vec{u}^{n+1} = \vec{\nabla} \cdot \left(\varepsilon \vec{u}^{n+1}\right) \approx \vec{\nabla} \cdot \left(\varepsilon \vec{u}^*\right), \tag{5.28}$$

giving the following Poisson equation

$$\nabla^2 \Pi^{n+1} = \frac{\vec{\nabla} \cdot \left[(1-\varepsilon)\, \vec{u}^*\right]}{\Delta t}, \tag{5.29}$$

Before proceeding to solve the pressure field, $\vec{u}^{**}$ is taken to the staggered mesh via the 6^{th}-order interpolation (Equation 5.16).

Equation 5.29 in the spectral space is

$$\hat{\Pi}_{lmn}^{k+1} = \frac{\hat{D}_{lmn}}{F_{lmn}}, \tag{5.30}$$

where $\hat{D}_{lmn}$ is the divergence in the spectral domain, and the spectral factor is expressed by

$$F_{lmn} = -[(k'_x T_y T_z)^2 + (k'_y T_x T_z)^2 + (k'_z T_x T_y)^2]\Delta t, \tag{5.31}$$

where the transference functions (T_j with $j = x,\ y,\ z$) are

$$T_j(k_j \Delta j) = \frac{2a\ cos(k_j \Delta j/2) + (2b/3)\ cos(3k_j \Delta j/2)}{1 + 2\alpha\ cos(k_j \Delta j)}. \tag{5.32}$$

The numerical transformation from the physical to the spectral space is carried out by applying a 3D Fast Fourier Transform (Laizet, 2005[47]). After solving the inverse transform of $\hat{\Pi}_{lmn}^{k+1}$ at the staggered mesh, $\vec{\nabla}\Pi^{k+1}$ is computed and then interpolated to the collocated mesh

(Equations 5.16 and 5.17), in order to correct the velocity field in t^{n+1} by Equation 5.24.

5.2.2 Fluid-solid thermal equations

As the thermal equations in fluid and solid domain have not pressure (Eq. 4.5 and 4.6), they are integrated in time without the fractional time step associated to the projection technique. After solving the velocity field in the fluid domain, the **fluid temperature** is predicted by a 3^{th}-order Adam-Bashforth scheme expressed by

$$\frac{\Theta^* - \Theta^n}{\Delta t} = \frac{3}{2}\left(\vec{u}^n \nabla\Theta^n + \frac{1}{RePr}\nabla^2\Theta^n\right) - \frac{1}{2}\left(\vec{u}^{n-1}\nabla\Theta^{n-1} + \frac{1}{RePr}\nabla^2\Theta^{n-1}\right), \tag{5.33}$$

$$\frac{\Theta^{n+1} - \Theta^*}{\Delta t} = f_\Theta^{n+1}, \tag{5.34}$$

while, the **solid temperature** is giving by

$$\begin{aligned}\frac{\Theta_s^{n+1} - \Theta_s^n}{\Delta t} \quad = \quad & \frac{1}{GRePr}\left\{2\left[\frac{\partial^2\Theta_s}{\partial x^2} + (1-\kappa)\frac{\partial^2\Theta_s}{\partial y^2} + \frac{\partial^2\Theta_s}{\partial z^2}\right]^n\right. \\ & \left. - \left[\frac{\partial^2\Theta_s}{\partial x^2} + (1-\kappa)\frac{\partial^2\Theta_s}{\partial y^2} + \frac{\partial^2\Theta_s}{\partial z^2}\right]^{n-1} + \kappa\frac{\partial^2\Theta_s^{n+1}}{\partial y^2}\right\},\end{aligned} \tag{5.35}$$

where the f_Θ is the source term which compensate the streamwise mean temperature gradient in order to ensure constant bulk temperature $\Theta_b = constant$. This is equivalent to the forcing term f_τ, in the momentum equation, which compensates the streamwise mean pressure gradient. However, f_τ is uniform in space, whereas f_Θ is proportional to the streamwise velocity ($f_\Theta \propto u_x$) and thereby is is not uniform but function of space. As $f_\Theta \propto u_x$, it can be stated that the amplitude of the source term is constant $f_\Theta/u_x = constant$ (Table 4.1). Applying volumetric bulk operator on Equation 5.34, it can be expressed as

$$\frac{1}{U_b\forall}\int_\forall u_x^{n+1} f_\Theta^{n+1} d\forall' = \frac{\frac{1}{U_b\forall}\int_\forall \left(u_x^{n+1}\Theta^{n+1} - u_x^{n+1}\Theta^*\right) d\forall'}{\Delta t}, \tag{5.36}$$

or, by taking advantage from $f_\Theta/u_x = constant$, operating and rearranging the terms, this expression becomes

$$\left(\frac{f_\Theta}{u_x}\right)^{n+1} \frac{1}{U_b \forall} \int_\forall \left(u_x^{n+1}\right)^2 d\forall' = \frac{\Theta_b^{n+1} - \frac{1}{U_b \forall} \int_\forall u_x^{n+1} \Theta^* d\forall'}{\Delta t}, \tag{5.37}$$

where the unknown velocity field in t^{n+1} can be estimated by the intermediate velocity ($u_x^{n+1} \approx u_x^*$), yielding the following temperature source term

$$f_\Theta^{n+1} \approx f_\Theta^* = u_x^* \frac{1}{\frac{1}{U_b \forall} \int_\forall \left(u_x^*\right)^2 d\forall'} \frac{\Theta_b^{n+1} - \Theta_b^*}{\Delta t}, \tag{5.38}$$

where $\Theta_b^{n+1} = (1 \; or \; 0)$ is the value of the target bulk temperature after adjustment, which allows the source term ensures constant bulk temperature at t^{n+1}.

The time advancement scheme of the conduction equation is a 1^{st}-order scheme based on the implicit Euler scheme. The coefficient κ modules the level of implicitness of the diffusive term in y-direction, however here this term is explicitly computed by using $\kappa = 0$. On the other hand, the Neumann-type (*NBC*) and Dirichlet-type (*DBC*) **boundary conditions** of the temperature for the real Conjugate heat transfer problem (Eq. 4.7, 4.8 and 4.9) or the ideal cases (Eq. 4.13, 4.19 and 4.23) are ensured by the *IBM* described in Section 5.3.

As the temperature is convected by the flow velocity and spatial derivatives are computed by mean compact schemes in the same velocity mesh, the stability criterion for the convective term is the same employed in the fluid dynamic equation. However, the diffusive criterion now is based on the thermal diffusivities

$$\frac{\alpha \Delta t}{\Delta x^2} \leq \frac{\sigma_r}{\alpha_{cut} \pi^2}, \qquad \text{in the fluid,} \tag{5.39}$$

$$\frac{\alpha_s \Delta t}{\Delta x^2} \leq \frac{\sigma_r}{\alpha_{cut} \pi^2}, \qquad \text{in the solid,} \tag{5.40}$$

where σ_r corresponds to the limit of the stability region, of the numerical scheme, in the real axis ($\sigma_r = 0.545$ for 3^{th}-order Adam-Bashforth, for instance).

Relation between source/sink term and Nusselt number estimation

In turbulent heated flow in a duct, the magnitude of the local Nusselt number is normally fluctuating and unknown. However, if the a cross-sectional and time averaged Nu is known, under **ideal locally imposed temperature** (IT), the amplitude of the source term (f_Θ/u_x) could be applied as a averaged-constant value (Eq. 4.12)

$$\left\langle \frac{f_\Theta}{u_x} \right\rangle = \frac{\beta}{RePr} \left\langle \left. \frac{\partial \Theta}{\partial \vec{n}} \right|_{int} \right\rangle = \frac{\beta \langle Nu \rangle}{RePr}, \quad where \ \beta = \begin{cases} 2, & for \ channel \ flow \\ 4, & for \ pipe \ flow. \end{cases} \tag{5.41}$$

or by adjusting the bulk temperature Θ_b^* every time step (as it is actually done in this work), in order to maintain $\Theta_b = 1$ (Figure 5.4)

$$\frac{f_\Theta}{u_x}(t) = \frac{1}{\frac{1}{U_b A} \int_A \left(u_x^*\right)^2 dA'} \frac{\Theta_b - \Theta_b^*(t)}{\Delta t}. \tag{5.42}$$

By averaging in time this equation, the expression for the mean amplitude of the forcing term is

$$\left\langle \frac{f_\Theta}{u_x} \right\rangle = \frac{1}{\frac{1}{U_b A} \int_A \left\langle \left(u_x^*\right)^2 \right\rangle dA'} \frac{\Theta_b - \langle \Theta_b^* \rangle}{\Delta t}. \tag{5.43}$$

The integrations, required to obtain the precedent term, are numerically computed by quadrature rules based on interpolating functions (Simpson rule in channel flow or midpoint rectangle rule in pipe flow). Substituting Eq. 5.41 in Eq. 5.43, the Nusselt number can be estimated as

$$\langle Nu \rangle \approx \frac{RePr}{\beta} \left(\frac{\Theta_b - \langle \Theta_b^* \rangle}{\Delta t} \right) \frac{1}{\frac{1}{U_b \forall} \int_\forall \left\langle \left(u_x^*\right)^2 \right\rangle d\forall'}, \qquad \text{where } \Theta_b = (1 \ or \ 0). \tag{5.44}$$

It can be shown (Jakob M, 1958[78]) that Nu is constant along x, thus eliminating any ambiguity in its use as a global quantity. For **ideal locally imposed heat flux** the source term is applied in the same form of Equation 5.43, but the Nusselt number is estimated from the average dimensionless temperature at the interface

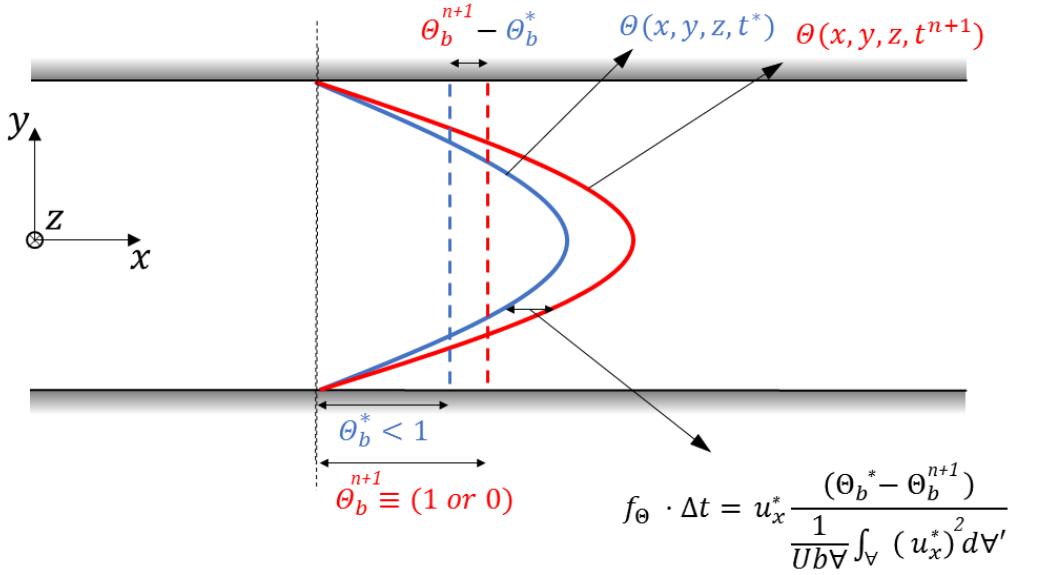

Figura 5.4: Schema of procedure to adjust bulk temperature.

$$\langle Nu \rangle = -\frac{1}{\langle \Theta|_{int} \rangle}. \tag{5.45}$$

5.3 Immersed boundaries treatment

Cartesian mesh is not always compatible or straightforward to be implemented in body conformal methodologies. Thus, the Immersed Boundary Method (*IBM*) is adopted to represent pipe/channel thermal coupling.

5.3.1 Velocity field

For the velocity field, the main objective of the *IBM* is to ensure the **no-slip condition** at the fluid-solid interface. In the direct forcing framework, the simplest approach to represent the solid is to force the target velocity $\vec{u}_0$ to be equal to the solid velocity $\vec{u}_s$ in the solid mesh nodes. For a cylinder in polar coordinates, this is written as

$$\begin{gathered} \vec{u}_0(r,\theta,z,t) = \vec{u}_s(r,\theta,z,t) \\ with\ \ 0 \le r \le D/2\ \ and\ \ 0 \le \theta \le 2\pi. \end{gathered} \tag{5.46}$$

When the target velocity is forced to be null in all the solid nodes, the no-slip condition and the continuity of the velocity could be ensured, but not necessarily the continuity of the first derivative at the fluid-solid interface. In order to solve this undesirable issue, in the compact schemes context, Parnaudeau (2003)[72] a mirrored target velocity field (Figure 5.5). It means, that $\vec{u}_0$ is computed by mirroring the external flow ($\vec{u}$) around the interface and multiplying by a convenient modulate function to deal with the singularity at the cylinder center ($r = 0$). Adopting this strategy, the target velocity reads

$$\vec{u}_0(r,\theta,z,t) = \vec{u}_s + (\vec{u}_s - \vec{u}(D - r,\theta,z,t))\, sin\left(\frac{2\pi r^2}{D^2}\right), \tag{5.47}$$

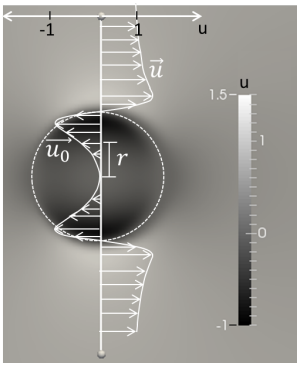

Figura 5.5: Streamwise target velocity inside a cylinder at $Re = 40$, to represent immersed boundaries. Adapted from Narváez (2015)[66].

The techniques (5.46) and (5.47) will be denoted as IBM_{unif} and IBM_{mirr}, respectively. As $\vec{u}_0$ is defined in a Cartesian mesh the reflected field in the polar system $\vec{u}(D - r,\theta,z,t)$ has to be interpolated. According to Parnaudeau *et al.* (2008)[74], the no-slip condition at the immersed boundary cannot reach accuracy higher than second order. Then, a bilinear spatial interpolation is enough to mirror the external flow. Figure 5.6 shows vorticity iso-lines for flow around a cylinder at $Re = 40$ by using the direct forcing methods IBM_{unif} and IBM_{mirr}. The induced discontinuity of the IBM_{unif} technique implies accuracy reduction, which is projected in spurious pressure and velocity oscillations at the interface (Gautier, 2013[20]).

When the submersed solid geometry is not as simple as the cylindrical one, the IBM_{mirr} technique has some limitation listed below:

- Difficulty to select a convenient modulate function to avoid singularities.

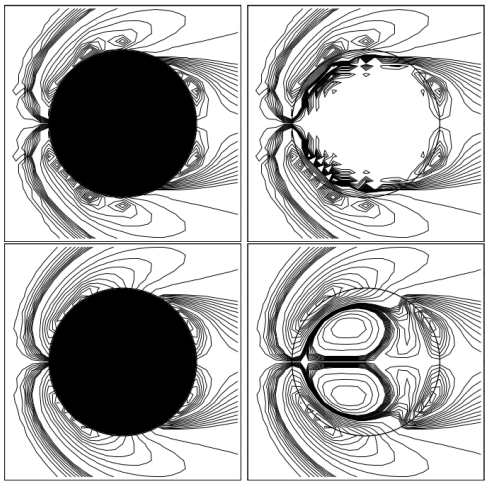

Figura 5.6: Vorticity iso-lines around a cylinder at $Re = 40$ by using the direct forcing method IBM_{unif} (top) and the mirrored flow method IBM_{mirr} (bottom). With internal flow (left) and without internal flow (right). Adapted from Gautier (2013)[20].

- Geometric problems to deal with edges.
- Incompatibility with the computational parallelization strategy, while the parallelization requires 1D derivations, the IBM_{mirr} needs 2D information.

These limitations reduce widely the applicability range of the code to represent complex geometries. Therefore, Gautier (2013)[20] developed an alternative direct forcing method (so-called Reconstruction Method by Alternated Direction, $IBM_{interpol.}$) which can deal with complex geometries and the parallelization strategy. Roughly, this technique consists in to use information from the fluid domain, to adjust a Lagrange interpolating polynomial in the solid domain (Figure 5.7) during the derivatives computation. This interpolation process will be referred to as **reconstruction** of the velocity or thermal field.

5.3.2 Thermal field

The **Dirichlet-type thermal boundary conditions**, required at the fluid-solid interface (Eq. 4.19, 4.23 and 4.7), are imposed in the same way in which the velocity no-slip condition is ensured (Subsection 5.3.1). On the other hand, under *IF* and *CHT* thermal conditions, the heat flux prescription (first directional derivative) is required at the fluid-solid interface (Eq. 4.19, 4.23 and 4.7) and the computational boundaries (Eq. 4.9). In this work, this condition is not

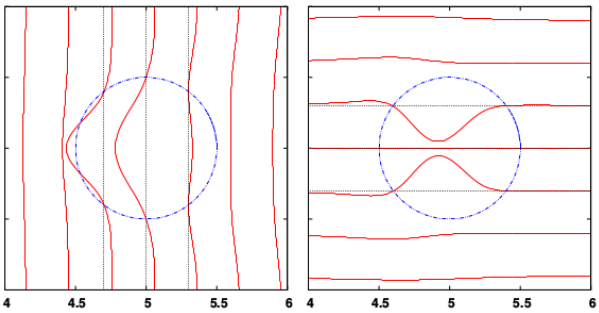

Figura 5.7: 2D reconstructed velocity profiles inside a cylinder via Reconstruction Method by Alternated Direction. Streamwise velocity (left) and cross-wise velocity (right). Figure adapted from Gautier (2013)[20].

achieved by imposing the derivative, but adjusting the temperature at the wall ($\Theta|_{int}$), in order to virtually ensure the target derivative value (Appendix A of Dairay Ph.D. thesis[8] has more details of the principle, accuracy, and convergence of the method). It means that a Dirichlet-type boundary condition (*DBC*) is applied to ensure a **Neumann-type boundary condition** (*NBC*).

In the *IBM* framework, the solid boundary does not always intercept a mesh node. In such case, $\Theta|_{int}$ is not prescribed at a mesh node, but it is indirectly defined by the interpolation required during the reconstruction.

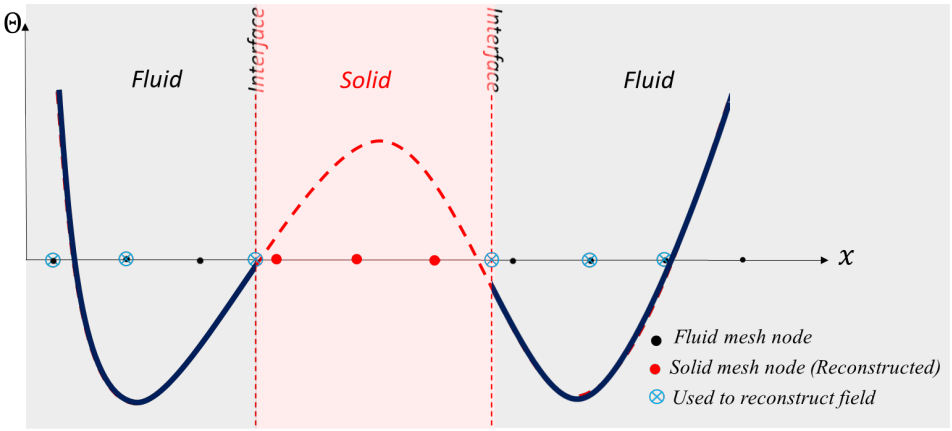

Figura 5.8: 1D Reconstruction scheme to represent solid by an Immersed Boundary Method. Case in which the variable in the fluid is reconstructed in the solid domain. This example uses 5^{th}-order Lagrange interpolating polynomials, which requires 6 points information.

At the computational domain boundary and the fluid/solid interface, it was applied a **3^{th}-order not centered scheme**. For the computational boundary with a uniform mesh spacing, the scheme reads

$$\frac{-11\Theta_1 + 18\Theta_2 - 9\Theta_3 + 2\Theta_4}{6\Delta x} = \left.\frac{\partial\Theta}{\partial x}\right|_{int}, \tag{5.48}$$

$$\frac{-11\Theta_{N_x} + 18\Theta_{N_x-1} - 9\Theta_{N_x-2} + 2\Theta_{N_x-3}}{6\Delta x} = \left.\frac{\partial\Theta}{\partial x}\right|_{int}. \tag{5.49}$$

At the **immersed boundary** the distance to the nearest fluid mesh node is not always the same, then the scheme is slightly modified, obtaining

$$a\,\Theta|_{int} + b\Theta_{i+1} + c\Theta_{i+2} + d\Theta_{i+3} = \left.\frac{\partial\Theta}{\partial x}\right|_{int} \Longrightarrow \Theta|_{int} = \frac{-b\Theta_{i+1} - c\Theta_{i+2} - d\Theta_{i+3} + \left.\frac{\partial\Theta}{\partial x}\right|_{int}}{a}, \tag{5.50}$$

where

$$a = -b - c - d,$$

$$b = \frac{1}{\Delta x_{int}} + \frac{\Delta x_{int} + \Delta x_1 + \Delta x_2}{\Delta x_1 \Delta x_2} - \frac{\Delta x_{int} + \Delta x_1}{\Delta x_2\,(\Delta x_1 + \Delta x_2)},$$

$$c = -\Delta x_{int}\frac{\Delta x_{int} + \Delta x_1 + \Delta x_2}{\Delta x_1 \Delta x_2(\Delta x_1 + \Delta x_2)},$$

$$d = \Delta x_{int}\frac{\Delta x_{int} + \Delta x_1}{\Delta x_2(\Delta x_{int} + \Delta x_1 + \Delta x_2)(\Delta x_1 + \Delta x_2)}.$$

In this work a two-fields approach is employed, in which the fluid and solid temperature field are stored in different computational variables. Figure 5.9 illustrates the reconstruction of the fluid temperature variable inside the solid domain. Equivalently, the solid temperature can be reconstructed inside the fluid domain. This and the derivative prescription at immersed boundary are new features implemented in *Incompact3d* to deal with the fluid-solid thermal (Real Conjugate Heat Transfer condition) coupling *via IBM*.

Heat flux imposition in complex geometries

When the heat flux has to be prescribed on the interface, the derivative imposition has to consider the local orientation of the interface. For the Cartesian mesh, this means that the heat

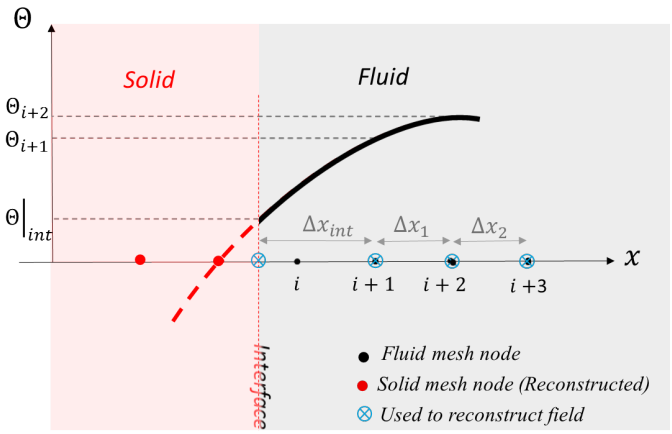

Figura 5.9: 1D reconstruction scheme to define the first derivative. Case used to prescribe a derivative in the fluid domain.

flux has to be projected in its Cartesian components, in order to apply the 1D reconstruction technique. Directional derivative gives two relations between the normal/tangential derivative and its Cartesian components. However, in 3D geometries, three relations are required to compute each Cartesian component of the heat flux. Thus, if it can not be taken any assumption about the tangential heat flux, there will not be enough equations for the problem closure.

The **conservation of energy** at the fluid-solid interface (Eq. 4.8), in Cartesian projections, can be expressed as

$$\left(\vec{\nabla}\Theta_s - \frac{1}{G_2}\vec{\nabla}\Theta\right)\Big|_{int} \cdot \vec{n} = 0. \tag{5.51}$$

two scenarios, in which Eq. 5.51 is satisfied, can be distinguish:

$$\left(\vec{\nabla}\Theta_s - \frac{1}{G_2}\vec{\nabla}\Theta\right)\Big|_{int} \cdot \vec{n} = 0 \Longleftrightarrow \begin{cases} (i): \quad \vec{\nabla}\Theta_s\Big|_{int} - \frac{1}{G_2}\vec{\nabla}\Theta\Big|_{int} = \vec{0} \\ or \\ (ii): \quad \left(\vec{\nabla}\Theta_s\Big|_{int} - \frac{1}{G_2}\vec{\nabla}\Theta\Big|_{int}\right) \perp \vec{n}. \end{cases} \tag{5.52}$$

The **temperature continuity** at the interface ($\Theta = \Theta_s$) requires that solid and fluid temperature gradients, tangential to the interface ($\vec{s} \perp \vec{n}$), be identical. From this consideration, it can be defined two scenarios:

$$\left(\vec{\nabla}\Theta_s - \vec{\nabla}\Theta\right)\Big|_{int} \cdot \vec{s} = 0 \Longrightarrow \begin{cases} (iii): \quad \vec{\nabla}\Theta_s\Big|_{int} - \vec{\nabla}\Theta\Big|_{int} = \vec{0} \\ \\ (iv): \quad \left(\vec{\nabla}\Theta_s\Big|_{int} - \vec{\nabla}\Theta\Big|_{int}\right) \perp \vec{s} \ (\parallel \vec{n}), \end{cases} \tag{5.53}$$

where $\vec{s} = [s_x \ s_y \ s_z]^T$ is a local unitary vector contained in the plane yz and tangential to the fluid/solid interface.

The combined scenario (i)+(iii), in Eq. 5.52 and 5.53, is only possible when the fluid and solid thermal conductivities are equals ($G_2 = 1$). In this scenario, the thermal gradients in the solid and fluid are parallels, and thereby the energy boundary condition can be decoupled into its Cartesian components as

$$\vec{\nabla}\Theta_s\Big|_{int} = \vec{\nabla}\Theta\Big|_{int} \longrightarrow \begin{cases} \dfrac{\partial\Theta_s}{\partial x}\Big|_{int} = \dfrac{\partial\Theta}{\partial x}\Big|_{int}, \\ \\ \dfrac{\partial\Theta_s}{\partial y}\Big|_{int} = \dfrac{\partial\Theta}{\partial y}\Big|_{int}. \end{cases} \tag{5.54}$$

which is desirable for the present 1D reconstruction technique.

The scenario (ii)+(iii), in Eq. 5.52 and 5.53, is not possible because, conversely to the condition (ii), condition (iii) requires that the solid and fluid temperature gradients be parallel. On the other hand, the combined scenarios (i)+(iv) and (ii)+(iv) are completely possible ($\forall\, G_2 > 0$), but the temperature gradients can not be decoupled and the equation system which must be verified is

$$\begin{aligned} \left(n_x\frac{\partial\Theta_s}{\partial x} + n_y\frac{\partial\Theta_s}{\partial y} + n_z\frac{\partial\Theta_s}{\partial z}\right)\Big|_{int} &= \frac{1}{G_2}\left(n_x\frac{\partial\Theta}{\partial x} + n_y\frac{\partial\Theta}{\partial y} + n_z\frac{\partial\Theta}{\partial z}\right)\Big|_{int}, \\ \left(s_x\frac{\partial\Theta_s}{\partial x} + s_y\frac{\partial\Theta_s}{\partial y} + s_z\frac{\partial\Theta_s}{\partial z}\right)\Big|_{int} &= \left(s_x\frac{\partial\Theta}{\partial x} + s_y\frac{\partial\Theta}{\partial y} + s_z\frac{\partial\Theta}{\partial z}\right)\Big|_{int}. \end{aligned} \tag{5.55}$$

where the second condition should be ensured by the temperature continuity condition. As this formulation requires gradients information in all directions, the combined scenarios which become in these conditions are not desirables neither for the 1D reconstruction technique nor the parallelization strategy.

However, for solid geometries with local normal vector $\vec{n}$ parallel to a Cartesian mesh direc-

tion (as channel flow), this restriction is bypassed. In **channel flow**, the Cartesian derivative, to respect the energy conservation at the interface, can be defined as

$$\left.\frac{\partial \Theta_s}{\partial y}\right|_{int} = \frac{1}{G_2}\left.\frac{\partial \Theta}{\partial y}\right|_{int}, \tag{5.56}$$

For **pipe flow** the system to be verified to ensure the conservation of energy trough the interface is

$$\begin{aligned}\left.\left(x\frac{\partial \Theta_s}{\partial x} + y\frac{\partial \Theta_s}{\partial y}\right)\right|_{int} &= \frac{1}{G_2}\left.\left(x\frac{\partial \Theta}{\partial x} + y\frac{\partial \Theta}{\partial y}\right)\right|_{int}, \\ \left.\left(y\frac{\partial \Theta_s}{\partial x} - x\frac{\partial \Theta_s}{\partial y}\right)\right|_{int} &= \left.\left(y\frac{\partial \Theta}{\partial x} - x\frac{\partial \Theta}{\partial y}\right)\right|_{int}.\end{aligned} \tag{5.57}$$

Hence, if the solid temperature gradients are known, the fluid temperature gradient in Cartesian coordinates can be computed through the previous relations and imposed at the interface trough our technique defined by Equation 5.50. **Remark:** ideal locally imposed conditions can be represented trough selecting conveniently the thermal properties, in order to obtain very high (*IF* condition) or very small (*IT* condition) activity ratio.

5.4 Fluid-solid thermal coupling

In order to economize computational time, an efficient weak coupling is adopted. It means, every time step the fluid dynamic equations (4.2 and 4.1) and the thermal equations (4.5 and 4.6) are solved sequentially, while a strong coupling solves the fluid and solid governing equations simultaneously by iterative procedure. In *DNS* or even in *LES* framework, a strong coupling is very restrictive due to the flow field has to be converged every time step, which increases substantially the computational time.

Although the explicit nature of the weak coupling can imply stability limitations, Giles (1997)[25] shows that this kind of thermal coupling can be more stable when a Dirichlet condition is applied in the fluid and a Neumann condition in the solid.

The coupling strategy presented in Flageul (2015)[17] is adapted in the next steps:

1. The fluid temperature at the interface is updated by the mean value of the precedent temperature at solid and fluid: $\Theta^{n+1} = 0.5\,(\Theta^n + \Theta_s^n)$. This step allows a small discontinuity in the temperature at the interface (Equation 4.7).

2. The temperature derivative $\left(\frac{\partial\Theta^{n+1}}{\partial\vec{n}}\right)$ is computed at the wall with information of the fluid domain (left side of Eq. 5.50).

3. The solid temperature at the interface is updated (right side of Eq. 5.50) in order to ensure the energy conservation at the wall (Eq. 4.8 and Eq. 4.9 for the domain boundary): $\frac{\partial\Theta_s^{n+1}}{\partial\vec{n}} = \frac{1}{G_2}\frac{\partial\Theta^{n+1}}{\partial\vec{n}}$.

5.5 Parallelization strategy

3D flow problems with a great number of mesh nodes are highly demanding in terms of computational processing time, particularly when the problem is solved sequentially in one computational core. The parallelization is the computational strategy whose objective is to reduce the processing time by distributing the same problem in many cores working simultaneously (in parallel). The most recent version of *Incompact3d* adopts the domain decomposition technique (Figure 5.10). The computational domain is decomposed in sub-domains (pencil), for which each core computes the discretized Navier-Stokes equations. As these equations have discrete derivative operators acting in three dimensions, when the domain decomposition is done in x-direction (Figure 5.10a), only the derivatives in x are computed. Then, information is swapped to y-pencil (Figure 5.10b) to compute the derivatives in y-direction (as analogously, it would be done for derivatives in z-direction: Figure 5.10c). Figure 5.11 displays the *Incompact3d* structure and the swap processes required in every time loop. The Message Passing Interface (*MPI*) standard allows swapping the information from one direction to the other. The parallelization strategy is supported by the 2DECOMP&FFT (`http://www.2decomp.org`) to generate the decomposition and compute the Fast Fourier Transform in the sub-domains. This kind of parallelism in pencils (so-called 2D domain decomposition) was implemented in *incompact3d* by Laizet & Li (2011)[50]. The strategy has shown high scalability since it has been used in solving great problems in up to $O(10^6)$ computational cores (Flageul, 2015[16]).

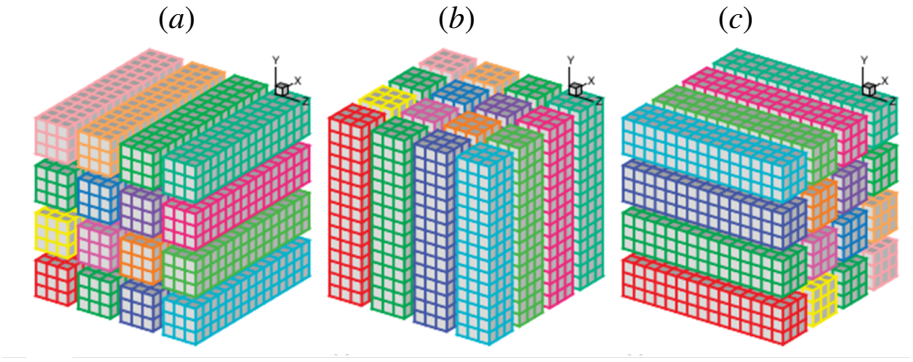

Figura 5.10: Domain decomposition in 4×4 MPI processes. (*a*): pencils in x-direction, (*b*): pencils in y-direction and (*c*): pencils in z-direction. Figure adapted from Laizet & Li (2011)[50]

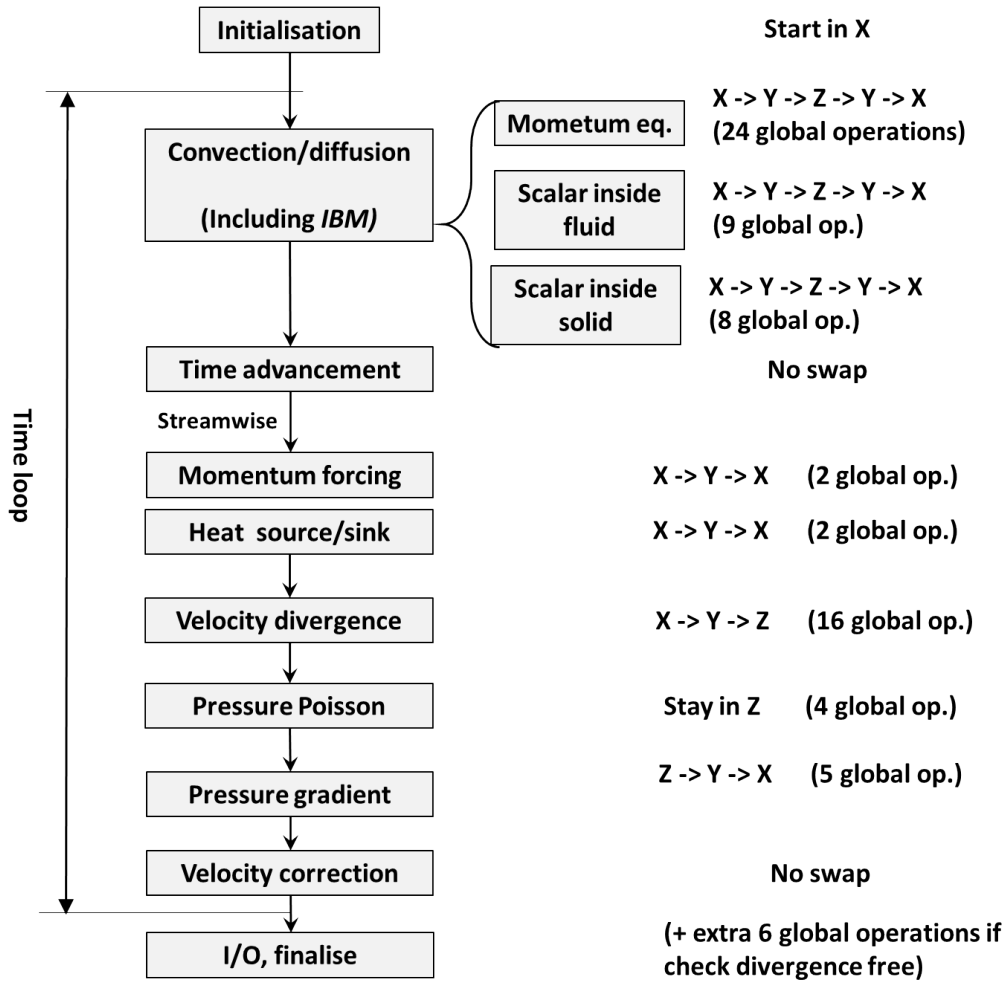

Figura 5.11: `Incompact3d` structure represented in one time step. On right side is shown the swap processes required by the 2D decomposition strategy. This is based on the main *Incompact3d* structure, adding the present implementations (Laizet e Li, 2011[50]).

The novel dual *IBM* developed in this thesis requires to solve the energy equation separately inside the fluid and the solid. Two computational fluid/solid temperature fields are employed, where the solid/fluid temperature exists all over the computational domain, but it is physically meaningful only in the corresponding domain. The fluid domain is the immersed region for the solid temperature and conversely for the fluid temperature solid. In practice, as Figure 5.11 shows, solving the energy equation requires nine global swap operation to compute the spatial derivatives in the fluid, eight additional global operations for the solid energy equation and four global operations to compute the streamwise momentum forcing and heat source/sink terms.

Chapter 6

Error analysis in laminar flow

The error analysis, described in this chapter, is based on velocity and temperature fields in the laminar solutions of channel/pipe flow, for ideal imposed uniform-constant heat flux (*IF*, Sec. 4.3.1), imposed non-uniform temperature (*IT*, Sec. 4.3.2) and the real conjugate heat transfer (*CHT*, Sec. 4.2). A rigorous and extensive analysis of the error sources, error order and spatial distribution, is presented. Pipe flow is only evaluated for the *IT* case, since a mathematical and numerical extra effort is required to solve the problem of imposing heat flux in a non-cartesian geometry, as the pipe geometry. However, at Subsection 5.3.2 some initial steps are presented in order to solve this problem.

The deviation of the numerical solution f from the exact solution f_e can be evaluated at every mesh node i (with the maximum absolute value equal to the norm L_∞) or estimated globally through the computation of the norm L_2. These error norms of the variable f are defined as

$$L_\infty[f] = max\left(\left|f_i - f_{e_i}\right|\right), \tag{6.1}$$

and

$$L_2[f] = \frac{1}{n}\sqrt{\sum_i (f_i - f_{e_i})^2} \tag{6.2}$$

where f_i is the numerical solution at the node i and n is the total number of nodes evaluated.

The error sources in the **velocity solution**, due to the discrete approximation, are:

1. the velocity and pressure decoupling by the projection method (not for laminar internal

flow, since wall-normal pressure gradient is null);

2. the computation of the convective term, velocity divergence, pressure gradient (first derivative);

3. the diffusive term computation (second derivative);

4. the time advancement error (temporal scheme);

5. the computation of the bulk velocity U_b, for correction of the streamwise pressure gradient every time step (spatial integration scheme).

As the temperature scalar field is passively transported by the flow, the **temperature solution** has the same error sources plus the errors associated to the numerical solution of the energy equation:

1. convective term computation (first derivative);

2. diffusive term computation (second derivative);

3. time advancement error ($O(\Delta t^3)$ for the fluid convective-diffusive equation; $\sim \Delta t^1$ for solid conduction equation);

4. computation of the bulk temperature Θ_b for correction of the streamwise temperature gradient every time step ($\sim \Delta x^4$ mean point integration scheme).

The error accuracy of a numerical scheme can be illustrated by a graph of an error norm (*e. g.* L_∞ and L_2) against a refinement or resolution parameter (η). In terms of the spatial resolution, for instance, two convenient options for η could be the mesh spacing (Δx) or its inverse (Δx^{-1}). If $\eta = \Delta x$, the error graph should follows an increasing potential law ($error = \eta^O$), conversely, if $\eta = \Delta x^{-1}$, the curve follows a decreasing potential law ($error = \eta^{-O}$), where the *error* is measured by an error norm (as L_∞ or L_2) and O is the accuracy order of the applied numerical scheme. This potential curve in a log-log scale is reduced to a linear curve with slope O or $-O$, as it is shown in Figure 6.1. For convenience at the present work, the refinement parameter is mainly selected as $\eta = \Delta x^{-1}$, since this illustrates the error decrement as the spatial refinement

increases. On the other hand, the spatial distribution of the error is analyzed for a normalized error profile/map, in order to compare different resolutions. The normalized profile/map of a function f is obtained by

$$f_{normalized} = \frac{|f - f_e|}{max\,|f - f_e|}. \tag{6.3}$$

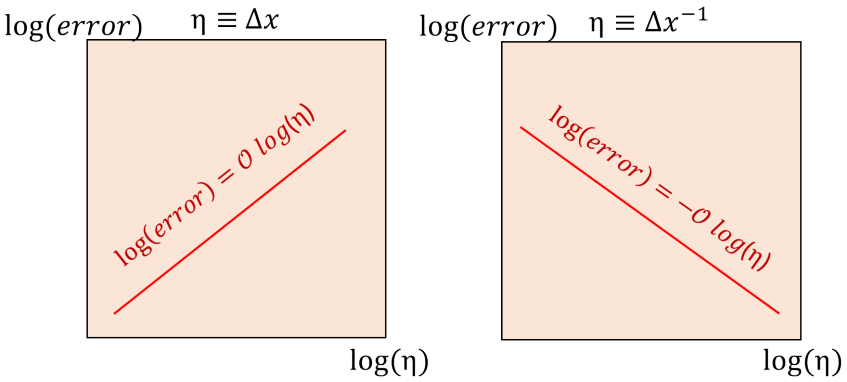

Figura 6.1: Error convergence illustration.

6.1 Error in channel configuration

6.1.1 Error in the fluid/solid interface location

When the interface coincides with mesh nodes, it is referred to as **collocated**, otherwise it is referred to as **staggered**. The magnitude of the error, in the fluid/solid interface location, is reduced by generating a highly refined sub-mesh $\Delta x_{ref} < \Delta x$ (where, $\Delta x_{ref} = \Delta x/m$ with $m \in \mathbb{Z}$). Then, when the fluid/solid interface does not coincide with a mesh node location, the error caused by the sub-mesh method is of the order of Δx^1, as Figure 6.2 shows. The channel flow is selected for this error evaluation, because the error of the interface location is the same over the entire interface (*e. i.* $L_\infty = L_2$).

Laminar solutions of velocity (Eq. 6.4) and temperature (Eq. 6.5 and 6.6) are polynomial functions of the distance from the wall y. As the lowest power of the polynomial solutions is $O(y^2)$, it is expected an error of $O(\Delta y^2)$ when the interface is not coinciding with mesh nodes, because the error in the interface location is $O(\Delta y)$.

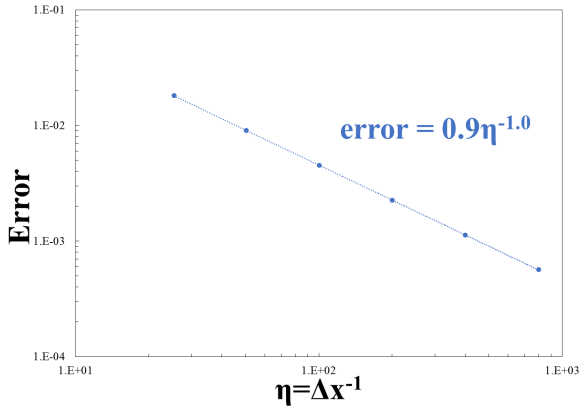

Figura 6.2: 1^{st}-order error in the *IB* location in channel geometry, when fluid/solid interface (wall) location is not collocated with mesh nodes, for $\Delta x_{ref} = \Delta x/10$. Using the sub-mesh method to reduce the error magnitude on the interface location.

6.1.2 Error in the derivatives computation

With no *IB* and using consistent periodical boundary conditions, the error on the spatial derivatives computation should be $O(\Delta x^6)$ all over the domain. When Dirichlet or Neumann boundary conditions are applied, the error is $O(\Delta x^3)$ at the computational boundary (see Tables 5.1-5.2, approximations 5.48-5.49 and annexe A of Dairay's thesis [8]). Conversely, when *IBM* is employed, the accuracy of the derivatives typically decreases at the fluid/solid interface, due to the numerical treatment given to the physical discontinuity imposed by the sudden medium change. The accuracy at the interface depends on the *IB* technique employed to overcome this discontinuity.

To establish the difference of accuracy between the cases with and without *IBM*, the error in computation of the first and second derivative is evaluated. Considering velocity and temperature analytical solutions for the laminar channel, the derivatives are numerically computed and compared to the analytical derivative, for several spatial resolutions. The analytical solutions for the velocity and temperature fields in the laminar **Poiseuille channel heated flow**, in $-H/2 \leq y \leq H/2$, are

$$u_x(y) = \frac{3}{2}\left(1 - 4y^2\right) U_b \quad , \quad u_y = u_z = 0, \tag{6.4}$$

$$\Theta(y) = \frac{Nu}{16}\left(5 - 24y^2 + 16y^4\right), \qquad \text{for } IT \tag{6.5}$$

$$\Theta(y) = \frac{1}{16}\left(5 - 24y^2 + 16y^4\right) - \frac{1}{Nu}, \qquad \text{for } IF/CHT \tag{6.6}$$

with $Nu = 140/34 \approx 4.118$ at any Reynolds and Prandtl numbers. When CHT is considered, the temperature profile inside the solid is linear

$$\Theta_s(y) = \frac{1}{G_2}\left(\frac{1}{2} - \frac{|y|}{H}\right) - \frac{1}{Nu}, \qquad \text{for } H/2 \leq |y| \leq L_y/2. \tag{6.7}$$

The temperature solution employed corresponds to the *IT* condition because, as it is shown at Section 4.3.4, this configuration enables using periodic computational domain for the scenario with *IBM*, without introducing error associated to the derivative imposition at the wall (conversely to *IF* and *CHT*). A different number of fluid nodes information ($npif$) is employed to reconstruct the solution in the immersed domain and establish its relation to the error convergence order. The error is computed for *collocated* and *staggered* interface, in order to define the difference.

The results of this analysis are shown in Figure 6.3, for collocated interface location. As expected, the greatest error is located at the immersed boundary (*IB*). The convergence order increases (up to 6^{th}-order) with an increasing number of information points used. This means that the error order of the derivation scheme is achieved at the immersed fluid-solid interface when the polynomial reconstructed is high enough. This is because a higher polynomial order has a higher continuous derivative, thus higher order terms are considered in the Taylor expansion of the solution around the interface (Linnick & Fasel, 2003[57]).

For staggered interface, Figure 6.4 shows the error in the computation of the first and second derivatives of velocity and temperature. the temperature and the velocity increases up to 3^{th} and 2^{nd}-order, respectively, with increasing information of fluid nodes. The interval in which this tendency is maintained is clearer and wider for the temperature than for the velocity, but, in practice, both converge with the same accuracy order for a high number of information nodes.

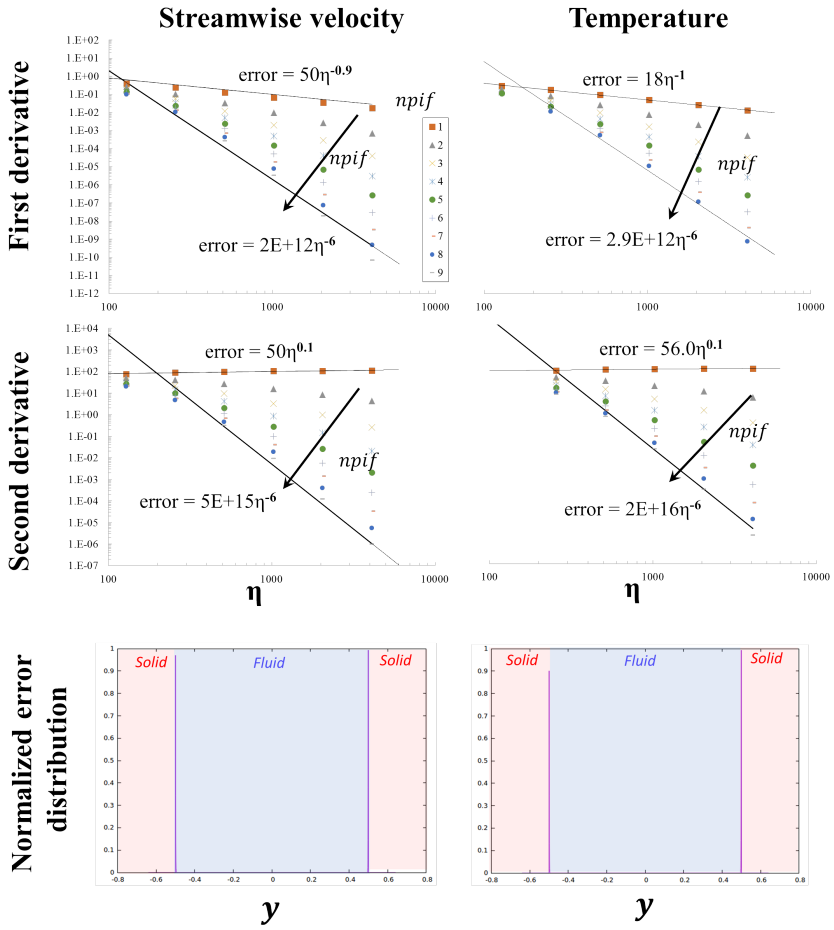

Figura 6.3: Error in the spatial derivatives computation of channel velocity and temperature laminar solutions, where *IBM* has been applied to represent the solid walls with different number of information nodes to each fluid side (*npif*). The immersed boundary is **collocated** with mesh nodes. The error distribution is practically the same for all the derivative estimations, and it shows twos clear peaks close to the wall while the error in the channel core is negligible, in comparison.

6.1.3 Error in the integration to compute bulk quantities - forcing/source term

The forcing term implementation requires to compute bulk quantities (Eq. 5.38), which are computed by applying a Simpson scheme. This scheme is 4^{th}-order accurate all over the integration domain. Besides, for a 1D-function f whose second derivative is null, the Simpson's scheme is exact. In practice, this means that, for laminar solution, the error in the bulk velocity computation is up to the machine accuracy (because $\partial^2 u_x/\partial y^2 = 0$).

Bulk quantity is used to compute the forcing/source term in the momentum/energy equation

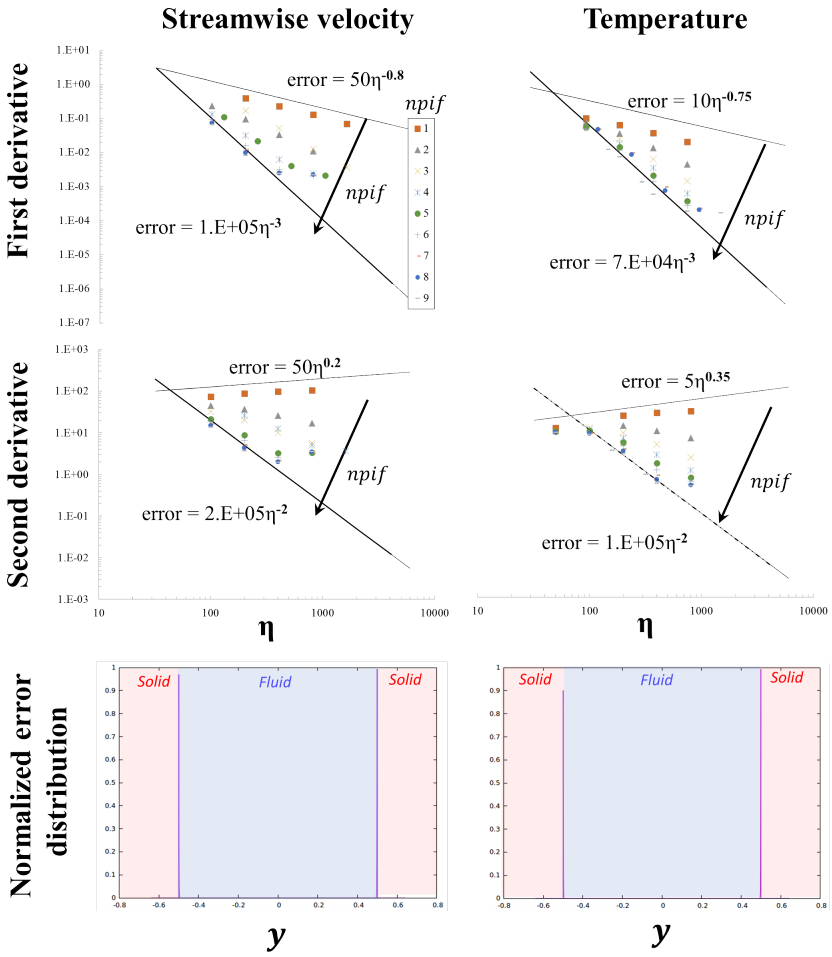

Figura 6.4: Error in the spatial derivatives computation of channel velocity/temperature laminar solution, where *IBM* has been applied to represent the solid walls with different number of information nodes to each fluid side ($npif$). The *IB* is **staggered** with mesh nodes. The error distribution is the same presented for the collocated case (Figure 6.3).

enabling to employ periodic streamwise domain. This source term could be implemented as a constant value or computed every time step to compensate the streamwise pressure/temperature gradient. The second alternative is attractive because allows the Nusselt number and friction Reynolds number estimation and that is the reason why, it is applied in this work.

6.1.4 Convergence to the laminar solution

In this section, the time evolution of the velocity and temperature, described by the governing equations, is considered. Although the laminar solution is not time-dependent, for any defined initial condition, the solver should be able to converge to an established flow, corres-

ponding to the steady laminar solution. Thus, for every simulation, it has been checked that the solution is fully established and converged in time, allowing to consider the numerical errors as only due to spatial discretization. However, aiming to minimize the transient stage during which the numerical solution has to adapt, the solutions (6.4, 6.5 and 6.6) are employed as initial conditions.

The analytical temperature and velocity solutions are compared with the corresponding numerical solution, in order to verify the code for *IF*/*IT* (both thermal conditions are physically equivalents in Poiseuille flow, Figure 4.2) and *CHT* thermal conditions.

The 3D version of the code *Incompact3D* is employed with arbitrary spanwise/streamwise domain size $L_x = L_z = 0.5$ and resolution $N_x = N_z = 10$, since the solution is independent on spanwise or streamwise directions. Table 6.1 shows the mesh resolution in normal-wall direction y, for the three thermal condition (*IT*, *IF* and *CHT*).

In the foregoing sections, the highest convergence order is reached by setting the number of fluid nodes used in the reconstruction to $npif$=9 (to each fluid side) and the employing collocated interface on the mesh nodes. Thus, the same parameters are adopted for following test of convergence to laminar solution. It should be pointed out that for *CHT* case, there are not the external buffer regions with still fluid and thereby the information nodes used corresponds to the closer nodes to the opposite wall.

Tabela 6.1: Spatial resolution N_y and domain size L_y of simulations, for verification of heat transfer in Poiseuille Chanel Flow[a] over locally imposed temperature (*IT*)[b], locally imposed heat flux (*IF*) and conjugate heat transfer (*CHT*) thermal boundary conditions (*TBC*).

TBC	N_y	L_y	$\Delta y \times 10^{-3}$	G_2
IT/IF	(128, 256, 512, 1024, 2048)	1.28	(20, 10, 5, 2.5, 1.25, 0.625)	–
CHT	(201, 401, 801, 1001, 2001)	2	(20, 10, 5, 2.5, 1.25, 0.625)	(1, 2, 4)

[a] Neither the velocity or the temperature solutions depend on *Re* or *Pr*.

[b] *IF* and *IT* are physically equivalents in Poiseuille flow (none velocity/temperature temporal fluctuation).

The present implementation of dual *IBM*, for the *CHT* case, consists in representing the solid temperature and the fluid temperature by *two* temperature fields. This very useful capability enables to simulate scenarios with different fluid-to-solid ratios of the conductivity ($G_2 = \lambda_s/\lambda$), having, at the interface, a sharp transition of the physical meaningful temperatures but even continuous derivatives (Figure 6.5).

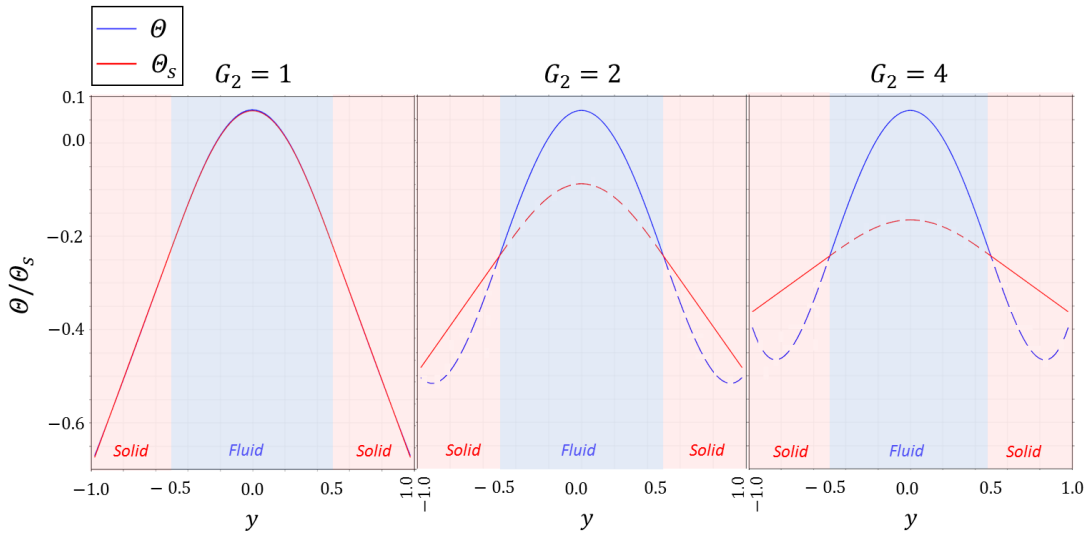

Figura 6.5: Temperature profiles at the fluid-solid interface for different conductivity ratios ($G_2 = \lambda_s/\lambda$).

As expected, the velocity has a 6^{th}-order of convergence when the computational boundary domain can be considered as periodic in the normal-wall direction (top of Figure 4.3), corresponding to the thermal configurations *IT* and *IF* (Figure 6.6). Whereas, for *CHT*, the computational domain has to be considered with Dirichlet-type boundary condition and thereby the convergence order is reduced to 2^{nd}-order. In practice, 6^{th}-order convergence is obtained for the Nusselt number and the temperature for *IT* (Figures 6.7 and 6.8), while, for the more demanding configurations *IF* and *CHT*, only 2^{nd}-order is reached for the temperature.

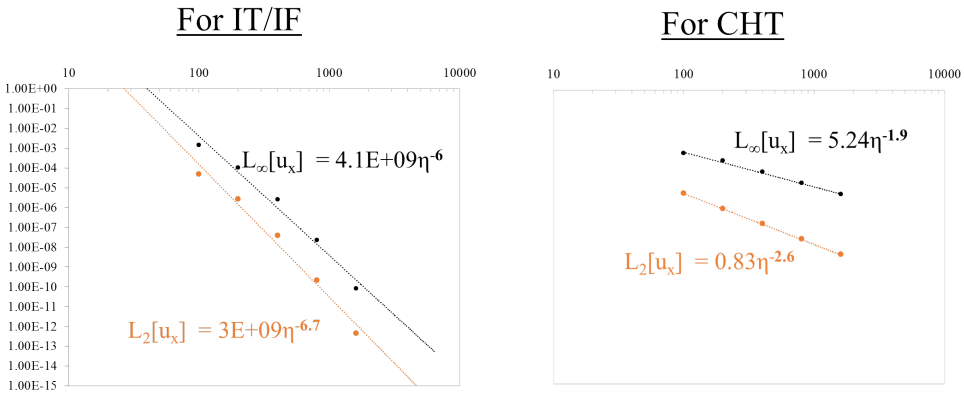

Figura 6.6: Velocity convergence using interface collocated on mesh nodes and nine information fluid nodes, to each side of the *IB*, to reconstruct the solution in the immersed region. As the computational domain is not periodic in the wall-normal direction, for *CHT*, the velocity convergence order is reduced.

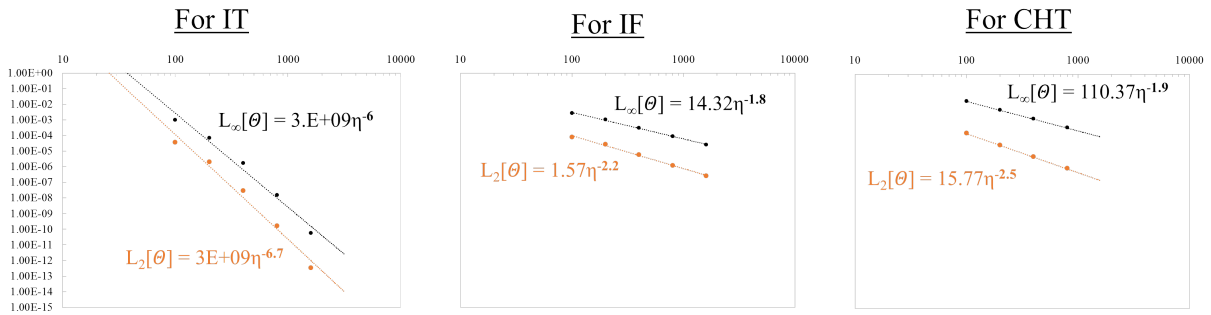

Figura 6.7: Temperature convergence in laminar channel, considering interface collocated on mesh nodes, *IT/IF/CHT* thermal conditions and nine fluid points of information for the reconstruction of the solution inside the immersed region ($npif = 9$).

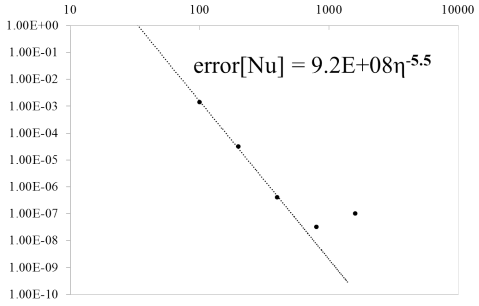

Figura 6.8: Nusselt number convergence for *IT*. Computed from the source term f_Θ.

6.2 Error in pipe configuration

Conversely to the channel, the pipe is a 2D geometry, then the **interface location** relative to the nodes changes along with the interface. This means that the pipe solid wall cannot be collocated with mesh nodes everywhere, thus the error in the interface location and its influence on the solution have to be accepted.

Here, the code verification is carried out for *IT* thermal conditions (equivalent to *IF*). In laminar Poiseuille flow, the analytical solution of the velocity profile is

$$u_x(r) = 2\left(1 - 4r^2\right) U_b, \quad u_\theta = u_r = 0. \tag{6.8}$$

where r is the radial coordinate, u_θ and u_r are the azimuthal and radial velocities, respectively.

Incropera [32] deduced the following temperature profile, for *IF/IT*:

$$T(r,x) = T|_{int}(x) - \frac{U_b D}{2\alpha}\left(\frac{dT_b}{dx}\right)\left[\frac{3}{16} + r^4 - r^2\right], \tag{6.9}$$

Then, changing variable to $\Theta = (T|_{int} - T)/(T|_{int} - T_b)$, the dimensionless temperature solution is

$$\Theta(r) = 2Nu\left[\frac{3}{16} + r^4 - r^2\right] \quad with \quad Nu = -\left.\frac{\partial\Theta}{\partial r}\right|_{int} = 4.36. \tag{6.10}$$

It is important to stress that $\Theta(r)$ does not depends on Re, Pr nor x.

All the simulations were initialized with the analytical solution (Equations 6.8 and 6.10). The error on the computation of the derivatives is analyzed while evaluating the quality of the solution in terms of:

- procedure to apply the thermal source term f_Θ;
- proximity of the *IB* to the computational boundary (orientation of the *IB* relative to the Cartesian mesh);
- exact velocity field or solved velocity field.

Similar to the channel laminar simulations, pipe flow solution does not depend on the streamwise coordinate, thus the size and the resolution in this direction are arbitrarily adopted as $(L_x,\ N_x) = (0.5,\ 10)$. Table 6.2 shows the transversal resolution $L_y/N_y = L_z/N_z$ for three domain sizes, where the two highest are only used to evaluate the domain size influence.

Tabela 6.2: Parameters of simulations for verification of heat transfer in Poiseuille Pipe Flow and *IF/IT* thermal boundary condition.

$N_y = N_z$	$L_y = L_z$	$\Delta y = \Delta z \left(\times 10^{-3}\right)$
(32, 64, 128, 256)	1.28	(40, 20, 10, 5)
(44, 88, 176, 362)	1.76	(40, 20, 10, 5)
(64, 128, 256, 512)	2.56	(40, 20, 10, 5)

6.2.1 Error in the derivatives computation

In addition to the solution quality, the error on the computation of the spatial derivatives is first analyzed (as it was done in Subsection 6.1.2, for channel flow). As the pipe geometry imposes a restriction of staggered *IB* relative to the mesh nodes, the expected maximum error on the derivatives is of 2^{nd}-order. The derivatives normalized error distribution on the pipe cross-sectional area (Eq. 6.3), for various resolutions, is presented in Figure 6.9. The first derivative shows sensibility to the orientation of the *IB* relative to the mesh orientation, in such way that the error in the first-derivative in z is concentrated at the left and right sides of the pipe, while the first-derivative error in y tends to concentrate at the top and bottom of the pipe sectional-area. Besides, the first-derivative in x shows some error fluctuations for the lowest resolution and these fluctuations can be associated with the very poor resolution of this test. On the other hand, the second-derivate error is more homogeneously distributed on the pipe section, excepting some points near the wall with apparently uniform azimuthal spacing. Again, the second-derivative in x only shows error for the poorest resolution.

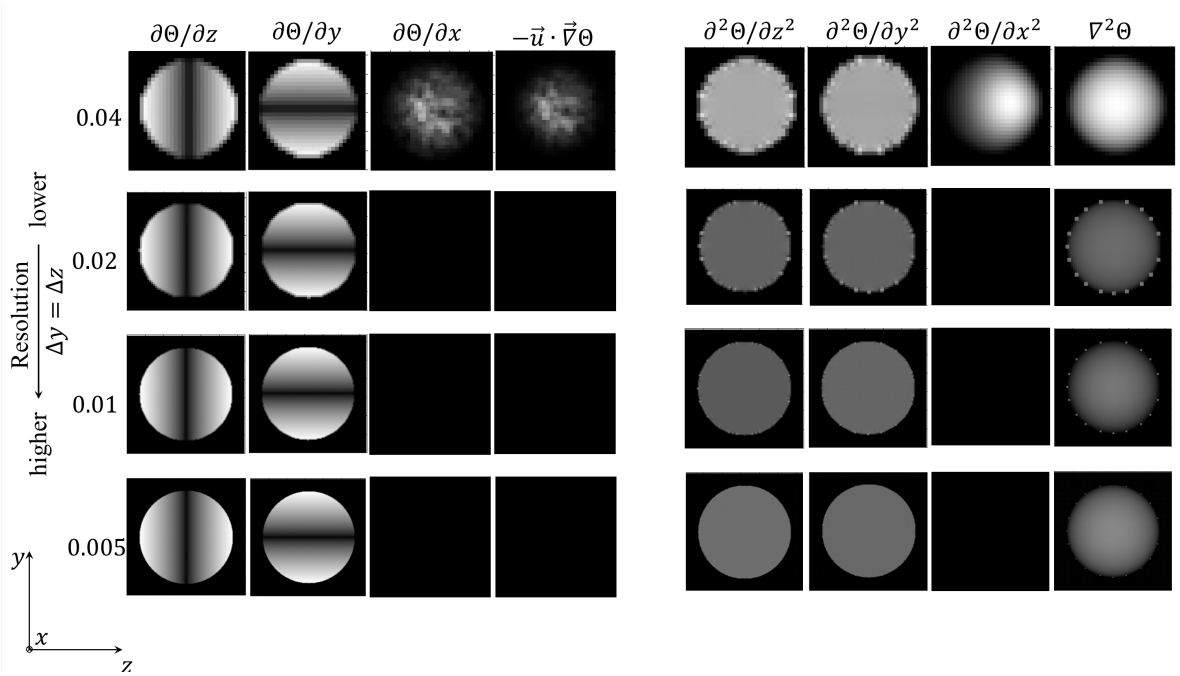

Figura 6.9: Normalized error maps of the first/second derivative and the convective/diffusive term, for different spatial resolutions. The error is normalized by the maximum error, then white tones illustrate the highest errors and the black tones the lowest ones.

6.2.2 Influence of the source term

At subsection, it already is considered time advancement of the variables of interest. The differences between the bulk temperature adjustment and the constant source term are discussed, in terms of the quality of the numerical solutions, time per iteration and error spatial distribution (Figures 6.10 and 6.11). As a 2^{nd}-order accuracy is expected (Subsection 6.1.1), for simplicity, the bulk quantities (employed in the Θ_b adjustment procedure) are computed by rectangle integration method, corresponding to 3^{th}-order accuracy, when the *mid point* is used.

The error in Θ, when Θ_b is adjusted, is higher for almost all the resolutions, but the convergence order (2^{nd}-order) is similar or even higher than the case of constant f_Θ.

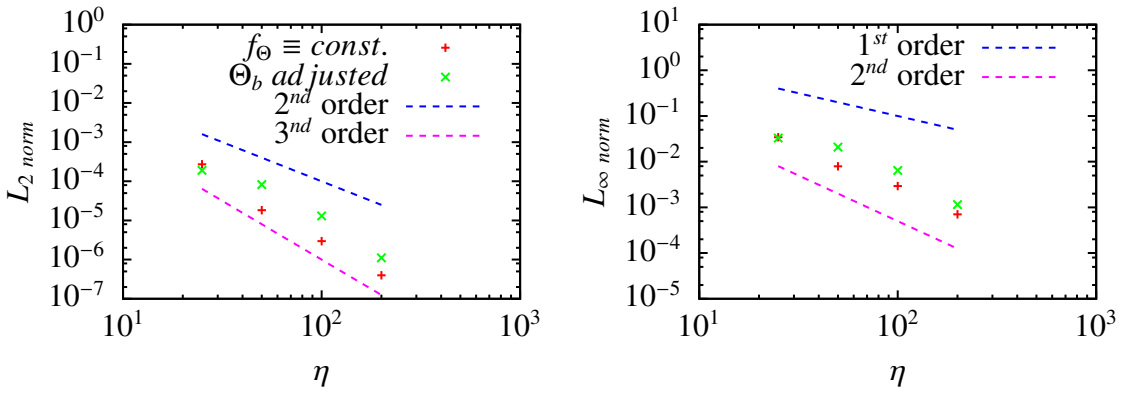

Figura 6.10: Convergence of Θ for two imposition procedures of f_Θ.

The results do not show considerable differences in term of time per iteration (Figure 6.11), however the error distribution changes (Figure 6.12). When $f_\Theta = const.$ the high errors are mainly concentrated near the immersed boundary, while for the case Θ_b adjusted ($f_\Theta = variable$), an error appears on the center of the pipe sectional-area. This variation on the error distribution is due to integration error in computing Θ_b. Furthermore, the error maps show an azimuthal distributed pattern with a cross-shape at regions which are closer to the computational domain boundary.

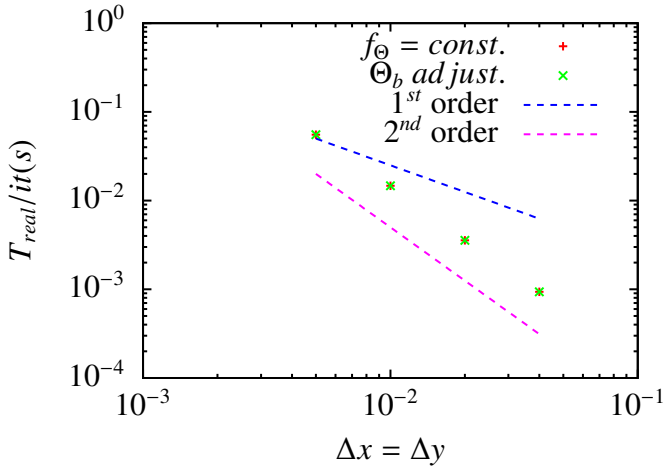

Figura 6.11: Real simulation time per iteration (T_{real}/it) estimated for two different procedures to impose the source term.

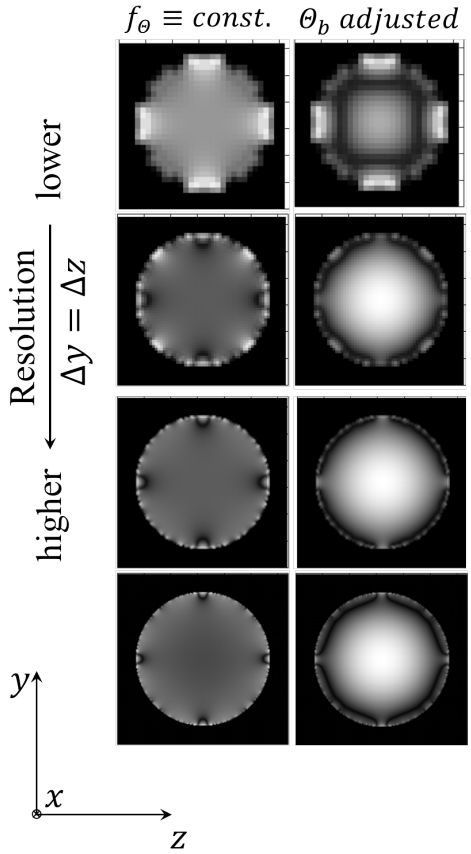

Figura 6.12: Normalized error maps of temperature Θ, for different imposition procedures of the source term. White tones illustrate the highest errors and the black tones the lowest ones.

The main advantage of adjusting the temperature is the capability to compute the Nusselt number, which also shows second order of convergence (Figure 6.13).

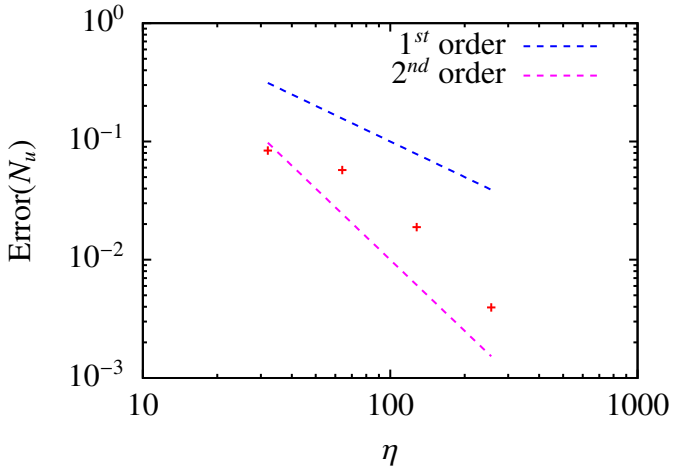

Figura 6.13: Nusselt number convergence.

6.2.3 Computational boundary proximity

Starting from the assumption that the proximity of the *IB* to the computational boundary defines the error pattern, the convergence order is evaluated for three domain sizes (Table 6.2). The convergence order does not show significant differences and the spatial error pattern is maintained and only intensified with increasing computational domain size (Figures 6.14 and 6.15). Therefore, it could be conclude that this pattern is associated with the *IB* orientation relative to the mesh and it is slightly influenced by the domain size.

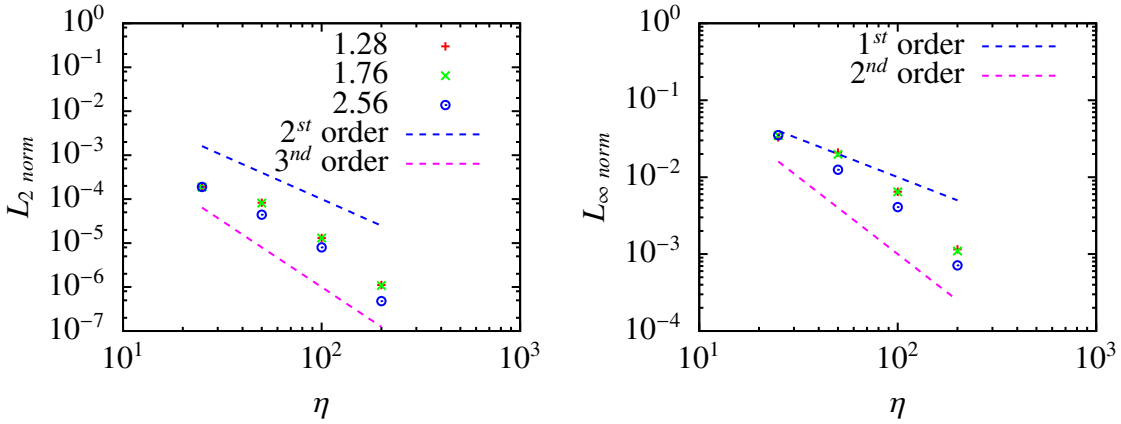

Figura 6.14: Convergence of Θ for different domain sizes $L_y \times L_z = 1.28 \times 1.28$; 1.76×1.76; 2.56×2.56.

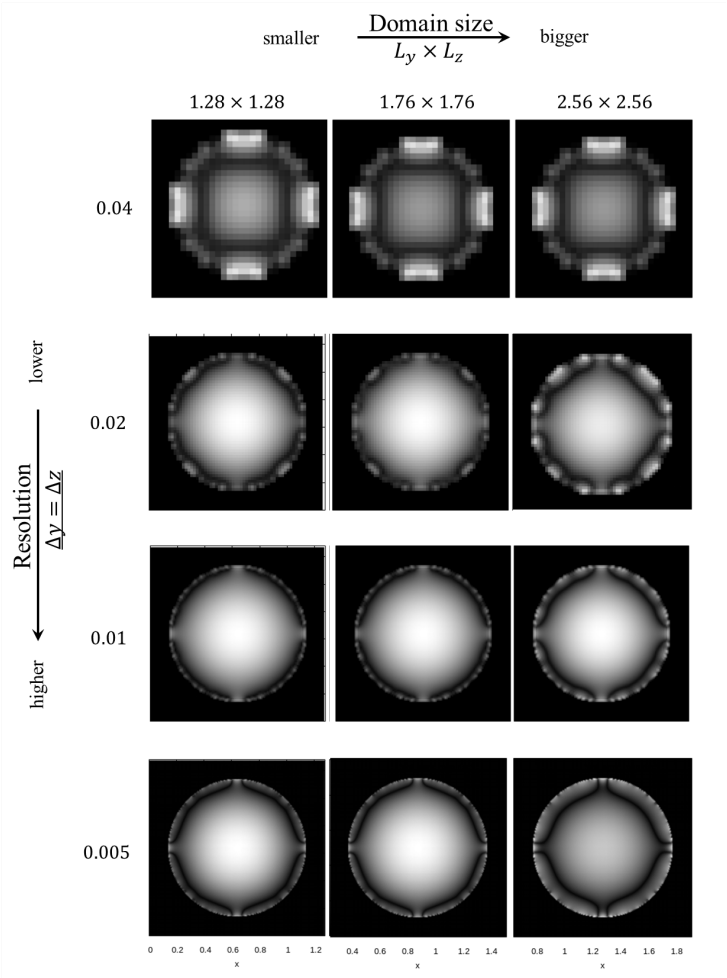

Figura 6.15: Normalized error maps of temperature Θ, for different spatial resolutions and domain sizes.

6.2.4 Influence of the velocity solver

In this subsection the convergence error is compared between the case in which the velocity solver is employed against the case in which the velocity analytical solution is applied (no velocity error). When the temperature transport equation is solved in couple with the momentum and continuity equations, the convergence analysis shows a wide influence of the velocity solver on the temperature solution (Figure 6.16). When velocity solver is employed, the convergence curve of the velocity and temperature has the same behavior and convergence order (first row of Figure 6.16). In both cases, the norm $L_{2\ norm}$ shows higher than 2^{nd}-order of convergence, but the maximum error (L_∞) is up to 2^{nd}-order of accuracy. When the velocity analytical solution is adopted instead of using the velocity solver, the convergence curve (slope) is more uniform and the magnitude of the error is lower, however, the error convergence is of 2^{nd}-order (second row

of Figure 6.16).

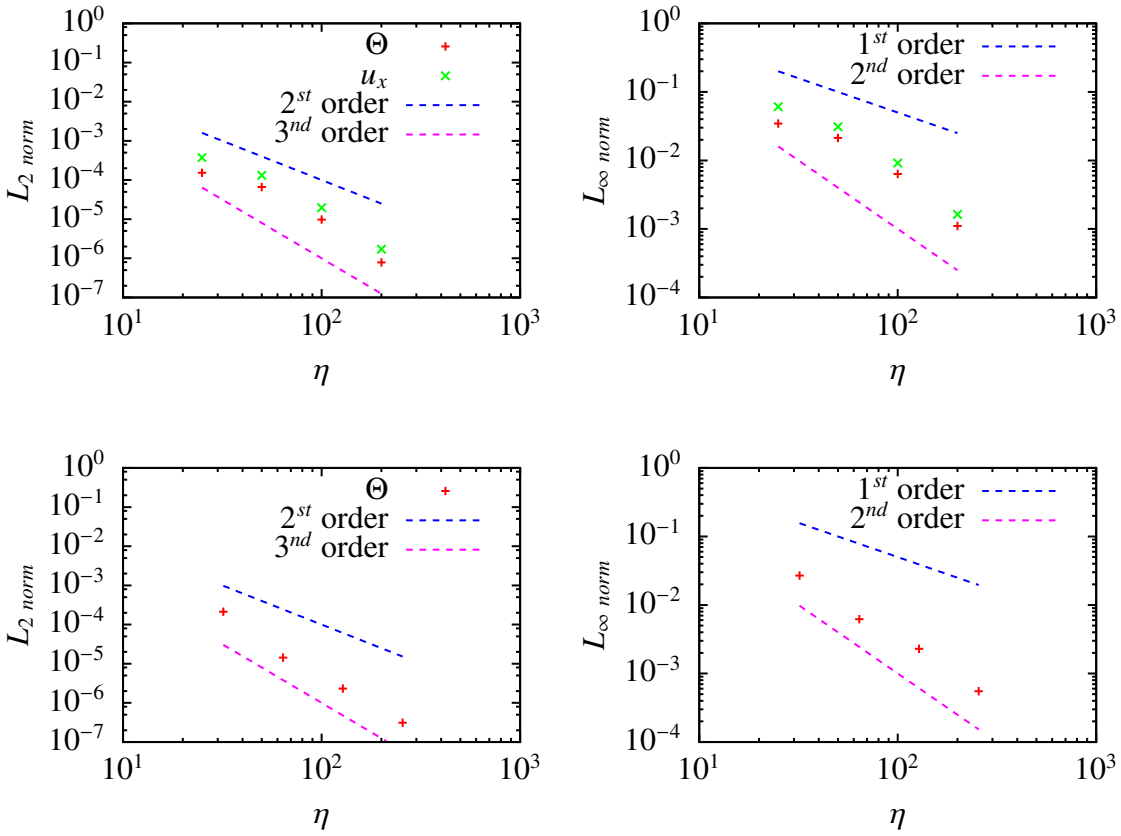

Figura 6.16: Convergence of Θ and u_x. First raw: applying **Velocity solver**; second row: assuming **analytical velocity field**.

6.3 Concluding remarks

At the foregoing sections, the code is verified for laminar channel and pipe flow. The channel flow is evaluated for three thermal boundary conditions at the *IB*, while the pipe flow is evaluated only for *IT* boundary condition. The main remarks of the results are listed below. By the present source term imposition, the Nusselt number can be accurately computed either in channel or in pipe plow.

In channel flow

- The convergence order increases with increasing order of the polynomial reconstructed inside the immersed region (increasing the polynomial order implies to increase the number of fluid nodes information).

- When consistent periodic boundary conditions on the computation domain can be impo-

sed (*IT* condition) and the *IB* is collocated on mesh nodes, up to 6^{th}-order accuracy is reached.

- Up to 2^{nd}-order of convergence is reached for *IF* and *CHT* (since imposed heat flux is required).

- Due to the error in the interface location is $O(\Delta y)$, in staggered interfaces location, it is expected an error of $O(\Delta y^2)$ in the velocity/temperature polynomial solutions (corresponding to polynomials of lowest 2^{nd}-order power).

- As the velocity/temperature analytical solution is a $2^{nd}/4^{th}$-order polynomial function of the distance to the *IB* location, when the *IB* is not collocated with mesh node, the *IB* location error is $\sim \Delta x^1$ and thereby the lowest polynomial (velocity solution) will impose the convergence order corresponding to 2^{nd}-order.

- The dual *IBM*, for the *CHT* case, allows simulating scenarios with different fluid-to-solid conductivity ratios (G_2) by efficiently representing the sudden medium transition and even maintaining continuous derivatives.

In pipe flow

- The distribution of the first-derivative error strongly depends on the direction in which the derivative is computed, while the second-derivative error distributes almost homogeneously with some peaks near the *IB*.

- The main influence of the procedure to impose the energy (temperature) source term is identified on the error distribution, which has a local peak at the pipe center when Θ_b is adjusted, conversely to the case $f_\Theta = const$.

- It was found that the pattern of error distribution is not only associated to the domain size but it strongly depends on the orientation of the *IB* interface relative to the mesh.

- As the velocity drives the temperature error, even using the exact velocity solution throughout the simulation, the 2^{nd}-order convergence of the maximum error is preserved.

On the other hand, the norm L_2 shows higher error, since it considers error located in the pipe core far from the *IB*.

Chapter 7

Turbulent flow

This chapter focuses on the presentation and discussion of the basic turbulent quantities (as profiles of mean streamwise velocity, Reynolds stresses, mean temperature, temperature fluctuations and streamwise turbulent heat flux) compared to *DNS* reference results obtained by techniques without *IBM*. This is carried out for three thermal boundary conditions (*IT/IF/CHT*) in channel flow, while the *IT* case is studied in pipe flow.

Table 7.1 shows the platforms used to perform the simulations, where the `Galileu` platform is mainly employed for laminar simulations (Chap. 6), while `LoboC` and `Curie` supercomputers were employed for the more demanding turbulent simulations. Finally, it should be stressed that the pipe flow is not analyzed for *IF* or *CHT* conditions.

Tabela 7.1: Characteristics of the high performance computers employed.

Platform (station)	*Processor*	*Speed (GHz)*	*Computational cores*	*RAM*
`Galileu`	Intel core i7	3.3	12	$32Gb$
`LoboC`	Intel Xeon	2.7	6048	$2.7Gb/core$
`Curie`	Intel SandyBridge	2.7	80640	$4Gb/core$

7.1 Validations of turbulent channel flow

Turbulent results were validated by comparing with the *DNS* works of Flageul *et al.* (2015[17], 2017[18]), since in those works the same 6^{th}-order compact schemes are employed. Further-

more, Flageul *et al.* do not use any *IBM*, discretize the solid domain in a Chebyshev mesh and the fluid domain in a stretched mesh (highly refined at near wall region) while computing implicitly the second derivatives in y-direction. This last allows using short computational time step and refined mesh to represent the thermal sublayer. For this purpose, our simulation were performed employing the same parameters of Flageul (Tables 7.2 and 7.3). However, our uniform mesh spacing requires to use a higher number of nodes. It should be stressed that the reference works of Flageul were deeply validated with the spectral *DNS* works of Kasagi *et al.* (1992)[36] and Tiselj *et al.* (2001a)[97], whose parameters and the present simulation parameters are also presented in Table 7.3.

Tabela 7.2: Main simulation parameters, for turbulent cases. Thermal boundary conditions (*TBC*): imposed temperature (*IT*), imposed heat flux (*IF*), conjugate heat transfer (*CHT*). Time step set to $\Delta t = 0.003$.

TBC	*Re*	*Pr*	$N_x \times N_y \times N_z$	$L_x \times L_y \times L_z$
IT	4560	0.71	$256 \times 256 \times 256$	$12.8 \times 1.28 \times 4.26$
IF	4560	0.71	$256 \times 256 \times 256$	$12.8 \times 1.28 \times 4.26$
CHT	4560	0.71	$256 \times 401 \times 256$	$12.8 \times 2 \times 4.26$

Tabela 7.3: Simulation parameters in wall-units compared to the reference ones.

Quantity	Current work	Flaguel *et al.*, 2015[17]	Kasagi *et al.*, 1992[36]	Tiselj *et al.*, 2001[97]
$\langle Re_\tau \rangle$	148	149	150	150
$Re'_{\tau\ rms}$	0.77	–	–	–
Pr	0.71	0.71	0.71	0.71
$\langle N_u \rangle$	15.1[a]	–	–	–
$N'_{u\ rms}$	0.27[a]	–	–	–
$\left[L_x^+,\ L_y^+,\ L_z^+\right]$	$[3789,\ 296, 1259]$	$[3814,\ 298, 1269]$	$[2356,\ 300, 942]$	$[2356,\ 300, 471]$
Δy^+	1.5	$[0.49; 4.8]$	$[0.08; 4.9]$	$[0.08; 4.9]$
$[\Delta x^+, \Delta z^+]$	$[14.8,\ 4.9]$	$[14.8,\ 4.9]$	$[14.8,\ 7.4]$	18.4
Δt^+	0.03	0.02	0.12	0.12
Duration	2900	29000	2100	6000
Scheme	Compact+*IBM*	Compact	Spectral	

[a] One classical and widely applied correlation, valid for smooth tubes over a large Reynolds number range including the transition region, is provided by Gnielinski (1976)[27]. At $Re = 4560$, Gnielinski's correlation estimates $\langle Nu \rangle = 15.76$, corresponding to about 4% of deviation from the present estimation.

In order to develop and establish a turbulent state, a simulation is performed at $Re = 19000$, employing uniform unitary velocity with white noise and temperature laminar solution as initial conditions. After obtaining an established turbulent state, the velocity/temperature fields

yielded are used as the initial condition for the simulations at $Re = 4560$. A turbulent simulation is considered as fully established when the time histories of Re_τ and Nu are statistically stationaries (Figure 7.1). For $Re = 4560$, Gnielinski's correlation estimates $\langle Nu \rangle = 15.76$, corresponding to about 4% of deviation from the present estimation. The friction Reynolds number Re_τ is underestimated in 0.7% in relation to Flageul (2015)[17], while the mean velocity and the Reynolds stresses profiles have a good agreement (Figures 7.1 and 7.2). The deviation from the reference values is associated with the low normal-wall resolution (Δy^+) at near-wall, which is three times lower than the used by Flageul.

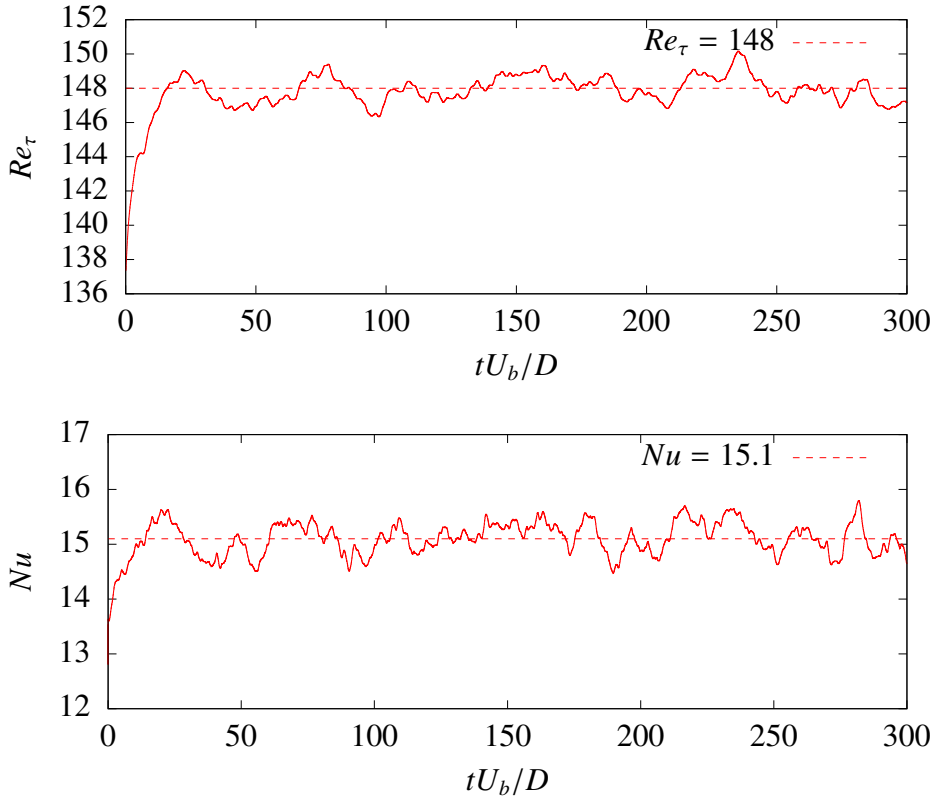

Figura 7.1: Time history of $Re_\tau = \dfrac{u_\tau(H/2)}{\nu}$ and $Nu = \dfrac{hH}{\lambda}$.

In the next sections, the present turbulent statistics are evaluated for channel and three thermal boundary conditions (*IT/IF/CHT*). For the velocity and temperature fields, basic statistics were evaluated, corresponding to spanwise-averaged profiles of mean velocity $\langle u_x \rangle^+$, Reynolds stresses $\langle u_i u_j \rangle^+$, mean temperature $\langle \Theta \rangle^+$, temperature fluctuations Θ^+_{rms} and turbulent heat flux $\langle u_x \Theta \rangle^+$.

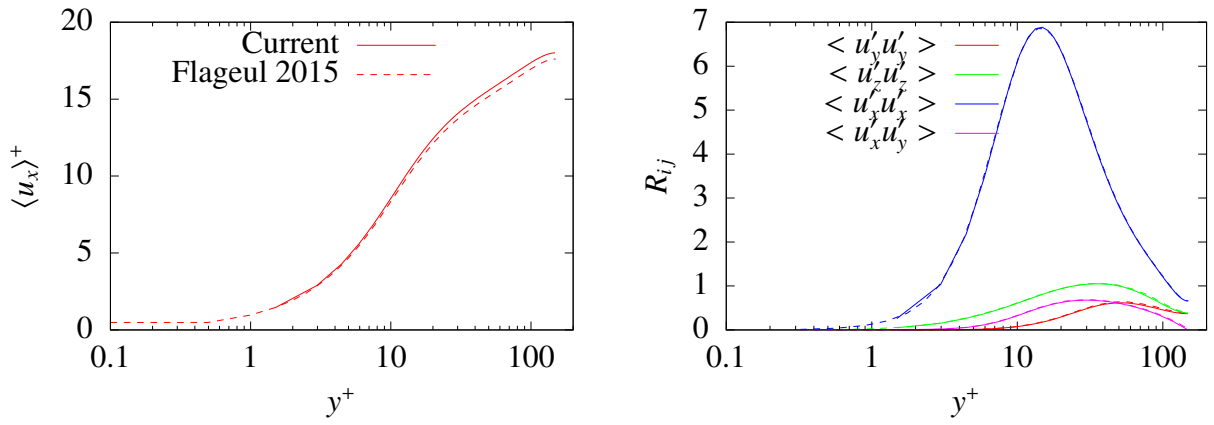

Figura 7.2: Current velocity statistics in channel flow (continuous line) compared to Flageul 2015 [17] (dashed line), for $Re = 4560$ ($Re_\tau \approx 150$). Left: Mean streamwise velocity profile $\langle u_x \rangle^+$. Right: Reynolds stresses profiles $R_{ij} = \left\langle u'_i u'_j \right\rangle$.

7.1.1 *IT* and *IF* in channel flow

For *IT* and *IF* cases, the temperature statistics have an excellent agreement (Figures 7.3 and 7.4), excepting the temperature *rms*, in *IF* case, which is slightly overestimated up to 5% at near-wall region, for $y^+ < 10$. As Flageul *et al.* use near-wall refinement, conversely to the present uniform mesh spacing, Flageul *et al.* mesh resolution is higher at the near-wall and lower in the channel center, in comparison with the present resolution (Table 7.3). Considering the variation between Flageul *et al.* methodology and the present approach, in future works our results could be even improved by increasing the number of nodes in $y-$direction, using near-wall stretching, prescribing the heat flux at the interface with a higher order numerical scheme, or/and modifying the *IBM* reconstruction strategy (*e. g.* reconstruct the solution in the immersed region by cubics splines or Hermite polynomials, for instance).

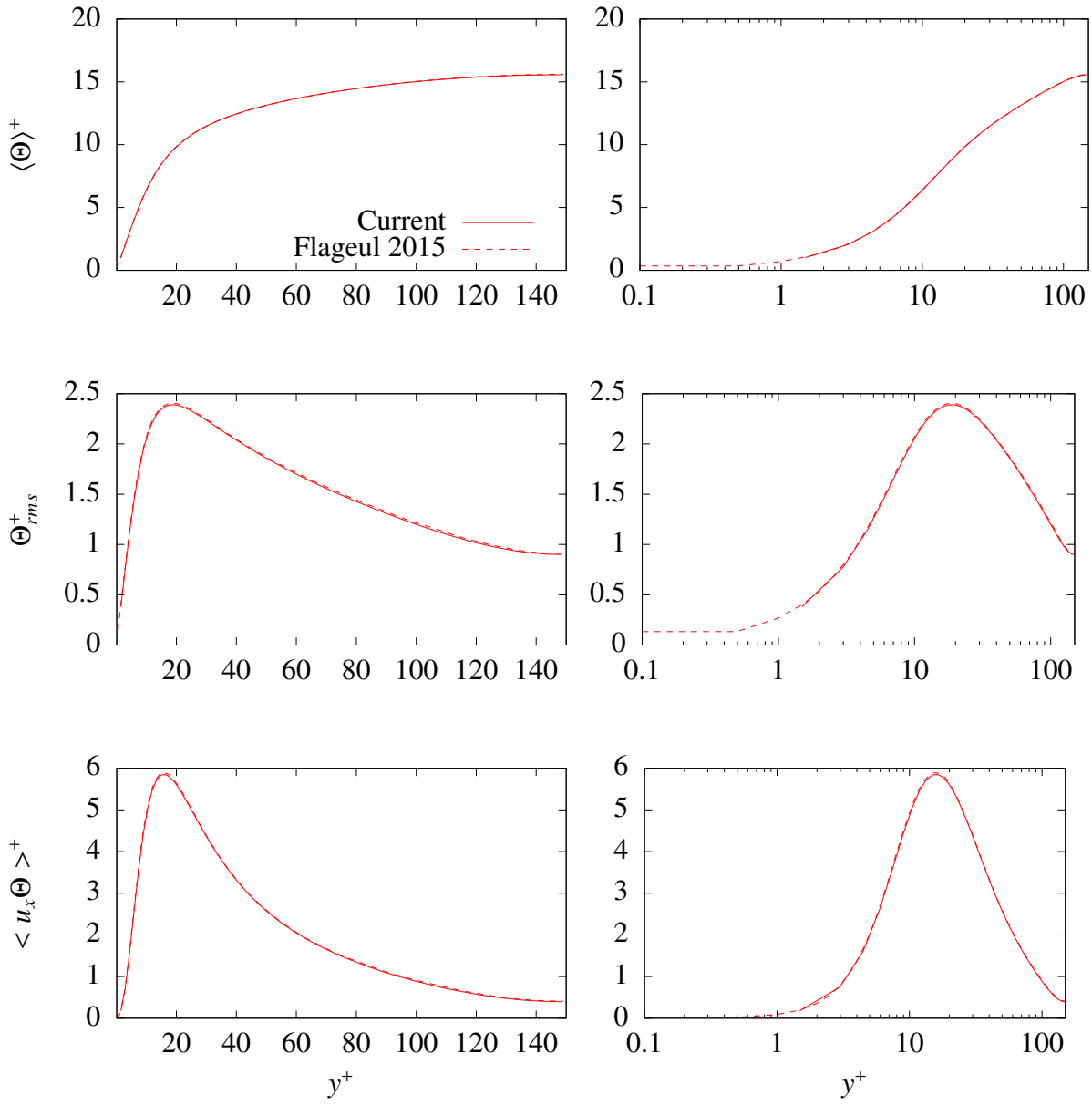

Figura 7.3: Temperature statistics in channel flow (continuous line) compared to Flageul, 2015[17] (dashed line), for *locally imposed non-uniform temperature* (*IT*). Top row: Mean temperature profile $\langle\Theta\rangle^+$. Center row: Temperature root mean square profile Θ^+_{rms}. Bottom row: Turbulent heat flux profile $\langle u'_x\Theta'\rangle^+$. At the Left/right column the wall-distance axis y^+ is in linear/logarithmic scale.

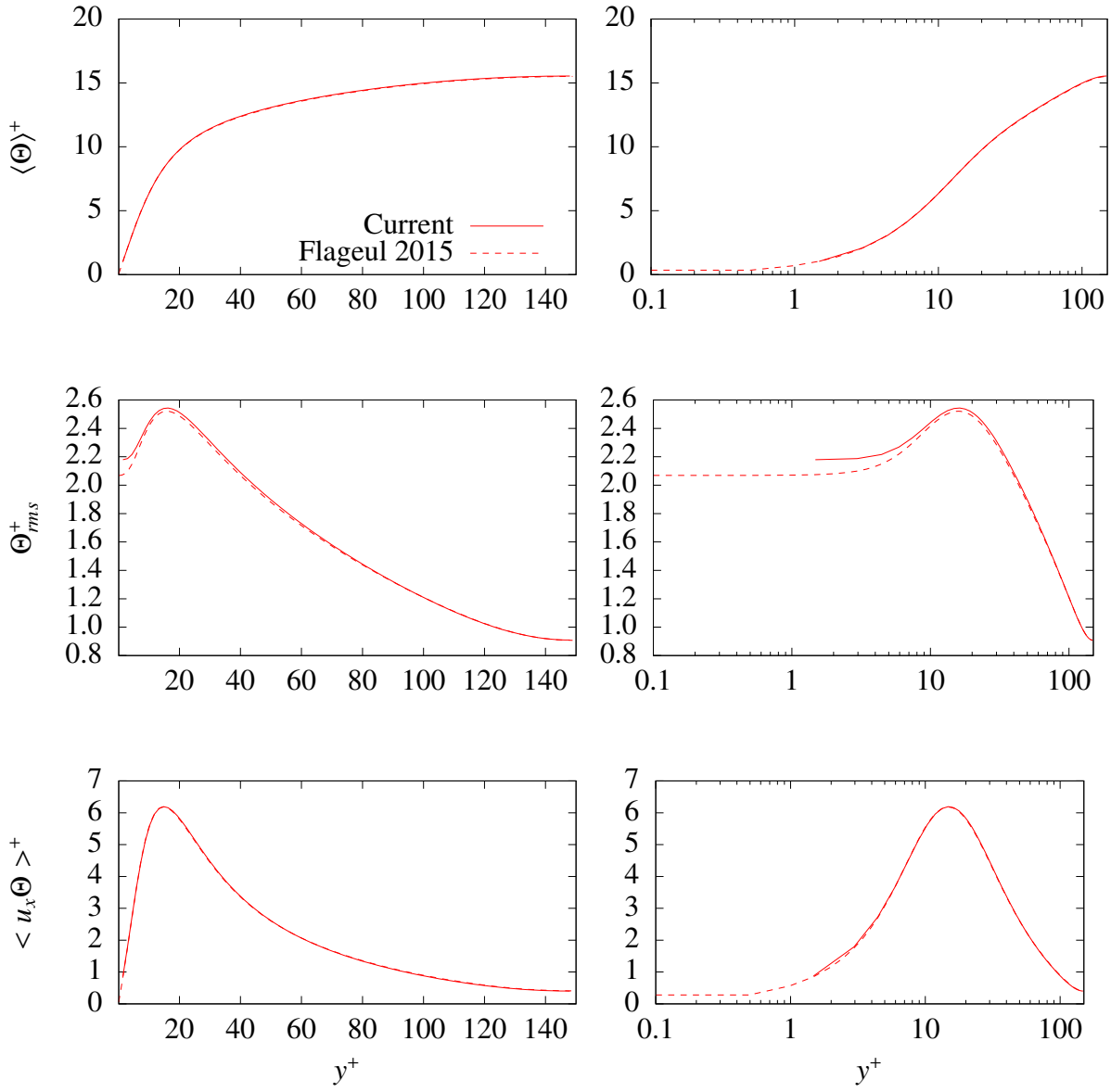

Figura 7.4: Temperature statistics in wall-units for channel flow (continuous line) compared to Flageul, 2015[17] (dashed line), for *locally imposed uniform-constant heat flux* (*IF*). Top row: Mean temperature profile $\langle\Theta\rangle^+$. Center row: Temperature root mean square profile Θ^+_{rms}. Bottom row: Turbulent heat flux profile $\langle u'_x\Theta'\rangle^+$.

7.1.2 Conjugate heat transfer in channel flow

In the *IBM* framework, the computational domain contains solid and fluid domains. Then, the temperature field in the solid is reconstructed in the fluid domain and the fluid velocity/temperature fields are reconstructed in the immersed solid domain (Figure 7.5).

Despite of the present fluid-solid weak coupling, the present original implementation is stable, accurate and capable to represent smoothly the heat fluxes at the interface, which is desirable when high order compact schemes are employed. It should pointed out that the temperature variance at the interface is directly associated to the dissipation rate discontinuity as Flageul *et al.* (2017)[18] addresses. The behavior of the discontinuity is highly dominated by the thermal diffusivity (G) and conductivity (G_2) ratios ([18]). In a Poiseuille flow, Figures 6.5 (for $G = 1$ and $G_2 = 1, 2, 4$) and 7.5 (for $G = 1$ and $G_2 = 2$) shows the temperature continuity condition ($\Theta = \Theta_s$) and the energy conservation $\left(\frac{\partial \Theta_s}{\partial y} = \frac{1}{G2}\frac{\partial \Theta}{\partial y}\right)$ at the interface. The turbulent *CHT* simulation is performed for unitary diffusivity and conductivity ratios ($G = G_2 = 1$) in order to ensure intermediate condition among the ideal imposed temperature ($G_2 \to 0$) or heat flux ($G_2 \to \infty$) conditions.

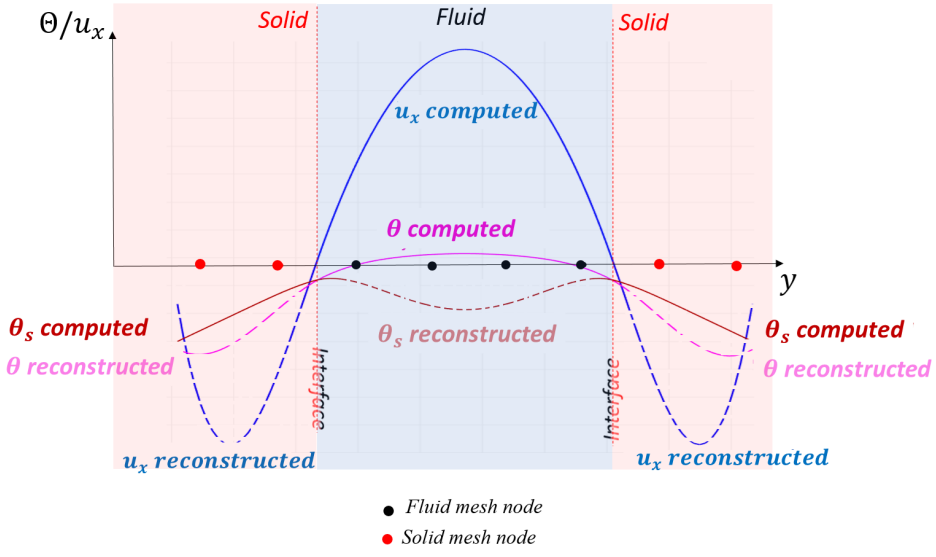

Figura 7.5: Streamwise velocity and temperature fields reconstruction. Illustration for laminar channel flow with $G = 1$ and $G_2 = 2$.

Figure 7.6 shows instantaneous velocity, fluid temperature and solid temperature fields embedded in the same computational domain. Turbulent structures either in the center of the

channel or the near-wall region are transferred from the flow to the temperature field. In most of the solid region, the temperature has a linear distribution, since the turbulent fluid-solid heat transfer only has considerable influence close to the interface.

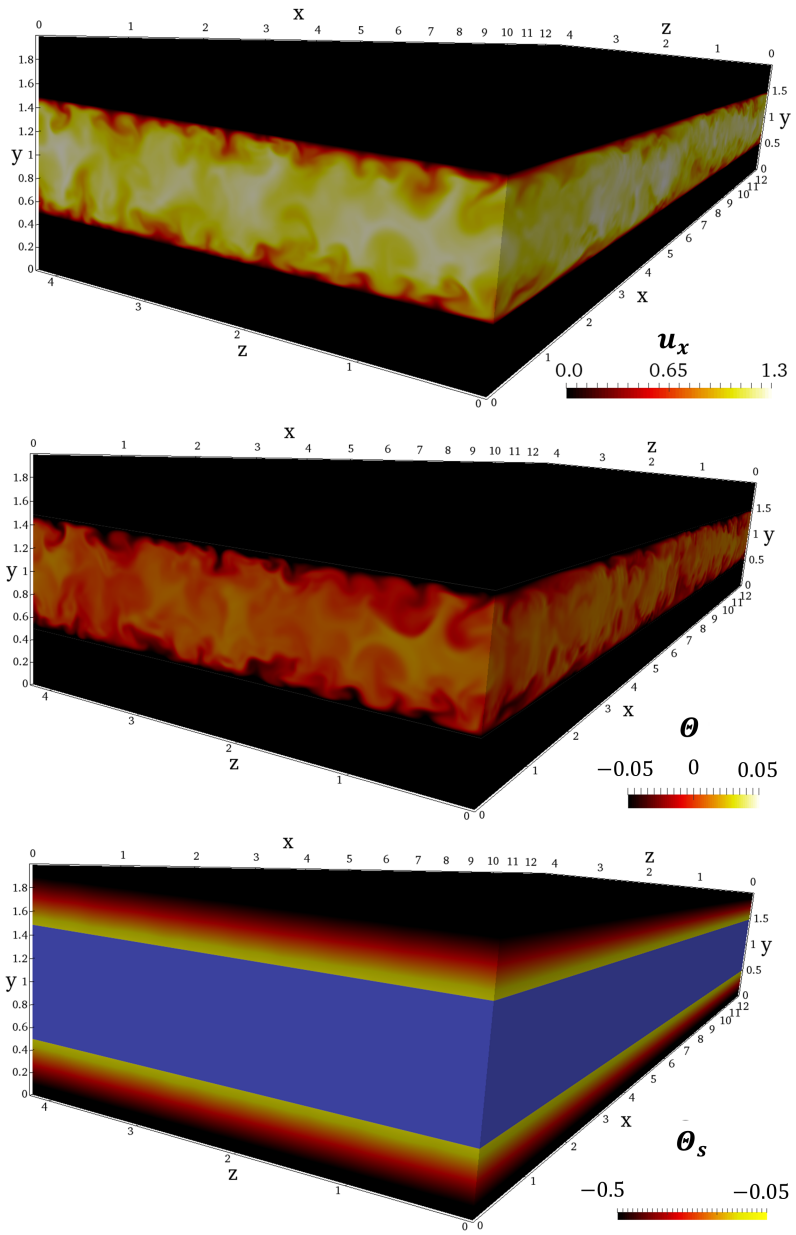

Figura 7.6: Streamwise velocity u_x, fluid temperature Θ and solid temperature Θ_s, employing the corresponding temperature dimensionless form, for *CHT* case. The simulation applies unitary diffusivity and conductivity ratios $G = G_2 = 1$. Blue field in the bottom row represents the fluid domain.

Temperature statistics have a good global agreement with the reference work (Figure 7.7). Temperature fluctuation and heat turbulent flux have an excellent agreement, for $y^+ > 20$, while having a poorer agreement, for $y^+ < 20$. This deviation relative to the reference can be associ-

ated with the weak thermal coupling at the interface, however, taking into account the present coarser mesh, this deviation is considered acceptable.

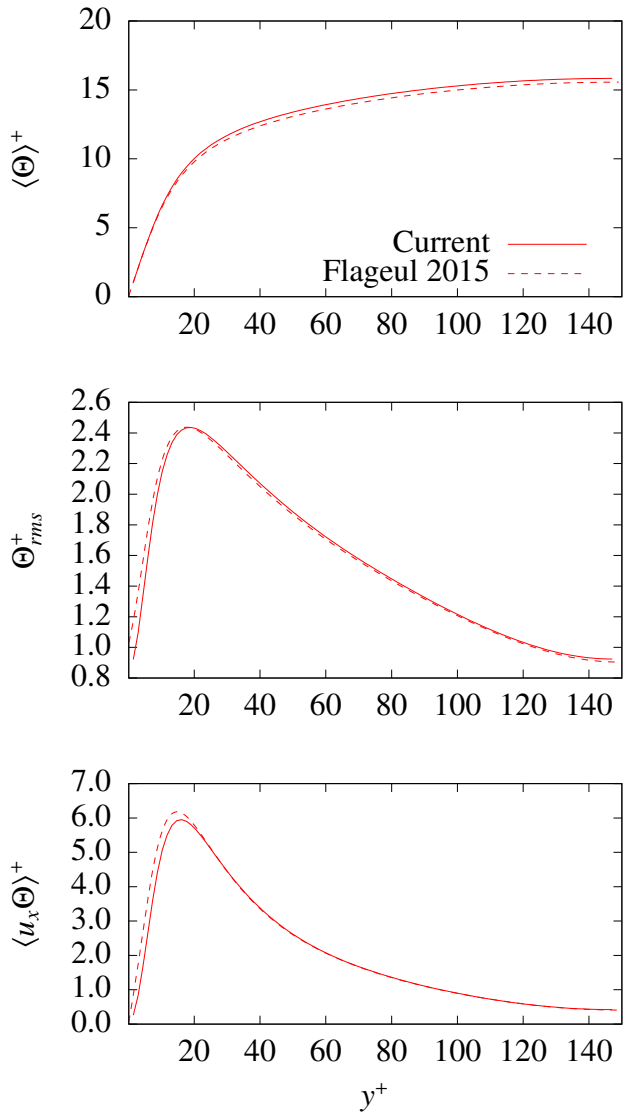

Figura 7.7: Temperature statistics for *CHT* condition in channel flow (continuous line) compared to Flageul, 2015[17] (dashed line). Top row: Mean temperature profile $\langle\Theta\rangle^+$. Center row: Temperature root mean square profile Θ^+_{rms}. Bottom row: Turbulent heat flux profile $\langle u'_x\Theta'\rangle^+$. Bottom row: Turbulent heat flux profile.

7.2 Validation of turbulent pipe flow

In this section, the basic velocity/temperature statistics in Turbulent Pipe Flow (*TPF*) are validated and discussed for imposed temperature at the wall (*IT*), for different Reynolds and Prandtl numbers. The spatial resolution ($N_x \times N_y \times N_z$) = (640×256×256), domain size ($L_x \times L_y \times L_z$) = ($12.5 \times 1.28 \times 1.28$) and the version of the velocity solver is the same employed in Dairay *et al.* (2017)[9] to perform simulations in turbulent pipe flow represented by an *IBM*. Figure 7.8 displays a 2D view of computational domain, uniform mesh employed in the pipe flow simulations and Table 7.4 presents the simulation parameters. At Re = 17000, two simulations are performed with different square modified wave number at the cutoff mesh: one for $k_c''=4\pi^2$ and a second one with $k_c''=8\pi^2$ in order to see the influence of the numerical dissipation over the smallest scales.

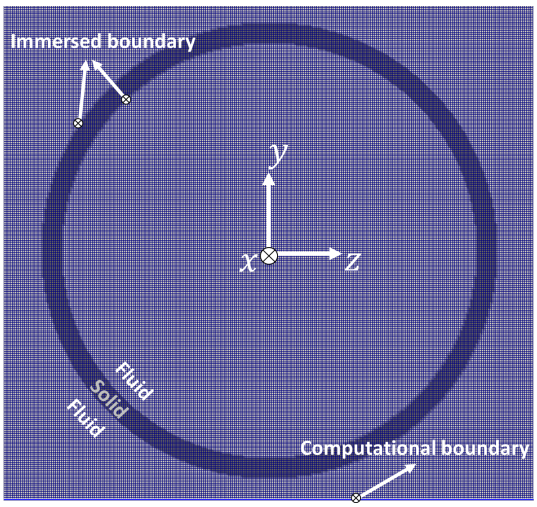

Figura 7.8: 2D visualization of the computational mesh in pipe flow. Figure adapted from Narváez *et al.* (2018b)[67].

Tabela 7.4: Flow parameters of simulations for verification of heat transfer in Turbulent Pipe Flow (*TPF*) and imposed temperature at the wall (*IT*). The time step was set at $\Delta t = 8 \times 10^{-4}$.

Simulation	k_c''	Re	Pr
TPF1	$4\pi^2$	5500	1.0
TPF2	$4\pi^2$	17000	0.71
TPF2.1	$8\pi^2$	17000	0.71
TPF3	$4\pi^2$	19000	0.71

Analogously to channel flow (Sec. 7.1), a field yielded from the Simulation *TPF3* is em-

ployed as the initial condition for the simulation at $Re = 5500$. Just as in channel flow, a turbulent simulation is considered as fully established when the time histories of Re_τ and Nu are statistically stationaries (Figure 7.9). These quantities are respectively related to the correction on the streamwise pressure gradient in the momentum equation and the streamwise temperature gradient in the energy equation. Note that Re_τ and Nu are outputs estimated and compared with the *DNS* reference works and the classical correlation of Gnielinski (1976)[27] (Figure 7.10 and Tables 7.5 and 7.6). Relative to any of the references works, Table 7.5 shows that the normal-wall refinement, close to the wall, is coarser in the present simulations. Under this consideration and regarding that the Nusselt number is globally estimated trough the energy source/sink term, deduced in this work (Eq. 5.44), the estimation in relation to the numerical and experimental references is considered very satisfactory (Figure 7.10 and Table 7.6).

Figure 7.9 shows the time history of the friction Reynolds number and the Nusselt number, normalized by the corresponding average value. The fluctuations of the Nusselt number relative to its average ($N'_{u\ rms}/\langle N_u \rangle$) are greater than the friction Reynolds number fluctuation relative to its average ($Re'_{\tau\ rms}/\langle Re_\tau \rangle$). In other words, in proportion to the corresponding average value, the Nusselt number shows higher fluctuations than the friction Reynolds number. Besides, conversely to $N'_{u\ rms}/\langle N_u \rangle$, the magnitude of the Nusselt number fluctuations ($N'_{u\ rms}$), for *TPF2* and *TPF3*, slightly decreases with increasing Reynolds number. This means that, in proportion to the averaged Nusselt number $\langle N_u \rangle$, the fluctuations increase when Re_τ increases (reinforce this affirmation with two last columns of Table 7.6).

To take the velocity/temperature information from the Cartesian mesh to a cylindrical mesh, it is adopted the 2^{th}-order projection procedure applied in Dairay *et al.* (2017)[9]. This procedure yields azimuthal-averaged profiles function of the radial distance to the wall, with a radial resolution Δr equal or more refined than the Cartesian one $\Delta x = \Delta y$ (Figure 7.11).

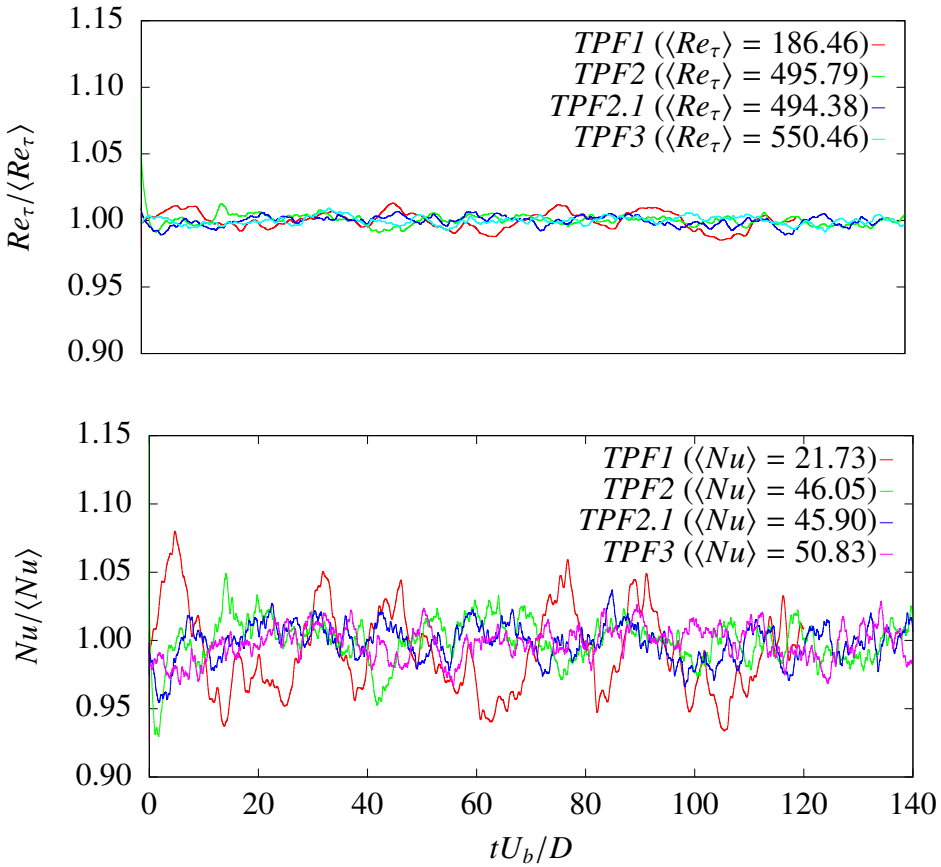

Figura 7.9: Time history of Re_τ (top) and Nusselt number Nu (bottom), normalized by the corresponding average value ($\langle Re_\tau \rangle$ and $\langle Nu \rangle$). These estimations correspond to simulations summarized in Tables 7.4 and 7.6.

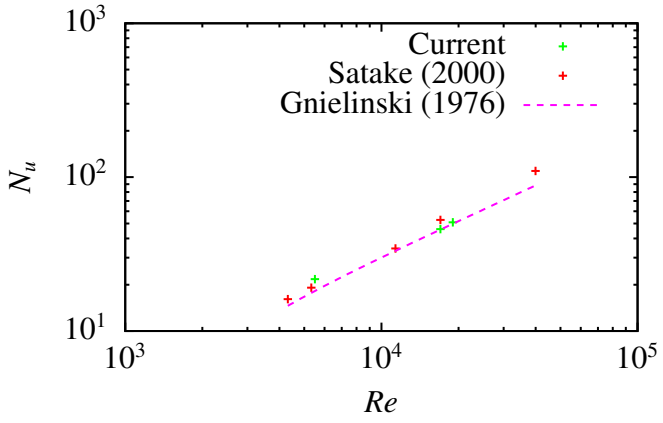

Figura 7.10: Nusselt number for turbulent pipe flow.

Tabela 7.5: *DNS* references and the present simulations. Spatial resolution in wall-units and numerical method.*FD*: Finite differences method; *FV*: finite volumes method; *SE*: spectral elements method.

Work	Δz^+	*Radial*	*Azimuthal*	Numerical method
TPF1	7.5	$\Delta x^+ = \Delta y^+ = 1.9$	$\Delta x^+ = \Delta y^+ = 1.9$	6^{th}-order *FD*
Redjem-Saad[84]	10.5	$\Delta r^+ \in [0.29; 1.04]$	$\Delta (R\theta)^+ = 8.84$	2^{th}-order *FD*
Saha[89]	9.3	$\Delta r^+ \in [0.061; 3.85]$	$\Delta (R\theta)^+ = 9.13$	*SE*
El Khoury[12]	[3.03; 9.91]	$\Delta r^+ \in [0.14; 4.44]$	$\Delta (R\theta)^+ = [1.51; 4.93]$	*SE*
Satake [92]	10.5	$\Delta r^+ \in [0.29; 1.04]$	$\Delta (R\theta)^+ = 8.84$	*FV*
Isshiki [33]	–	–	–	Experimental
TPF2	19.4	$\Delta x^+ = \Delta y^+ = 5.0$	$\Delta x^+ = \Delta y^+ = 5.0$	6^{th}-order *FD*
TPF2.1	19.3	$\Delta x^+ = \Delta y^+ = 4.9$	$\Delta x^+ = \Delta y^+ = 4.9$	6^{th}-order *FD*
TPF3	21.5	$\Delta x^+ = \Delta y^+ = 5.5$	$\Delta x^+ = \Delta y^+ = 5.5$	6^{th}-order *FD*
Satake [92]	14.6	$\Delta r^+ \in [0.1; 2.6]$	$\Delta (R\theta)^+ = 8.18$	*FV*
El Khoury[12]	[3.06; 9.99]	$\Delta r^+ \in [0.15; 4.49]$	$\Delta (R\theta)^+ = [1.45; 4.75]$	*SE*

Tabela 7.6: *DNS* references. Friction Reynolds number, Prandtl number and Nusselt number.

Work	*Re*	$\langle Re_\tau \rangle$	$Re'_{\tau\ rms}$	*Pr*	$\langle N_u \rangle$	$N'_{u\ rms}$
TPF1	5500	186.46	1.223	1.0	21.73	0.631
Redjem-Saad[84]	5500	186	–	1.0	–	–
Saha[89]	5500	186	–	1.0	–	–
El Khoury[12]	5300	181	–	–	–	–
Satake [92]	5300	186	–	0.71	18.74	–
Isshiki [33]	5300	180	–	–	20.06	–
TPF2	17000	495.79	1.675	0.71	46.05	0.637
TPF2.1	17000	494.38	1.681	0.71	45.90	0.574
TPF3	19000	550.51	1.694	0.71	50.83	0.577
Satake [92]	17000	500	–	0.71	$\approx$ 52.74	–
El Khoury[12]	19000	550	–	–	–	–

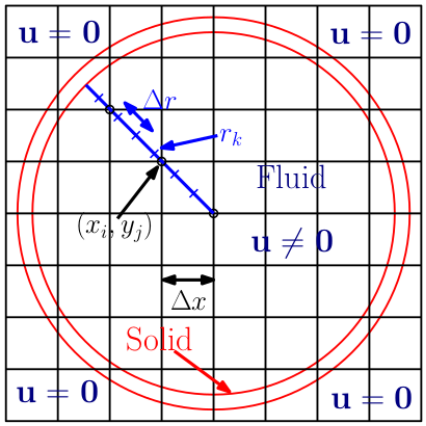

Figura 7.11: sketch of the parameters for the projection from the Cartesian grid (x_i,y_j) to the discretized radial coordinate r_k. Figure adopted from Dairay *et al.* (2017)[9].

Comparing the present results with the *DNS* references (Figure 7.12), an excellent agreement of the velocity statistics at $Re = 5500$ ($Re_\tau = 186$) and a poorer agreement at $Re = 17000$ ($Re_\tau = 500$) and $Re = 19000$ ($Re_\tau = 550$) were reached. The poorer agreement is observed in the estimation of the peak of the streamwise Reynolds stressed $\langle u_x u_x \rangle$, which is underestimated in about 7.5%. As the present mesh is uniform and the reference one is a near-wall stretched mesh, Dairay *et al.* (2017)[9] suggest that this poor agreement at $Re = 19000$ and $Re = 17000$ could mainly related to the coarser resolution in the wall-normal direction. The simulations at $Re = 17000$ with different numerical dissipation at the cutoff mesh do not show appreciable differences (center row of Figure 7.12).

At $Re_\tau = 186$, the temperature statistics show excellent agreement with the most recent reference work (Figure 7.13), however, the peaks of the temperature fluctuations *rms* (Θ^+_{rms}) and the turbulent heat flux ($\langle u'_x \Theta' \rangle^+$) are slightly higher than the references ones (around 2% and 3%, respectively).

On the other hand, at $Re_\tau = 500$, in the core of the pipe, our results are considerably higher than the data of Satake *et al* (2000)[92] (Figure 7.14). Considering the moderate Re_τ, our coarser resolution and our high precision numerical scheme, in contrast with the finite volume of Satake *et al*, the results are considered very satisfactory and consistent. Moreover, the typical protuberance of the statistics in the pipe core region ($y^+ > 100$), associated to large turbulent scales for the highest Reynolds numbers, is consistently reproduced and slightly intensified for $Re_\tau = 550$ in relation to $Re_\tau = 500$. It should be stressed that this protuberance is also identified in the present velocity statistics (Figure 7.12) and it was already reported in the review section of this work (Figure 2.4 for velocity and Figure 2.7 for temperature).

Figures 7.15 and 7.16 (for $Re_\tau = 186$ and $Re_\tau = 550$, respectively) show instantaneous velocity and fluid temperature fields in a cross section at the middle of the pipe. As temperature transport is driven by the velocity, the instantaneous temperature fields show turbulent structures highly correlated with velocity. As expected, for the higher Reynolds number ($Re_\tau = 550$) the size distribution of the observed turbulent structures is richer than the simulation for $Re_\tau = 186$. This is also identifiable in the iso-surfaces of temperature illustrated in Figures 7.17 and 7.18. The turbulent biggest (in the core of the pipe) and smallest (near-wall) structures are well

represented and no numerical artificial oscillations are visually identified near the wall, where the *IBM* has the most incidence.

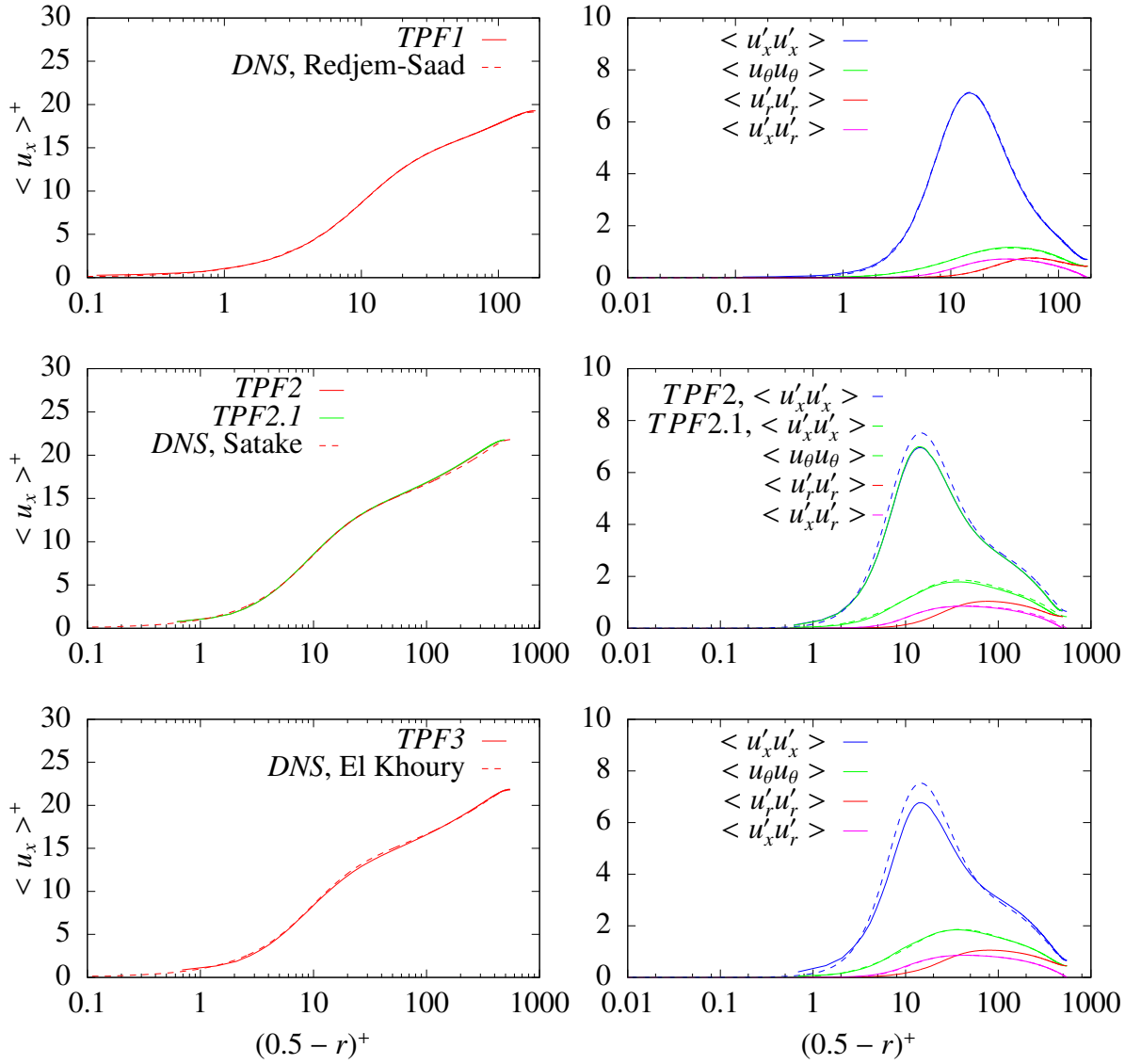

Figura 7.12: Current velocity statistics (continuous line) compared to DNS references [84],[92] and [12] (dashed lines). Left: Mean velocity profiles $\langle u_x \rangle^+$. Right: Reynolds stresses profiles. $\left\langle u_i' u_j' \right\rangle^+$ Top: $Re = 5500$ ($Re_\tau = 186$); center: $Re = 17000$ ($Re_\tau = 500$); bottom: $Re = 19000$ ($Re_\tau = 550$). Azimuthal average with $\Delta r = \Delta x/8$.

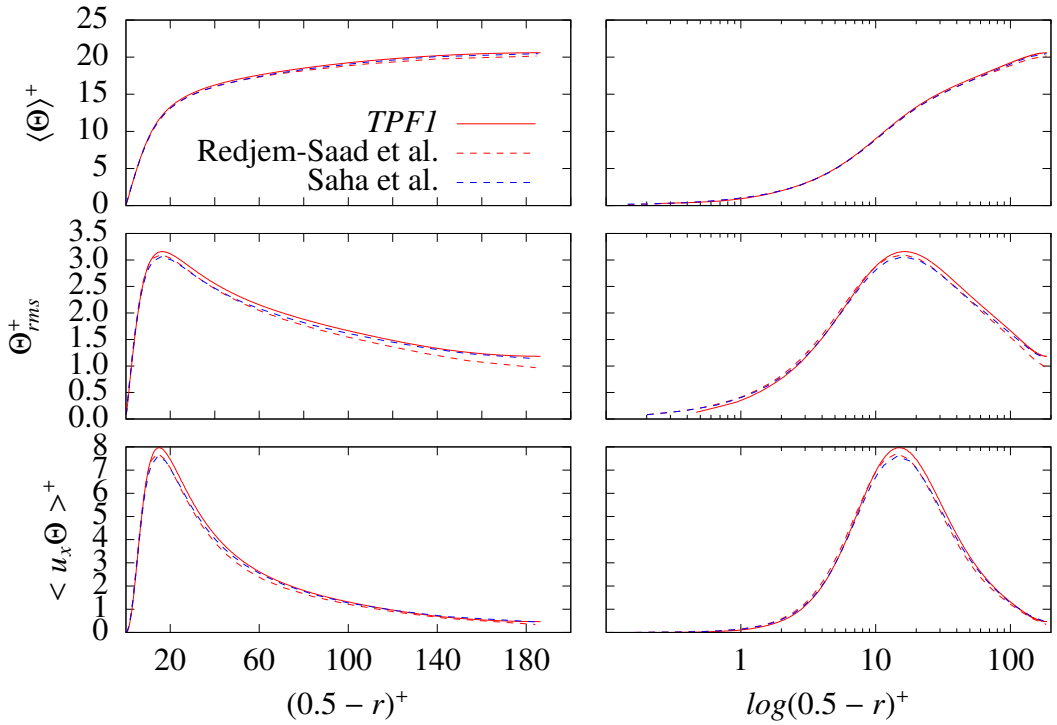

Figura 7.13: Temperature statistics, at $Re_\tau = 186$ ($Re = 5500$) and $Pr = 1$, compared to Redjem-Saad *et al.* (2007)[84] and Saha *et al.* (2014)[89]. Top row: Mean temperature profile $\langle\Theta\rangle^+$. Center row: Temperature root mean square profile Θ^+_{rms}. Bottom row: Turbulent heat flux profile $\langle u'_x\Theta'\rangle^+$. Azimuthal average with $\Delta r = \Delta x/8$.

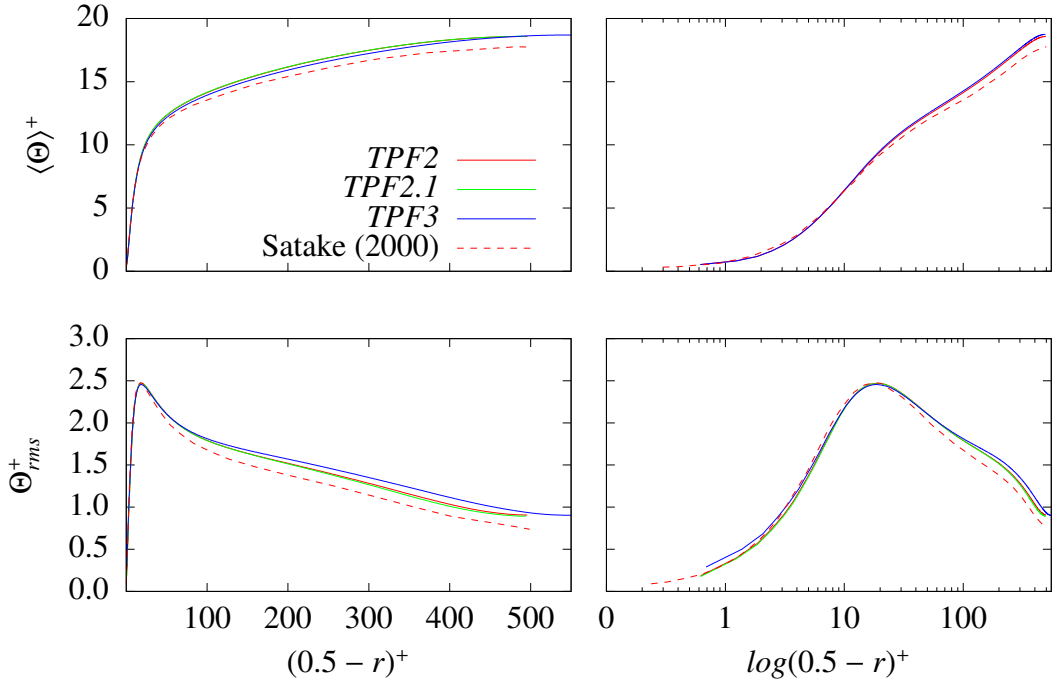

Figura 7.14: Temperature statistics (at $Re_\tau = 500$, $Re_\tau = 550$ and $Pr = 0.71$) compared to Satake *et al.* (2000)[92] ($Re_\tau = 500$). Mean temperature profile (Top) and Temperature root mean square profile (Bottom). Azimuthal average with $\Delta r = \Delta x/8$.

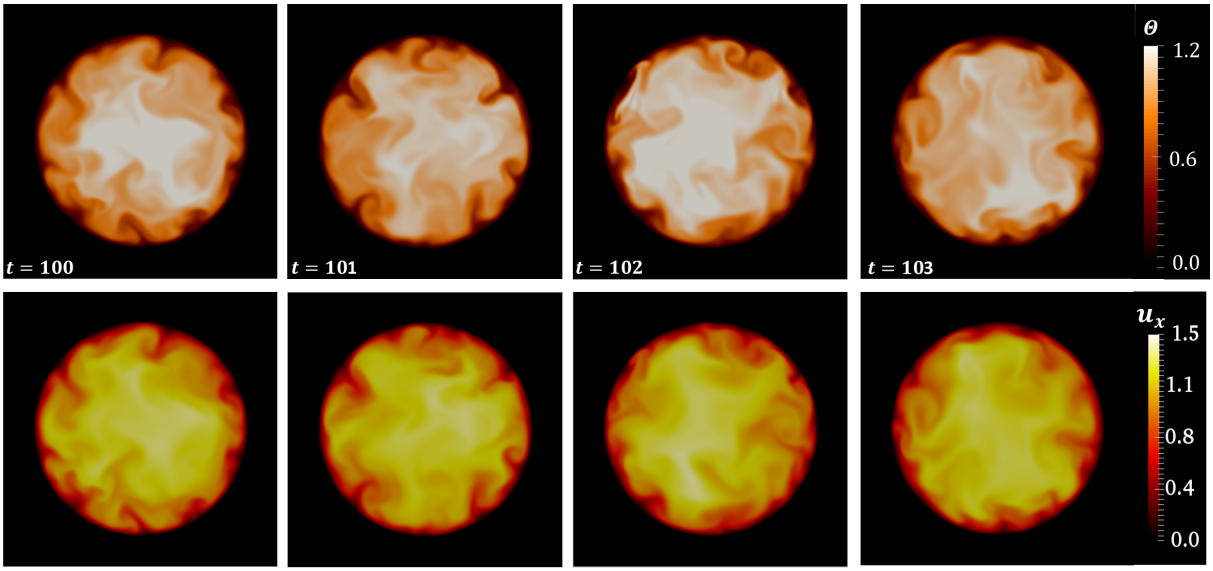

Figura 7.15: Instantaneous temperature Θ (first row) and streamwise velocity u_x (second row) fields at cross section in $x = L_x/2$, at $Re_\tau = 186$ ($Re = 5500$) and $Pr = 1$.

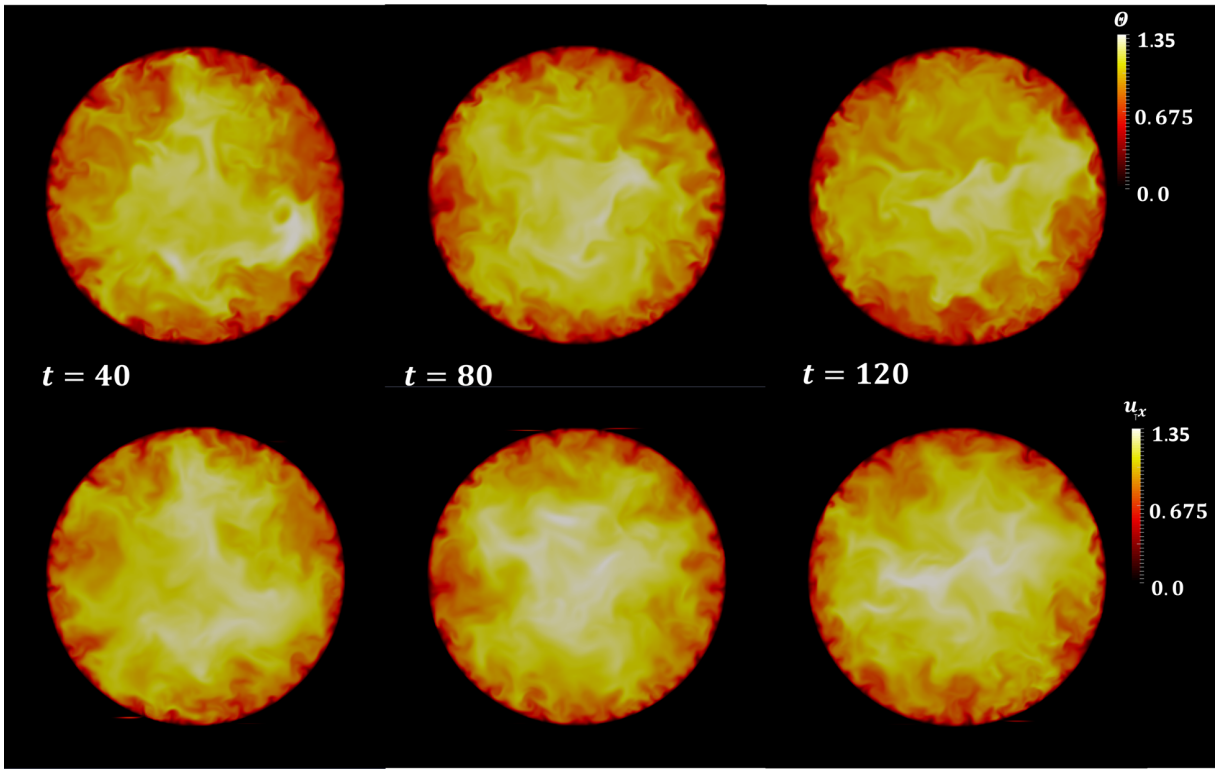

Figura 7.16: Instantaneous temperature Θ (first row) and streamwise velocity u_x (second row) fields at cross section in $x = L_x/2$, at $Re\tau = 550$ ($Re = 19000$) and $Pr = 0.71$.

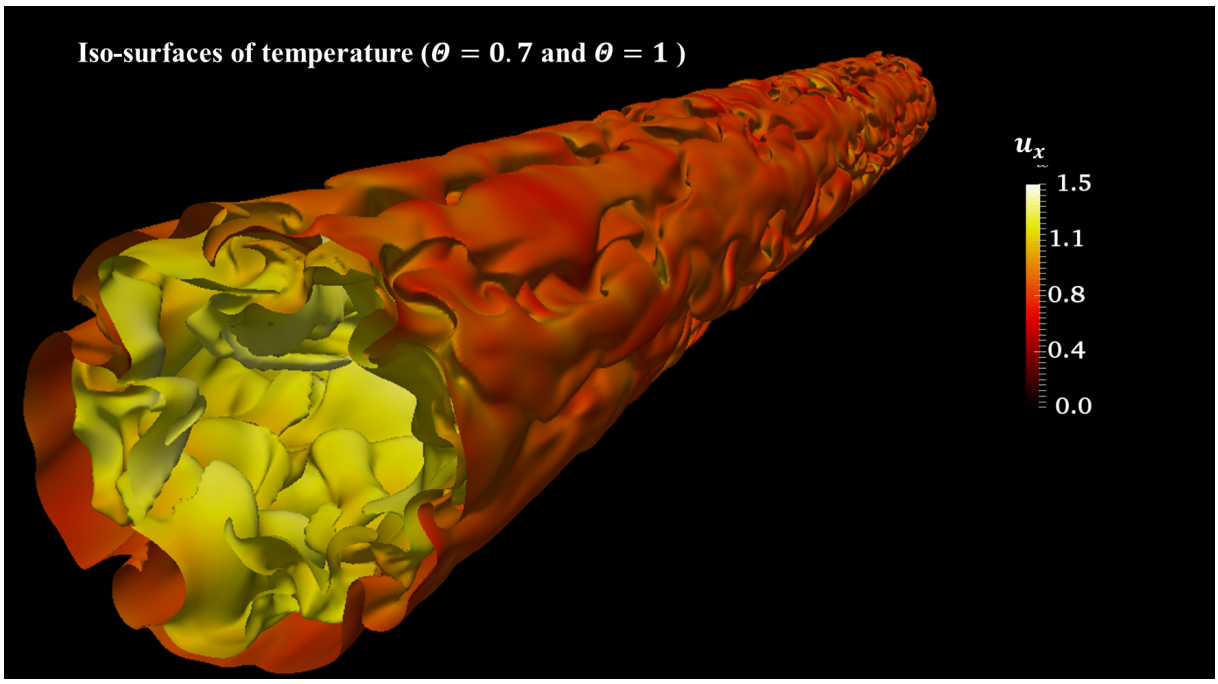

Figura 7.17: Iso-surfaces of temperature, at $Re_\tau = 186$ ($Re = 5500$) and $Pr = 1$.

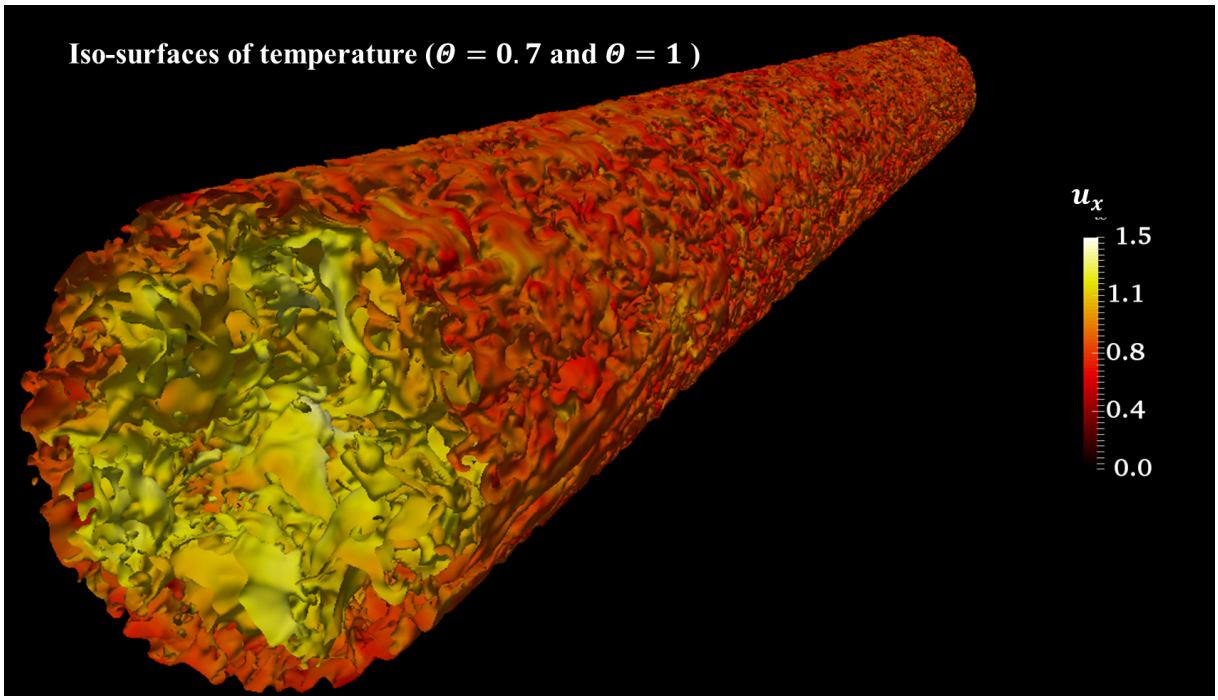

Figura 7.18: Iso-surfaces of temperature Θ, at $Re_\tau = 550$ ($Re = 19000$) and $Pr = 0.71$.

7.3 Concluding remarks on turbulent results

In the foregoing sections, the implementations are validated for turbulent channel and pipe flow by comparing the basic velocity/temperature statistics, the friction Reynolds number Re_τ and the Nusselt number Nu estimations to *DNS* reference works based on a body-fitted and near-wall stretched mesh. The channel flow is evaluated for three thermal boundary conditions at the *IB*, while the pipe flow is evaluated and studied for *IT* boundary condition. The main remarks of the results are listed below.

The friction Reynolds number is estimated (Eq. 5.26) with small deviation from the reference works, especially for pipe flow. The source/sink term deduced, implemented and applied in this work allows estimating a global averaged Nusselt number $\langle Nu \rangle$ with considerable accuracy (Eq. 5.44).

The turbulent velocity/temperature structures are well represented and do not show artificial numerical oscillations at the near-wall, where the *IBM* has the most impact.

In channel flow:

- For imposed temperature (*IT*) and imposed heat flux (*IF*) at the wall, the velocity/temperature has an excellent agreement with the reference works. However, in *IF* case, the temperature fluctuation are slightly greater than the reference, for $y^+ < 10$.

- For the most demanding conjugate heat transfer (*CHT*) case, an excellent global agreement is reached, with a present sequential coupling.

In pipe flow:

- The velocity/temperature statistics have an excellent agreement, however the peak of the streamwise Reynolds stresses $\langle u'_x u'_x \rangle$ are slightly underestimated for $Re = 17000$ ($Re_\tau = 500$) and $Re = 19000$ ($Re_\tau = 550$). At $Re = 5500$ ($Re_\tau = 186$), the second order temperature statistics (*e. i.* Θ^+_{rms} and $\langle u_x \Theta \rangle^+$) show small deviation from the *DNS* references. At $Re_\tau = 500$ and $Re_\tau = 550$, the temperature statistics are higher than the *DNS* reference in the core of the pipe, where our simulations clearly show a consistent protuberance associated to the biggest turbulent scales.

- Our simulations based on numerical modulated viscosity together with the *IBM* and the azimuthal averaging procedure can represent accurately the temperature statistics in thermal sublayer, even for coarser resolution than the layer thickness.

Chapter 8

Conclusions

This thesis deals numerically with the fluid-solid thermal interaction *via* a dual immersed boundary method (*IBM*). The configurations studied are internal pipe and channel laminar turbulent flows. The high precision code *Incompact3d* is employed as fluid dynamic solver and all developments are carried out on this code. The *Incompact3d* derivative operators are also used to solve the energy governing equations for the temperature, which are coupled at the fluid-solid interface by mean an efficient weak coupling. The main methodological contributions of this work are listed below.

- A time dependent temperature (energy) source/sink term is deduced, implemented, applied and validated, which allows compensating the streamwise temperature gradient enabling to deal with a periodic internal flow, in three different thermal boundary conditions.

- A methodology in *Incompact3d* code, which allows prescribing temperature Dirichlet and Neumann boundary conditions by using a customized immersed boundary method, is developed, implemented and evaluated. The biggest challenges lies on the implementation of the Neumann-type boundary condition, because for Dirichlet-type boundary condition the velocity *IBM* was harnessed.

Channel flow is evaluated for three types of thermal boundary conditions (*TBC*) at the fluid-solid interface: ideal locally imposed temperature (Dirichlet-type boundary condition), ideal locally imposed heat flux (Neumann-type boundary condition) and real conjugate heat transfer

(Dirichlet and Neumann type boundary conditions). Pipe flow is evaluated for the imposed temperature case.

Laminar cases are verified by comparing with analytical solutions, while turbulent cases are validated with references *DNS* works. The friction Reynolds number is accurately estimated, especially for pipe flow. The variable energy source/sink term proposed in this work allows estimating a global averaged Nusselt number with considerable accuracy.

In channel flow

- The convergence order of the error increases with increasing order of the polynomial reconstructed inside the immersed region (increasing the polynomial order implies to increase the number of fluid nodes information). For *IT* case with the immersed boundary (*IB*) collocated on mesh nodes, up to 6^{th}-order accuracy is reached. At the *IB*, up to 2^{th}-order of convergence is achieved for *IF* and *CHT* (since imposed heat flux is required).

- In internal laminar flows (no pressure gradient in wall-normal direction) with staggered *IB* location, the velocity/temperature convergence order is closely relate to the *IB* location error ($\sim \Delta x^1$). Thus, the second-order accuracy reached for this case is consistent with the velocity analytical solution, which is a second-order polynomial function of the distance to the wall.

- The thermal basic statistics have an excellent agreement with the *DNS* references, however, for *IF* and *CHT* our results show a deviation from the reference data in $y^+ < 10$ and $y^+ < 20$, respectively.

- The dual *IBM*, for the *CHT* case, allows simulating scenarios with different fluid-to-solid ratios of the conductivity (G_2) by efficiently representing the sudden medium transition and even maintaining continuous derivatives.

In pipe flow

- The distribution of the first-derivative error shows a strong dependence on the direction in which the derivative is computed. Then it was shown that the pattern of error distribution

depends on the orientation of the *IB* interface relative to the mesh.

- The main impact of imposing a variable energy source term (adjusting Θ_b) is identified on the error spatial distribution, which has a local peak at the pipe center.

- The maximum errors are located near to the immersed boundary, thus the norm L_∞ shows 2^{th}-order convergence, while norm L_2 shows a higher order of convergence, since this norm considers the errors in the pipe core, which are certainly smaller than the error close to the immersed boundary.

- At $Re = 17000$ ($Re_\tau = 500$) and $Re = 19000$ ($Re_\tau = 550$), the velocity/temperature statistics have an excellent agreement with the reference *DNS*. At $Re_\tau = 500$ and $Re_\tau = 550$, the temperature statistics are higher than the *DNS* reference in the core of the pipe, where our simulations are able to capture a *protuberance* associated to the biggest turbulent scales.

- Our simulations, based on numerical modulated viscosity, together with the *IBM* and the azimuthal averaging procedure can represent accurately the temperature statistics in thermal sublayer, even for coarser resolution than the layer thickness.

The present customized immersed boundary method (*IBM*) is capable to prescribe Dirichlet and Neumann boundary conditions at the interface. The *IBM* can represent Dirichlet boundary conditions with high precision, even in the thermal sublayer and using coarser mesh than the *DNS* references. When the solid geometry is compatible with the Cartesian mesh (*e. g.* channel flow), the strategy can represent a Neumann-type boundary condition with a small deviation of the temperature root mean square in the near-wall region. Real conjugate heat transfer is simulated and, although there are slight discrepancies in the temperature statistics, the phenomenon is consistently represented. The versatility, the relative low computational capacity required and the simple implementation of fluid-solid thermal coupling make this *IBM* approach a promising candidate to continue studying fluid-solid thermal interaction.

Appendix A

Thermal energy equation (Source/sink term in pipe/channel periodic flow)

The dimensional energy equations in the fluid domain, with invariant properties, can be expressed by the temperature convection-conduction equation

$$\frac{\partial T}{\partial t} = -\vec{V} \cdot \nabla T + \alpha \nabla^2 T, \tag{A.1}$$

where the first term on the right-hand side represents the heat transport by convection of the temperature in fluid with a velocity field $\vec{V}$, while the second models the heat transfer by conduction. Sometimes is convenient to *normalize* the temperature, i. e., making a variable change. For instance, considering a heated/cooled internal flow in x-direction, by substituting the dimensionless temperature by

$$\Theta = \frac{\langle T|_{int} \rangle(x) - T(x,y,z,t)}{T_r(x)}, \tag{A.2}$$

in Equation A.1, we obtain

$$\frac{\partial \Theta}{\partial t} = -\vec{u} \cdot \nabla \Theta + \frac{1}{RePr} \nabla^2 \Theta + f_\Theta, \tag{A.3}$$

where T_r is the reference temperature (scaling factor), $T\,|_{int}$ is the wall temperature (translation factor), $\langle \cdot \rangle$ is the average operator in spanwise/azimuthal-time, Re is the Reynolds number and

$Pr = \nu/\alpha$ is the Prandtl number which relates the fluid viscosity and its thermal diffusivity. The additional quantity, f_Θ, is a source term expressed by

$$f_\Theta = -\frac{u_x}{T_r}\left[\Theta\left(\frac{dT_r}{dx}\right) - \frac{d\langle T\,|_{int}\rangle}{dx}\right] + \frac{1}{RePr}\frac{1}{T_r}\left[\Theta\left(\frac{d^2T_r}{dx^2}\right) + 2\frac{\partial\Theta}{\partial x}\left(\frac{dT_r}{dx}\right) - \frac{d^2\langle T\,|_{int}\rangle}{dx^2}\right]. \tag{A.4}$$

As it will be shown, f_Θ allows making a correction in the temperature gradient to maintain dimensionless bulk temperature uniform in streamwise direction ($\Theta_b = constant$), which is desirable in streamwise periodic flows.

In a thermal fully developed flow under ideal thermal boundary conditions with temperature profile similarity, an appropriate scaling factor $T_r(x)$ could ensure the dimensionless mean temperature profile $\langle\Theta\rangle$ and the bulk temperature Θ_b invariant along x

$$\frac{\partial\langle\Theta\rangle}{\partial x} = \frac{\partial}{\partial x}\left[\frac{\langle T\,|_{int}\rangle(x) - \langle T\rangle(x,y,z)}{T_r(x)}\right] = 0 \tag{A.5}$$

and

$$\frac{\partial\Theta_b}{\partial x} = \frac{\partial}{\partial x}\left[\frac{\langle T\,|_{int}\rangle(x) - T_b(x)}{T_r(x)}\right] = 0, \tag{A.6}$$

which is true for

$$T_r \propto \langle T\,|_{int}\rangle - T_b. \tag{A.7}$$

The equalities A.5 and A.6 and the proportionality condition A.7 can be established for **ideal locally imposed uniform flux heat** *(IF)*, **ideal locally imposed non-uniform temperature** *(IT)* or **ideal locally imposed uniform temperature** *(IUT)* boundary conditions (Figure A.1). It should be pointed out that, both *IF* and *IUT* boundary conditions can not be imposed simultaneously, because uniform-constant wall heat flux ($\varphi|_{int} = constant$) implies $d\langle T\,|_{int}\rangle/dx \neq 0$ ($T\,|_{int} \neq constant$), while, uniform-constant wall temperature ($T\,|_{int} = constant$) implies $d\langle\varphi|_{int}\rangle/dx \neq 0$ ($\varphi|_{int} \neq constant$). However, as the second column of Figure A.1 shows, the wall temperature can be imposed to be linearly variable in x ($T\,|_{int} = T\,|_{int}(x)$) to maintain the heat flux uniform in mean, $d\langle\varphi|_{int}\rangle/dx = 0$ ($\varphi|_{int} \neq \langle\varphi|_{int}\rangle = constant$). In the present text,

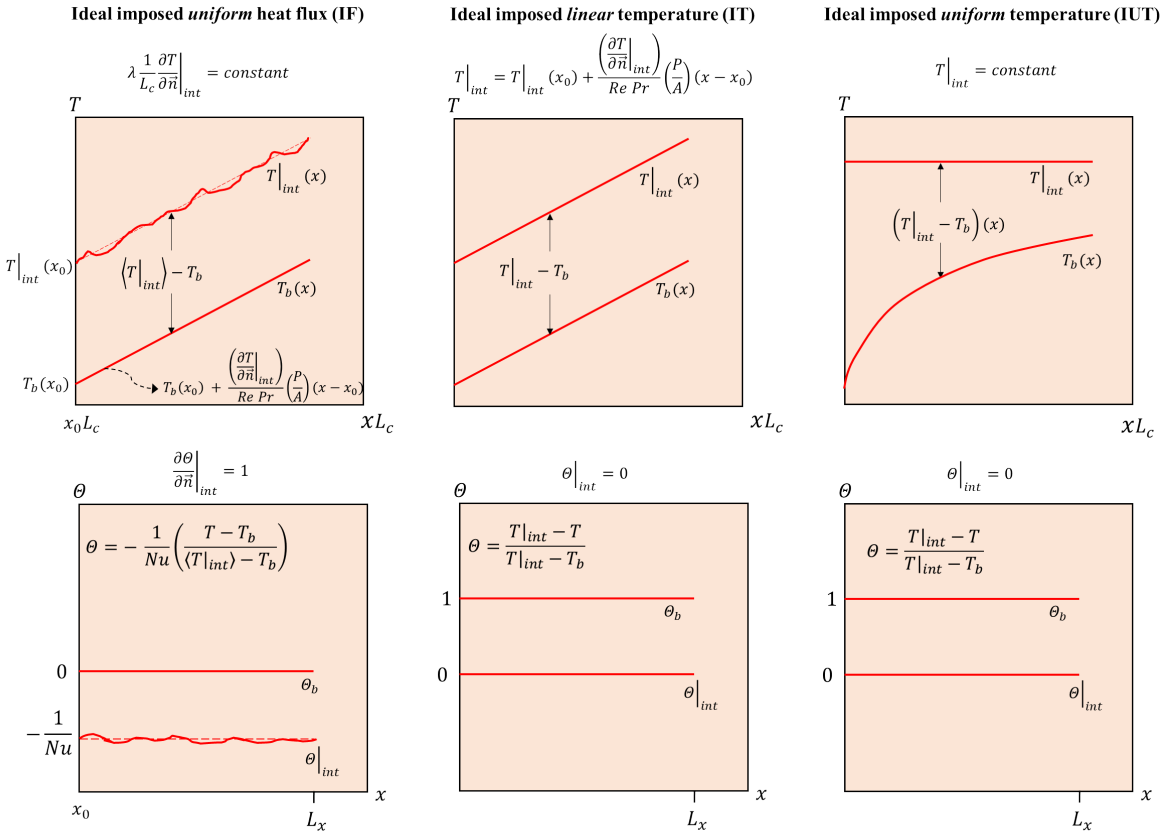

Figura A.1: Streamwise variation of temperature in thermal fully developed flow, for some ideal thermal boundary conditions. Top: dimensional temperature; bottom: dimensionless temperature. The derivative operator normal to the wall is dimensionless and the normal vector is pointing towards the fluid.

this ideal thermal condition is referred as ideal locally imposed linear temperature boundary condition which corresponds to a particular case of **ideal locally imposed non-uniform temperature** *(IT)*. This ideal condition is the so-called mixed-type condition in Piller (2005)[80].

It is interesting to note that expanding and averaging Equation A.5 with $T_r = \langle T\,|_{int}\rangle - T_b$, the following useful relation between the averaged streamwise temperature gradients

$$\frac{\partial \langle T\rangle}{\partial x} = \frac{d\langle T\,|_{int}\rangle}{dx} - \frac{\langle T\,|_{int}\rangle - \langle T\rangle}{\langle T\,|_{int}\rangle - T_b}\left(\frac{d\langle T\,|_{int}\rangle}{dx}\right) + \frac{\langle T\,|_{int}\rangle - \langle T\rangle}{\langle T\,|_{int}\rangle - T_b}\left(\frac{dT_b}{dx}\right). \tag{A.8}$$

Furthermore, by applying an *overall energy balance* to a differential volume control of pipe/channel (Pdx) submitted to *IF* ($\varphi|_{int} \equiv constant$), from Incropera and Dewit[32], an expression for the bulk temperature streamwise gradient is

$$\frac{dT_b}{dx} = \frac{P\,\varphi|_{int}}{\dot{m}c_p} = \frac{\beta\,\varphi|_{int}}{\rho c_p U_b}, \tag{A.9}$$

where $\dot{m} = \int_A \rho u_x dA = \rho U_b A$ is the mass flux, P is the wetted perimeter, A is the cross-sectional duct area, c_p is the fluid heat capacity and $\beta = 4$ for pipe flow and $\beta = 2$ for channel flow. Integrating this equation, it can be found

$$T_b(x) = T_b(x_0) + \frac{P\,\varphi|_{int}}{\dot{m}c_p}(x - x_0). \tag{A.10}$$

In contrast, for *IT* ($T\,|_{int} = constant$), it can be demonstrated

$$-\frac{1}{T_r}\frac{dT_r}{dx} = \frac{\beta Nu}{RePr} \quad \Longrightarrow \quad \langle\varphi|_{int}\rangle(x) = \langle\varphi|_{int}\rangle(x_0) exp\left(-\frac{\beta Nu}{RePr}x\right) \tag{A.11}$$

and

$$\frac{1}{T_r}\frac{d^2T_r}{dx^2} = \left(\frac{\beta Nu}{RePr}\right)^2. \tag{A.12}$$

The Reynolds number Re and the Nusselt number Nu are based on characteristic length L_c ($\equiv D$ or $\equiv H$ for pipe or channel flow, respectively). The Nusselt number is defined as

$$Nu = \frac{hL_c}{\lambda} = function(Re, Pr), \tag{A.13}$$

where h is the local convection heat transfer coefficient from Newton's law of cooling expressed by

$$\langle\varphi|_{int}\rangle(x) = h\left(\langle T|_{int}\rangle - T_b\right). \tag{A.14}$$

The coefficient h can be a function of x in the entrance region, but is constant along the duct where the thermal fully developed condition was reached.

A.1 Ideal locally imposed uniform heat flux

When $\langle \varphi|_{int} \rangle = constant$, from Equation A.14, it can be deduced that

$$\frac{dT_b}{dx} = \frac{d\langle T|_{int}\rangle}{dx}, \qquad \varphi|_{int} = constant. \tag{A.15}$$

Substituting this result in Equation A.8 and using Expression A.9, the following equalities must be satisfied

$$\frac{\partial\langle T\rangle}{\partial x} = \frac{d\langle T|_{int}\rangle}{dx} = \frac{dT_b}{dx} = \frac{\beta\,\varphi|_{int}}{\rho c_p U_b}, \qquad \varphi|_{int} = constant. \tag{A.16}$$

This means that *streamwise temperature gradients* does not dependent on space. Then, equivalently as was done in the momentum equation (Eq. 4.2), in periodic flow it should be done a correction in the *streamwise temperature gradient* to maintain constant the rate of change of T_b (Saha *et al.*, 2001[88]). From Equations A.4 and A.16, the source term, added to the temperature transport equation (Eq. A.3), becomes

$$f_\Theta = \frac{u_x}{T_r}\left[\frac{d\langle T|_{int}\rangle}{dx}\right] = \frac{u_x}{T_r}\left[\frac{\beta\,\varphi|_{int}}{\rho c_p U_b}\right]. \tag{A.17}$$

Then, using the Fourier's law, the heat flux normal to the wall towards the fluid ($\vec{n} = [n_y\, n_z]^T$) is

$$\varphi|_{int} = -\frac{k}{D}\left.\frac{\partial T}{\partial \vec{n}}\right|_{int} \; or \; -\frac{k}{H}\left.\frac{\partial T}{\partial \vec{n}}\right|_{int}, \tag{A.18}$$

and the source term can be rewritten as

$$f_\Theta = \frac{\beta u_x}{RePr}\left(\left.\frac{\partial\Theta}{\partial\vec{n}}\right|_{int}\right), \tag{A.19}$$

where the dimensionless temperature gradient through the wall ($\partial_{\vec{n}}\Theta|_{int}$) depends on the assumed normalization. As the normalization is function of known quantities, they should be defined for the corresponding thermal boundary condition. The values of the normal-wall temperature gradient for different dimensionless for are

$$\left.\frac{\partial\Theta}{\partial\vec{n}}\right|_{int} = \begin{cases} Nu, \quad if \quad \Theta = \dfrac{\langle T|_{int}\rangle - T}{\langle T|_{int}\rangle - T_b} \\ \\ RePr, \quad if \quad \Theta = \dfrac{\langle T|_{int}\rangle - T}{\dfrac{\varphi|_{int}}{\rho c_p U_b}} \\ \\ 1, \quad if \quad \Theta = \dfrac{1}{Nu}\left(\dfrac{\langle T|_{int}\rangle - T}{\langle T|_{int}\rangle - T_b} - 1\right) \end{cases} \tag{A.20}$$

Some interesting quantities can be obtained if T is substituted by $\langle T|_{int}\rangle$ or T_b, aiming to found an expression for the dimensionless temperature at the wall ($\Theta|_{int}$) or the bulk dimensionless temperature Θ_b, respectively. Moreover, the values of the dimensionless wall heat flux were obtained by applying normal derivative operator ($\partial_{\vec{n}}(\cdot)$) to the right-hand expressions of Θ in Eq. A.20, and evaluating it at the wall.

Tabela A.1: Temperature dimensionless expressions. The Nusselt number Nu is an output computed from the quantities with the average operator $\langle\cdot\rangle$. The last dimensionless form corresponds to the last one in Equation A.20.

Dimensionless temperature Θ	Wall temperature $\Theta\|_{int}$	Bulk temperature Θ_b	Temperature normal-wall gradient
$\Theta = \dfrac{\langle T\|_{int}\rangle - T}{\langle T\|_{int}\rangle - T_b}$	$\Theta\|_{int} = 0$	$\Theta_b = 1$	$\left\langle \left.\dfrac{\partial\Theta}{\partial\vec{n}}\right\|_{int} \right\rangle = Nu$
$\Theta = \dfrac{\langle T\|_{int}\rangle - T}{\dfrac{\varphi\|_{int}}{\rho c_p U_b}}$	$\Theta\|_{int} = 0$	$\langle\Theta_b\rangle = \dfrac{RePr}{Nu}$	$\left.\dfrac{\partial\Theta}{\partial\vec{n}}\right\|_{int} = RePr$
$\Theta = \dfrac{\langle T\|_{int}\rangle - T}{\dfrac{\varphi\|_{int}}{\rho c_p u_\tau}}$	$\Theta\|_{int} = 0$	$\langle\Theta_b\rangle = \dfrac{Re_\tau Pr}{Nu}$	$\left.\dfrac{\partial\Theta}{\partial\vec{n}}\right\|_{int} = Re_\tau Pr$
$\Theta = -\dfrac{1}{Nu}\left(\dfrac{T - T_b}{T\|_{int} - T_b}\right)$	$\langle\Theta\|_{int}\rangle = -1/Nu$	$\Theta_b = 0$	$\left.\dfrac{\partial\Theta}{\partial\vec{n}}\right\|_{int} = 1$

The dimensionless form used for the *IF* boundary condition is the last one in Eq. A.20 and in Table A.2. It is easy to show that $\Theta_b = 0$ since the numerator is canceled when $T = T_b$. In addition, by applying the average operator over Eq. 4.10, at the wall $T = T|_{int}$, it can be shown that dimensionless temperature at the interface is $\langle\Theta|_{int}\rangle = -1/Nu$. Finally, the

average dimensionless heat flux is unitary, which can be proved by applying dimensionless directional derivative operator $\partial_{\vec{n}}(\cdot)$ over this equation and combining Newton's law of cooling and Fourirer's law ($-\frac{\lambda}{L}\partial_{\vec{n}}T = h(\langle T|_{int}\rangle - T_b)$).

A.2 Ideal locally imposed linear temperature (IT)

For the Dirichlet-type boundary conditions (*IT* and *IUT*), it will be used the first dimensionless form of the Table A.2. The source term continues being the same as for *IF* (Equation A.19), while imposing the wall temperature implies that $\Theta|_{int} = 0$. Then, if

$$T|_{int} = \langle T|_{int}\rangle(x), \tag{A.21}$$

the boundary condition, for the so-called *IFT* thermal condition, is

$$\Theta|_{int} = 0. \tag{A.22}$$

It should be pointed out, that, although, this Dirichlet boundary condition implies that at the wall $T = T|_{int}$ ($\Theta|_{int} = 0$), $T|_{int}$ continues being linear function of x (Figure A.1), while ensuring the mean heat flux by the source term (Eq. A.19).

A.3 Ideal locally imposed uniform temperature (IUT)

To consider $T|_{int} = constant$ implies

$$\frac{d\,T|_{int}}{dx} = \frac{d\,\langle T|_{int}\rangle}{dx} = 0, \qquad T|_{int} = constant, \tag{A.23}$$

then, from Equation A.8

$$\frac{\partial\langle T\rangle(x,y,z)}{\partial x} = \frac{T|_{int} - \langle T\rangle(x,y,z)}{T|_{int} - T_b}\left(\frac{dT_b}{dx}\right) \qquad T|_{int} = constant. \tag{A.24}$$

Conversely to *IF*, this shows that the *streamwise temperature gradient* depends on spatial coordinates, which implies that the correction in the *streamwise temperature gradient* must be

function of them. Hence, substituting the results of Equations A.8, A.11, A.12 and A.23 in Equation A.4, the source term in the temperature transport equation is

$$f_\Theta(x,y,z) = \Theta\left[-u_x\left(\frac{1}{T_r}\frac{dT_r}{dx}\right) + \frac{1}{RePr}\left(\frac{1}{T_r}\frac{d^2T_r}{dx^2}\right)\right]$$
$$= \Theta\left[-u_x\left(\frac{\beta Nu}{RePr}\right) + \frac{1}{RePr}\left(\frac{\beta Nu}{RePr}\right)^2\right], \tag{A.25}$$

A.4 Relation between dimensionless temperatures

The governing equations can be solved considering any of the dimensionless expression. Some of these expressions sometimes are more convenient than others. However, a relation can be established between them, in such a way that after obtaining the simulation results, it is possible to transform one into the other one (Table A.2).

Tabela A.2: Relation between temperature dimensionless expressions.

Temporal notation	Dimensionless form	Expression in wall units (Θ^+)
Θ_T	$\dfrac{\langle T\vert_{int}\rangle - T}{\langle T\vert_{int}\rangle - T_b}$	$\Theta_T = \dfrac{Nu}{Re_\tau Pr}\Theta^+$
Θ_φ	$\dfrac{\langle T\vert_{int}\rangle - T}{\dfrac{\varphi\vert_{int}}{\rho c_p U_b}}$	$\Theta_\varphi = \dfrac{Re}{Re_\tau}\Theta^+$
Θ^+	$\dfrac{\langle T\vert_{int}\rangle - T}{\dfrac{\varphi\vert_{int}}{\rho c_p u_\tau}}$	Θ^+
Θ_{Nu}	$-\dfrac{1}{Nu}\left(\dfrac{T - T_b}{T\vert_{int} - T_b}\right)$	$\Theta_{Nu} = \dfrac{\Theta^+}{Re_\tau Pr} - \dfrac{1}{Nu}$

In the previous expression, the friction Reynolds number is defined as

$$Re_\tau = \frac{u_\tau(D/2)}{\nu} \quad or \quad \frac{u_\tau(H/2)}{\nu}. \tag{A.26}$$

Appendix B

Conjugate heat transfer in channel flow - Laminar solution

Conjugate heat transfer (*CHT*) represents the fluid-solid thermal coupling. Thus, the transport equation in the fluid domain (Ω) and the diffusion equation in the solid domain (Ω_s) are coupled by the thermal boundary conditions at the fluid-solid interface ($|_{int}$) and the outer solid boundary ($|_{out}$). The dimensionless energy equations read

$$\frac{\partial \Theta}{\partial t} = -\vec{u} \cdot \nabla \Theta + \frac{1}{RePr} \nabla^2 \Theta + f_\Theta \ in \ \Omega, \tag{B.1}$$

$$\frac{\partial \Theta_s}{\partial t} = \frac{1}{GRePr} \nabla^2 \Theta_s + f_{\Theta_s} \ in \ \Omega_s, \tag{B.2}$$

$$\Theta|_{int} = \Theta_s|_{int}\,, \tag{B.3}$$

$$\left.\frac{\partial \Theta_s}{\partial \vec{n}}\right|_{int} = \frac{1}{G_2} \left.\frac{\partial \Theta}{\partial \vec{n}}\right|_{int}, \tag{B.4}$$

$$\left.\frac{\partial \Theta_s}{\partial \vec{n}}\right|_{out} = \frac{1}{G_2} \left.\frac{\partial \langle \Theta \rangle}{\partial \vec{n}}\right|_{int}, \tag{B.5}$$

where Θ (Θ_s) is the fluid (solid) temperature, $G = \lambda \rho_s c_{ps} / (\lambda_s \rho c_p)$ the ratio of thermal diffusivi-

ties and $G_2 = \lambda_s/\lambda$ the ratio of thermal conductivities. Equation B.3 represents the temperature continuity on the interface, and the Equation B.4 imposes the heat flux at that interface which physically represents the energy conservation.

Considering the dimensionless temperature form as

$$\Theta = \frac{1}{Nu}\left(1 - \frac{T|_{int} - T}{T|_{int} - T_b}\right), \tag{B.6}$$

the dimensionless temperature at the interface is

$$\Theta|_{int} = \Theta_s|_{int} = \frac{1}{Nu}, \tag{B.7}$$

the bulk temperature is

$$\Theta_b = 0 \tag{B.8}$$

and the source term in the fluid energy equation (B.1) is

$$f_\Theta = -2\frac{u_x}{RePr}. \tag{B.9}$$

The temperature was conveniently normalized (B.6), in order to ensure that, in fully developed flow, the dimensionless mean temperature $\langle\Theta\rangle$ has not streamwise variation ($x-$direction). It means that, in steady flow, $\partial\Theta/\partial x = 0$ or $\Theta = \Theta(y)$, since Θ has not spanwise gradient ($z-$direction). For Pouseuille channel flow (1D steady flow), energy equations in the fluid and the solid (B.1 and B.2) can respectively be rewritten as

$$0 = \frac{d^2\Theta}{dy^2} - 2u_x, \tag{B.10}$$

$$0 = \frac{d^2\Theta_s}{dy^2}, \tag{B.11}$$

$$\Theta|_{int} = \Theta_s|_{int}\,, \tag{B.12}$$

$$\left.\frac{d\Theta_s}{dy}\right|_{int} = \frac{1}{G_2}\left.\frac{d\Theta}{dy}\right|_{int}, \tag{B.13}$$

$$\left.\frac{d\Theta_s}{dy}\right|_{out} = \frac{1}{G_2}\left.\frac{\partial\Theta}{\partial y}\right|_{int}, \tag{B.14}$$

where

$$u_x = \frac{3}{2}\left(1 - 4y^2\right). \tag{B.15}$$

Remembering that, for simplicity, in the equations above, the symbols $|_{int}$ and $|_{out}$ indicate respectively that the variable is evaluated at the fluid/solid *interface* or at the solid *outer* (computational) boundary. The second derivative of the fluid temperature field is a parabola (Equations B.10 and B.15) and the second derivative in the solid is null (Equation B.11). Hence, from those equations, it can be observed that the temperature solution in the solid and fluid must be a first and second order polynomials, respectively.

The solid plane plates at the top and bottom of the channel are normal to the y axis and are located at $y = \pm 0.5$. Assuming that the plate have thickness δ_s, the fluid domain is defined in $|y| \leqslant 0.5$, and the solid domain in $0.5 \leqslant |y| \leqslant \left(0.5 + \delta_s = L_y/2\right)$, where L_y is the computational domain size in y-direction. Integrating Equation B.10 between the center of the channel ($y = 0$) and the interface ($y = \pm 0.5$), it follows

$$\int_0^{\left.\frac{d\Theta}{dy}\right|_{int}} \frac{d\Theta}{dy} = 3\int_0^{\pm 0.5}\left(1 - 4y^2\right)dy, \tag{B.16}$$

$$\left.\frac{d\Theta}{dy}\right|_{int} = \begin{cases} -1, & at\ y = 0.5, \\ \\ 1, & at\ y = -0.5. \end{cases} \tag{B.17}$$

$$\left.\frac{d\Theta}{dy}\right|_{int} = \mp 1, \quad at\ y = \pm 0.5, \tag{B.18}$$

$$\left.\frac{d\Theta}{dy}\right|_{int} = -\frac{y}{|y|}. \tag{B.19}$$

Then, an energy balance (Equations B.13 and B.14) shows that

$$\left.\frac{d\Theta_s}{dy}\right|_{int} = \left.\frac{d\Theta_s}{dy}\right|_{out} = \begin{cases} -\dfrac{1}{G_2}, & at\ y = 0.5, \\ \\ \dfrac{1}{G_2}, & at\ y = -0.5. \end{cases} \tag{B.20}$$

Now, integrating Equation B.10 between a generic point (y) and the interface ($y = \pm 0.5$), we obtain

$$\int_{\frac{d\Theta}{dy}(y)}^{\left.\frac{d\Theta}{dy}\right|_{int} = \mp 1} \left(\frac{d\Theta}{dy}\right)' = 3\int_{y}^{\pm 0.5} \left(1 - 4y'^2\right) dy', \tag{B.21}$$

$$\frac{d\Theta}{dy}(y) = 4\,|y|^3 - 3\,|y| \quad for \quad |y| \leqslant 0.5. \tag{B.22}$$

Integrating again, the temperature field can be written as

$$\int_{\Theta(y)}^{\Theta|_{int}} d\Theta' = \int_{y}^{\pm 0.5} \left(4y'^3 - 3y'\right) dy', \tag{B.23}$$

$$\Theta(y) - \Theta|_{int} = \frac{1}{16}\left(16y^4 - 24y^2 + 5\right), \quad for \quad |y| \leqslant 0.5 \tag{B.24}$$

Finally, by integrating Equation B.11 twice, the solid derivative and temperature solutions respectively are

$$\frac{d\Theta_s}{dy} = -\frac{y}{|y|}\left(\frac{1}{G_2}\right), \quad for \ \ 0.5 \leqslant |y| \leqslant L_y/2 \tag{B.25}$$

$$\Theta_s(y) - \Theta_s|_{int} = \frac{1}{G_2}\left(0.5 - |y|\right), \quad for \ \ 0.5 \leqslant |y| \leqslant L_y/2 \tag{B.26}$$

It should be stressed that the solution in the fluid, for the dimensionless form adopted, is independent on the conductivity ratio $G_2 = \lambda_s/\lambda$, contrarily to the solution in the solid (Figure

B.1).

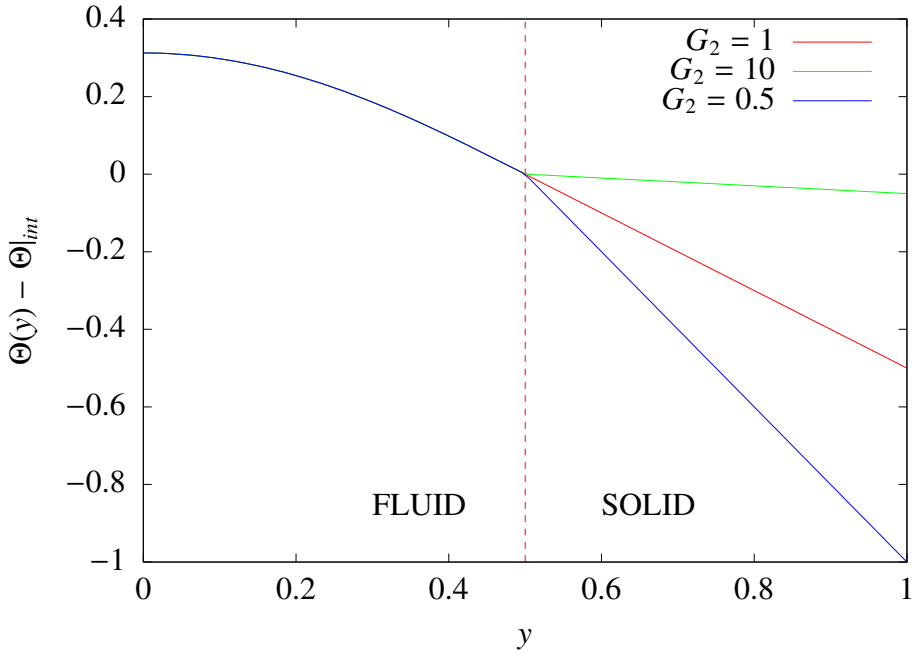

Figura B.1: Temperature distribution in a Pouseuille channel flow, for various conductivity ratios $G_2 = \lambda_s/\lambda$. For dimensionless temperature solution in the fluid is independent on G_2.

Bibliografia

[1] Angot, P., Bruneau, C. H., and Frabrie, P. A penalization method to take into account obstacles in viscous flows. *Num. Math.* **81** (1999), 497–520.

[2] Atzberger, P. J., Kramer, P. R., and Peskin, C. S. A stochastic immersed boundary method for fluid-structure dynamics at microscopic length scales. *JCP* **224**, 2 (2007), 1255–1292.

[3] Balaras, E. Modeling complex boundaries using an external force field on fixed cartesian grids in large-eddy simulations. *Comp. Fluids* **33(3)** (2004), 375–404.

[4] Binnie, A. M., and Fowler, J. S. A study by a double refraction method of the development of turbulence in a long cylindrical tube. In *Proceedings of the Royal Society of London, Oct. 9. Series A: Mathematical and Physical Sciences.* (London, 1947), vol. 192, p. 32.

[5] Borazjani, I., Ge, L., and Sotiropoulos, F. Curvilinear immersed boundary method for simulating fluid structure interaction with complex 3d rigid bodies. *J. Comp. Phys.* **227** (2008), 7587–7620.

[6] Borue, V., and Orszag, S. A. Local energy flux and subgrid-scale statistics in three-dimensional turbulence . *J. Fluid Mech.* **366** (1998), 1–31.

[7] Brinkmann, H. C. A calculation of the viscous force exerted by a flowing fluid on a swarm of particles. *Appl. Sci. Res.* **468** (1947).

[8] Dairay, T. *High fidelity simulation of the aerothermal of an impinging jet*. Theses, Université de Poitiers, Nov. 2013.

[9] Dairay, T., Lamballais, E., and Benhamadouche, S. Mesh node distribution in terms of wall distance for large-eddy simulation of wall-bounded flows. *Flow, Turbulence and Combustion* (2017), 1–10.

[10] Dairay, T., Lamballais, E., Laizet, S., and Vassiliscos, J. C. Numerical dissipation vs. subgrid-scale modelling for large eddy simulation. *J. Comp. Phys.* (2017), 1–10.

[11] Darbyshire, A. G., and Mullin, T. Transition to turbulence in constant-mass-flux pipe flow. *J. Fluid Mech.* **289** (1995), 83–114.

[12] El Khoury, G. K., Schalatter, P., Noorani, A., Fischer, P. F., Brethouwer, G., and Johansson, A. V. Direct numerical simulation of turbulent pipe flow at moderately high reynolds numbers. *Flow, Turbulence and Combustion* **91** (2013), 475–495.

[13] Fadlun, E., Verzicco, R., Orlandi, P., and Mohd-Yusof, J. Combined immersed boundary finite-difference methods for the three-dimensional complex flow simulations. *J. Comp. Phys.* **161** (2000), 35–60.

[14] Fauci, L. J., and Dillon, R. Biofluidmechanics of reproduction. *Annu. Rev. Fluid Mech. 38* (2006), 371–394.

[15] Ferziger, J. H., and Perić, M. *Computational Methods in Fluid Dynamics*, 3 ed. Springer-Verlag, New York, USA, 2002.

[16] Flageul, C. *Création de bases de donnés fines par simulation directe pour les effects de la tubulence sur les tranferts thermiques pariétaux.* PhD thesis, Université de Poitiers, Poitiers - France., 2015.

[17] Flageul, C., Benhamandouche, S., Laballais, E., and Laurence, D. DNS of turbulent channel flow with conjugate heat transfer: Effect of thermal boundary conditions on the second moments and budgets. *Int. J. Comp. Fluid Dyn.* **28** (2015), 393–410.

[18] Flageul, C., Benhamandouche, S., Laballais, E., and Laurence, D. On the discontinuity of the dissipation rate associated with the temperature variance at the fluid-solid interface for cases with conjugate heat transfer. *Int. J. Comp. Fluid Dyn.* **111** (2017), 321–328.

[19] Fortuna, A. O. *Técnicas Computacionais para Dinâmica dos Fluidos*, 2 ed. Editora da Universidade de São Paulo, São Paulo, Brasil, 2012.

[20] Gautier, R. *Calcul haute fidélité de la turbulence en géometrie complexe: Application au contrôle fluidique d'un jet*. Theses, Université de Poitiers, Dec. 2013.

[21] Gautier, R., Biau, D., and Lamballais, E. A reference solution of the flow over a circular cylinder at Re=40. *Journal Computers and Fluids* **75** (2014), 103–111.

[22] Gautier, R., Laizet, S., and Laballais, E. A dns study of jet control with microjets using an immersed boundary method. *Int. J. Comp. Fluid Dyn.* **28** (2014), 393–410.

[23] Ge, Y., and Fan, L.-S. Three-dimensional direct numerical simulation for film-boiling contact of moving particle and liquid droplet. *Phys. Fluids* **18**, 11 (2006), 117104.

[24] Ghias, R., Mittal, R., and Dong, H. A sharp interface immersed boundary method for compressible viscous flows. *JCP* **225**, 1 (2007), 528–553.

[25] Giles, M. B. Stability analysis of numerical interface conditions in fluid-structure thermal analysis. *Int. J. Numer. Methods Fluids* **25** (1997), 421–436.

[26] Gilmanov, A., and Sotiropoulos, F. A hybrid cartesian/immersed boundary method for simulating flows with 3d, geometrically complex, moving bodies. *JCP 207*, 2 (2005), 457–492.

[27] Gnielinski, V. New equations for heat and mass transfer in the turbulent pipe and channel flow. *International Chemical Engineering* **16** (1976), 359–368.

[28] Goldstein, D., Handler, R., and Sirovich, L. Modeling a no-slip flow boundary with an external force field. *J. Comp. Phys.* **105** (1993), 354–366.

[29] Guerreiro, C. B. P. Resolução numérica das equações de navier-stokes com esquemas de diferenças finitas de quarta ordem. Master's thesis, Universidade Federal do Rio Grande do Sul. Instituto de Matemática. Programa de Ps-Graduação em Matemática Aplicada, Porto Alegre, 2000.

[30] Iaccarino, G., and Moreau, S. Natural and forced conjugate heat transfer in complex geometries on cartesian adapted grids. *J. Fluids Engine.* **128** (2006), 838–846.

[31] Iaccarino, G., and Verzicco, R. Immersed boundary technique for turbulent flow simulations. *Appl. Mech. Rev.* **36** (2003), 331–347.

[32] Incropera, F., and Dewit, D. *Fundamentals of Heat and Mass transfer*, 4 ed. John Wiley and Sons, 2000.

[33] Isshiki, S., Obata, T., Kasagi, N., and Hirata, N. An experimental study on heat transfer in a pulsating pipe flow (1st report, time-averaged turbulent characteristics). *Bulletin of the Japan Society of Mechanicals Engineers* **59** (1993), 2245–2251.

[34] Kang, S., Iaccarino, G., and Ham, F. Dns of buoyancy-dominated turbulent flows on a bluff body using the immersed boundary method. *J. Comp. Phys. 228*, 9 (2009), 3189–3208.

[35] Karmannos, G. S., and Kaniadakis, G. E. A spectral vanishing viscosity method for large-eddy simulations. *J. Comp. Phys.* **163** (2000), 22–50.

[36] Kasagi, N., Horiuti, K., Miyake, Y., Miyauchi, T., and Nagano, Y. Test case: fully developed 2-d channel flow. *Disponvel em www.thtlab.t.u-tokyo.ac.jp/* (1992).

[37] Kasagi, N., Kuroda, A., and Hirata, M. Numerical investigation of near-wall turbulent heat transfer taking into account the unsteady heat conduction in the solid wall. *J. Heat Transfer* **111**, **2** (1989), 385–392.

[38] Kasagi, N., and Shikazono, N. Contribution of direct numerical simulation to understanding and modelling turbulent transport. In *Proceedings of the Royal Society of London, Oct. 9. Series A: Mathematical and Physical Sciences.* (London, 1995), vol. 451, pp. 257–292.

[39] Kawamura, H., Ohsaka, K., Abe, H., and Yamamoto, K. DNS of turbulent heat transfer in channel flow with low to medium-high Prandtl number fluid. *Int. J. Heat and Fluid Flow* **19(5)** (1998), 482–491.

[40] Khabakhpasheva, Y. M. Experimental investigation op turbulent momentum and heat transfer in the proximity op the wall. *International Heat transfer Conference* (1986), 79–90.

[41] Khandra, K., Angot, P., Parneix, S., and Caltagirone, J. P. Fictitious domain approach for numerical modeling of Navier-Stokes equations. *Int. J. Numer. Methods Fluids* **34** (2000), 651–684.

[42] Kim , D., and Choi, H. Immersed boundary method for flow around an arbitrarily moving body. *J. Comp. Phys.* **212** (2006), 662–680.

[43] Kim, J. Classic ercoftac database at university of surrey. *Disponvel em www.ercoftac.org* (1989).

[44] Kim, J., and Choi, H. An immersed-boundary finite-volume method for simulation of heat transfer in complex geometries. *KSME international journal 18*, 6 (2004), 1026–1035.

[45] Kim, W., and Choi, H. Immersed boundary methods for fluid-structure interaction: A review. *Int. J. Heat and Fluid Flow* (2019).

[46] Lai, M. C., and Peskin, C. S. An immersed boundary method with formal second-order accuracy and reduced numerical viscosity. *J. Comp. Phys.* **160** (2000), 705 – 719.

[47] Laizet, S. *Développement d'un code de calcul combinant des schémas de haute précision avec une méthode de frontière immergée pour la simulation des mouvements tourbillonnaires en aval d'un bord de fuite*. Theses, Université de Poitiers, Dec. 2005.

[48] Laizet, S., and Lamballais, E. High-order compact schemes for incompressible flows: A simple and efficient method with quasi-spectral accuracy. *J. Comp. Phys. 228* (2009), 5989–6015.

[49] Laizet, S., Lamballais, E., and Vassilicos, J. C. A numerical strategy to combine high-order schemes, complex geometry and massively parallel computing for dns of fractal generated turbulence. *Journal Computers and Fluids 39* (2010), 471–484.

[50] Laizet, S., and Li, N. Incompact3d: A powerful tool to tackle turbulence problems with up to $o(10^5)$ computational cores. *Int. J. Numer. Methods Fluids 67* (2011), 1735–1757.

[51] Lamballais, E., Fortuné, V., and Laizet, S. Straightforward high-order numerical dissipation via the viscous term for direct and large eddy simulation. *J. Comp. Phys.* **230** (2011), 3270–3275.

[52] Lamorgese, A. G., Caughey, D. A., and Pope, S. B. Direct numerical simulation of homogeneous turbulence with hyperviscosity. *Phys. Fluids* **17** (2005), 1–10.

[53] Lardeau, S., Lamballais, E., and Bonnet, J. P. Direct numerical simulation of a jet controlled by fluid injection. *J. Turbulence* **3** (2002).

[54] Leite, R. J. An experimental investigation of the stability of Poiseuille flow. *J. Fluid Mech.* **5** (1959), 81.

[55] Lele, S. Compact finite difference schemes with spectral-like resolution. *J. Comp. Phys.* **103** (1992), 16–42.

[56] Li, Q., Schlatter, P., Brandt, L., and Henningson, D. S. Dns of a spatially developing turbulent boundary layer with passive scalar transport. *Int. J. Heat and Fluid Flow*.

[57] Linnick, M. N., and Fasel, H. F. A high-order immersed boundary method for unsteady incompressible flow calculations. In *Proceedings of 41st AIAA Aerospace Sciences Meeting and Exhibit* (Reno, NV, 2003), pp. 1–17.

[58] Luo, H., Yin, B., Dai, H., and Doyle, J. A 3d computational study of the flow-structure interaction in flapping flight. In *48th AIAA aerospace sciences meeting including the new horizons forum and aerospace exposition* (2010), p. 556.

[59] Luo, K., Mao, C., Zhuang, Z., Fan, J., Haugen, N., and Erland, L. A ghost-cell immersed boundary method for the simulations of heat transfer in compressible flows under different boundary conditions part-ii: Complex geometries. *Int. J. Heat and Mass Transfer 104* (2017), 98–111.

[60] Luo, K., Zhuang, Z., Fan, J., Haugen, N., and Erland, L. A ghost-cell immersed boundary method for simulations of heat transfer in compressible flows under different boundary conditions. *IJHMT 92* (2016), 708–717.

[61] Mittal, R., and Iaccarino, G. Immersed boundary methods. *Annu. Rev. Fluid Mech.* **37** (2005), 239–261.

[62] Mohd-Yosuf, J. Combined immersed boundary/b-spline methods for simulation of flow in complex geometries. *Annu. Res. Briefs, Cent. Turbul. Res.* (1997), 317–328.

[63] Moin, P. *Fundamentals of Engineering Numerical Analysis*. Cambridge University Press, Stanford University, 2001. 209p.

[64] Moraga, N. O., and Salinas, C. H. Numerical model for heat and fluid flow in food freezing. *Numerical Heat Transfer: Part A: Applications 35*, 5 (1999), 495–517.

[65] Mukun, V., and Hof, B. The critical point of the transition to turbulence in pipe flow. *J. Fluid Mech.* **839** (2018), 76–94.

[66] Narváez, G. F. Análise numérica da vibração induzida por vórtices de dois cilindros em alinhados com o escoamento. Master's thesis, Universidade Federal do Rio Grande do Sul. Instituto de Pesquisas Hidráulicas. Programa de Pós-Graduação em Recursos Hídricos e Saneamento Ambiental, Porto Alegre, 2015.

[67] Narváez, G. F., Lamballais, E., and Camaño, E. B. Transporte escalar em escoamento em conduto circular forçado. estudo de caso: transferência de calor (accepted). In *XXVII Congreso Latinoamericano de hidráulica.* (Buenos Aires - Argentina, 2018).

[68] Nestola, M. G. C., Becsek, B., Zolfaghari, H., Zulian, P., De Marinis, D., Krause, R., and Obrist, D. An immersed boundary method for fluid-structure interaction based on overlapping domain decomposition. *arXiv preprint arXiv:1810.13046* (2018).

[69] Nishioka, M., and Asai, M. Some observations of the subcritical transition in plane Poiseuille flow. *J. Fluid Mech.* **150** (1985), 441–450.

[70] Orszag, S. A. Accurate solution of the Orr-Sommerfeld equation. *J. Fluid Mech.* **50** (1971), 689–703.

[71] Pacheco, J. R., Pacheco-Vega, A., Rodić, T., and Peck, R. E. Numerical simulations of heat transfer and fluid flow problems using an immersed-boundary finite-volume method on nonstaggered grids. *Numerical Heat Transfer, Part B: Fundamentals 48*, 1 (2005), 1–24.

[72] Parnaudeau, P., andD. Heitz, E. Lamballais., and Silvestrini, J. H. *Combination of the immersed boundary method with compact schemmes for DNS of flows in complex geometry.* Kluwer academic publishers., 2003, p. 10p.

[73] Parnaudeau, P., andD. Heitz, E. Lamballais., and Silvestrini, J. H. *Combination of the immersed boundary method with compact schemmes for DNS of flows in complex geometry.* Kluwer academic publishers., 2004, p. 10p.

[74] Parnaudeau, P., Carlier, J., Dominique, D., and Lamballais, E. Experimental and numerical studies of the flow over a circular cylinder at reynolds number 3900. *Phys. Fluids* **20** (2008), 085101–085101.

[75] Pasquetti, R. Spectral vanishing viscosity method for large-eddy simulation of turbulent flows. *Journal of Scientific Computing* **27** (2006), 365–375.

[76] Perot, B. Conservation properties of unstructured staggered mesh schemes. *J. Comp. Phys.* **159** (2000), 58–89.

[77] Peskin, C. S. *Flow patterns around heart valves: a digital computer method for solving the equations of motion.* PhD thesis, Physiol., Albert Einstein Coll. Med., Univ. Microfilms. Bronx, NY, 1972.

[78] Pfenniger, W. *Heat Transfer.* ed Wiley, Wiley: NY, 1958.

[79] Pfenniger, W. *Transition in the inlet length of tubes at high Reynolds numbers Boundary Layer and Flow Control.* ed G. V. Lachman., Oxford: Pergamon, 1961.

[80] Piller, M. Direct numerical simulation of turbulent forced convection in a pipe. *Int. J. Numer. Methods Fluids* **49** (2005), 583–602.

[81] Pinto, L. *Análise por simulação numérica direta do escoamento ao redor de um cilindro submetido a vibração induzida por vórtices.* PhD thesis, Universidade Federal do Rio Grande do Sul, Porto Alegre - Rio Grande do Sul., 2012.

[82] Pirozzoli, S., Bernardini, M., and Orlandi, P. Passive scalars in turbulent channel flow at high reynolds number. *J. Fluid Mech.* **788** (2016), 614 – 639.

[83] Poliakov, A. Wall effect on temperature fluctuations in the viscous sublayer. *High Temperature Science 12* (1974), 328–337.

[84] Redjem-Saad, L., Ould-Rouiss, M., and Lauriat, G. Direct numerical simulation of turbulent heat transfer in pipe flow. *Int. J. Heat and Fluid Flow* **28** (2007), 847–861.

[85] Ren, W., Shu, C., Wu, J., and Yang, W. Boundary condition-enforced immersed boundary method for thermal flow problems with dirichlet temperature condition and its applications. *Computers & Fluids 57* (2012), 40–51.

[86] Ren, W., Shu, C., and Yang, W. An efficient immersed boundary method for thermal flow problems with heat flux boundary conditions. *International Journal of Heat and Mass Transfer 64* (2013), 694–705.

[87] Reynolds, O. An experimental investigation of the circumstances which determine whether the motion of water in parallel channels shall be direct or sinuous and of the law of resistance in parallel channels. *Philos. Trans. R. Soc. London* **174** (1883), 935–982.

[88] Saha, S., Blackburn, H. M., and Ooi, A. S. H. The influence of pipe lenght on thermal statistics computed from DNS of turbulent heat transfer. *Int. J. Heat and Fluid Flow* **32** (2011), 1083–1097.

[89] Saha, S., Ooi, A. S. H., and Blackburn, H. M. Validation criteria for DNS of turbulent heat transfer in pipe flow. In *Procedia Engineering, 10th International Conference on Mechanical Engineering.* (Dhaka - Bangladesh, 2014), pp. 599–604.

[90] Saiki, E. M., and Biringen, S. Numerical simulation of a cylinder in uniform flow: Application of a virtual boundary method. *J. Comp. Phys.* **123(2)** (1996), 450–465.

[91] Sano, M., and Tamai, K. A universal transition to turbulence in channel flow. *Nature Physics* **12(3)** (2015), 393–410.

[92] Satake, S., Kunugi, T., and Himeno, R. High reynolds number computation for turbulent heat transfer in a pipe flow. In *High Performance Computing, Third International Symposium.* (Tokyom Japan, 2000), pp. 514–523.

[93] Sinai, Y. L. A wall function for the temperature variance in turbulent flow adjacent to a diabatic wall. *J. Heat Transfer 109*, 4 (1987), 861–865.

[94] Smolarkiewicz, P. K., Sharman, R., Weil, J., Perry, S. G., Heist, D., and Bowker, G. Building resolving large-eddy simulations and comparison with wind tunnel experiments. *J. Comp. Phys.* **227**, 1 (2007), 633–653.

[95] So, R., and Sommer, T. An explicit algebraic heat-flux model for the temperature field. *Int. J. Heat and Mass Transfer 39*, 3 (1996), 455–465.

[96] Song, J. C., Ahn, J., and Lee, J. S. An immersed-boundary method for conjugate heat transfer analysis. *Journal of Mechanical Science and Technology 31*, 5 (2017), 2287–2294.

[97] Tiselj, I., Bergant, R., Mavko, B., Bajsić, I., and Hetsroni, G. DNS of turbulent heat transfer in channel flow with heat conduction in solid wall. *J. Heat Transfer* **123(3)** (2001), 849–857.

[98] Tiselj, I., Pogrebnyak, E., Li, C., mosyak, A., and Hetsroni, G. Effect of wall boundary condition on scalar transfer in a fully developed turbulent flume. *Phys. Fluids* **13(4)** (2001), 1028–1039.

[99] Tseng, Y. H., and Ferziger, J. H. A ghost-cell immersed boundary method for flow in complex geometry. *J. Comp. Phys.* **192** (2003), 593–623.

[100] Tsukahara, T., and Ishida, T. The lower bound of subcritical transition in plane Poiseuille flow. In *Proceedings of the Euromech Colloquium EC656, May 6-9. Subcrital transition to turbulence.* (Cargèse - France, 2014), p. 83.

[101] Uhlmann, M. An immersed boundary method with direct forcing for the simulation of particulate flows. *JCP 209*, 2 (2005), 448–476.

[102] Van Dyke, M. *An album of fluid motion.* The Parabolic Press., Standford, California, 1982.

[103] Verzicco, R., Mohd-Yusof, J., Orlandi, P., and Haworth, D. Les in complex geometries using boundary body forces. *AIAA Paper* **38** (2000), 427–433.

[104] Vichnevetsky, R., and Bowles, J. B. *Fourier anlaysis of numerical approximations of hyperbolic equations.*, vol. 5. Siam., 1982.

[105] Wang, M., and Georgiadi, J. G. Conjugate forced convection in crossflow over a cylinder array with volumetric heating. *Int. J. Heat and Mass Transfer* **39**, **7** (1996), 1351–1361.

[106] Wang, Z., Fan, J., Luo, K., and Cen, K. Immersed boundary method for the simulation of flows with heat transfer. *International Journal of Heat and Mass Transfer 52*, 19-20 (2009), 4510–4518.

[107] White, F. M. *Fluid mechanics.*, 7 ed. ed. McGraw-Hill, United States of America - university of Rhode Island., 2011. 353p.

[108] Ye, T., Mittal, R., Udaykumat, H. S., and Shyy, W. An accurate cartesian grid method for viscous incompressible flows with complex immersed boundaries. *J. Comp. Phys.* **156** (1999), 209–240.

[109] Young, T. J., and Vafai, K. Convective cooling of a heated obstacle in a channel. *Int. J. Heat and Mass Transfer 41*, 20 (1998), 3131–3148.

[110] Yu, Z., Shao, X., and Wachs, A. A fictitious domain method for particulate flows with heat transfer. *J. Comp. Phys.* **217** (2007), 424–452.

[111] Zhang, N., Zheng, Z., and Eckels, S. Study of heat-transfer on the surface of a circular cylinder in flow using an immersed-boundary method. *International Journal of Heat and Fluid Flow 29*, 6 (2008), 1558–1566.

[112] Zhang, N., and Zheng, Z. C. An improved direct-forcing immersed-boundary method for finite difference applications. *J. Comp. Phys.* **221(1)** (2007), 250–268.

[113] Zhang, Y. Critical transition Reynolds number for plane channel flow. *Appl. Math. Mech.* **38** (2017), 1415 – 1424.

[114] Zhao, H., Freund, J. B., and Moser, R. D. A fixed-mesh method for incompressible flow–structure systems with finite solid deformations. *J. Comp. Phys. 227*, 6 (2008), 3114–3140.